HEAVY NEUTRAL LEPTON DECAY SEARCHES AT THE NA62 EXPERIMENT AT CERN

Lorenza Iacobuzio

Thesis submitted to the University of Birmingham
for the degree of Doctor of Philosophy

UNIVERSITY OF BIRMINGHAM

Supervisors:
Dr. Evgueni Goudzovski
Dr. Angela Romano

Particle Physics Group
School of Physics and Astronomy
University of Birmingham

30th of September 2019

Abstract

A sensitivity study on a new dark fermion, the Heavy Neutral Lepton (HNL), decaying to pion-muon final states at the NA62 experiment at CERN is discussed in this thesis, within a theoretical framework called the Neutrino Minimal Standard Model. A full Monte Carlo simulation that has been developed to quantify the expected sensitivity of the NA62 experiment to HNL decays is detailed in this work.

A data-driven background evaluation has been performed on a data set collected for HNL decay searches during the 2016-2018 data taking by the NA62 experiment. Results on the expected number of background events to $N \to \pi\mu$ decays are presented in this thesis.

To me, as arrogant and unnecessary as it sounds

Contents

Declaration of author's contribution

For this thesis, a full Monte Carlo simulation has been implemented to study Heavy Neutral Lepton (HNL) production from D mesons and its decay to two-body final states at the NA62 experiment. This constitutes my own work, together with the study of expected sensitivity curves for HNL decays to pion-muon final states, according to several chosen benchmark theoretical models. I am solely responsible for the implementation and maintenance of the Monte Carlo simulation and the code used to provide the sensitivity curves. The results of my own work also include a data-driven study of the background to HNL decays to pion-muon final states, performed on a data set collected in 2016-2018.

A full description of the theoretical framework for HNL studies and the NA62 experiment is provided to support my own work detailed in this thesis.

Whilst I was not involved in the design and construction of the NA62 experiment, I have worked in close collaboration with the trigger and data acquisition working group, testing and maintaining several algorithms for the NA62 software trigger system. I also participated in the data-taking operation between 2016 and 2018, both as expert for the KTAG detector and the trigger system and as a shift worker.

No other qualifications have been achieved with the work reported in this thesis.

Introduction and motivation

The Standard Model (SM) of particle physics has become, over the last 50 years, one of the most complete theories in the history of science, requiring precise scrutiny and, nonetheless, leaving several open questions. Tensions between the SM predictions and the experimental observations are yet to be understood, such as neutrino oscillations and masses, matter-antimatter asymmetry and the presence of dark matter and dark energy [1].

Since their discovery, it was believed that neutrinos were massless particles. In 1957, Bruno Pontecorvo predicted that neutrinos have non-zero masses, and that each flavour species can oscillate to another one with a probability that is proportional to the squared mass differences between mass states [2,3]. Several observations of neutrino oscillations have been performed throughout the years, confirming that neutrinos are massive. The first one occurred in the late 1960s, when a flux of electron neutrinos emitted from the solar core was observed, which was roughly a third of the SM expectation [4]. This tension between the experimental observation and the theoretical prediction require the SM to be extended to include neutrino masses and oscillations.

Another tension that arises from experimental observations is the matter-antimatter asymmetry, also known as Baryon Asymmetry of the Universe (BAU), one of the greatest unresolved mysteries of modern particle physics and cosmology. During the Big Bang, equal amounts of matter and antimatter were produced, but all antimatter has disappeared from the universe as we observe it, due to unknown reasons [5].

The presence of dark matter and dark energy is not accounted for either in the SM, although several pieces of experimental evidence have been observed. For example, the Hubble Space Telescope has found that the rate of expansion of the universe is increasing with respect to how it was in the past. This could be explained by adding a new property of spacetime, the dark energy, which would account for roughly 70% of the observable universe.

Evidence for dark matter, which would constitute about 25% of the universe, has been collected, including galactic rotational curves and Cosmic Microwave Back-

ground (CMB) structures [6]. All of these suggest that the observed patterns cannot be explained without fitting the presence of dark matter into the theoretical models.

These, several other experimental tensions and the fact that gravity and the three other fundamental forces cannot be described yet by a unified theoretical model are attempted to be explained by proposing new, broader theoretical models that include the SM, within a new branch of particle physics called Physics Beyond the Standard Model (PBSM) or New Physics (NP). Some of these models suggest the existence of new particles whose presence would provide explanation for experimental tensions. Two classes of PBSM particles are currently searched for at particle experiments, with two different approaches: Weakly Interacting Massive Particles (WIMPs) on one side and "Hidden-Sector" Mediators (HSMs) and "Dark Fermions" (DFs) on the other. The two approaches are complementary and fundamental to precisely test the validity of the SM.

WIMPs are hypothetical new elementary particles, with a mass of the order of 1 TeV/c^2 [7], which may only interact via gravity and weak force and constitute, therefore, a candidate for dark matter. Experimental efforts to detect WIMPs include indirect searches, through observation of their annihilation or decay far away from Earth, in the centers of galaxies and galaxy clusters; and direct searches, which refer to the observation of a WIMP-nucleus collision as the dark matter passes through a detector in a particle physics experiment [8].

HSMs and DFs are proposed to have masses in the MeV/c^2-GeV/c^2 range and they feebly interact with SM particles. These new particles may decay to SM final states via charged or neutral current interactions and be detected by several particle laboratories. This is why numerous experiments are currently focusing on measuring large statistics of rare decays, in the hope of observing deviations from SM predictions, which could be explained in terms of HSM and DF exchanges.

This PhD thesis focuses on a SM extension that operates through a dark fermion called Heavy Neutral Lepton, whose decay products are searched for at the NA62 experiment at CERN. This fixed-target experiment at the CERN Super Proton Synchrotron (SPS) has been designed to measure the rate of the rare decay $K^+ \to \pi^+\nu\bar{\nu}$, by collecting roughly 100 SM events [9].

The high flux of protons delivered to the NA62 experiment ($\sim 10^{12}$ protons/s) is also exploited to perform a broad programme of rare and forbidden kaon decays and HSM and DF searches, including HNL ones. Several features of the experimental apparatus make NA62 suitable for searches of long-lived, feebly-interacting HSM particles and DFs. NA62 collects 10^{18} Protons on Target (POT) per data-taking year, which allows the observation of particles that would be produced in SM decays with low mixing. The energy beam and the length of the NA62 detector are such

that these long-lived mediators could travel up to the experiment fiducial decay region and decay in it. Moreover, several NA62 detectors can be used to detect possible decay products of HSMs and DFs. Their high resolutions and efficiencies can be exploited to perform data-driven studies on the background sources to HSM and DF searches.

This thesis details the NA62 sensitivity to HNL decays to pion-muon final states. The HNL production and decay is studied within a theoretical framework called the Neutrino Minimal Standard Model (νMSM), which is presented in the first Chapter. The second Chapter describes the NA62 physics programme and its experimental setup. The third Chapter focuses on the full Monte Carlo simulation for HNL production and decay at NA62 within the νMSM framework, while the fourth Chapter introduces the expected sensitivity and the data analysis strategy for HNL decays to pion-muon final states. In the fifth Chapter, background studies performed on a data sample collected between 2016 and 2018 for HNL searches are discussed. Finally, the sixth Chapter draws the conclusions, outlook and future possible applications of this work.

Chapter 1

Theoretical framework

Despite being the most complete theory of particle physics phenomenology, the Standard Model (SM) does not account for several experimental observations, such as neutrino masses and oscillations, Baryon Asymmetry of the Universe (BAU), dark matter and dark energy. The Neutrino Minimal Standard Model (νMSM) is a SM extension that explains these experimental observations by introducing three singlet fermions with masses smaller than the electroweak scale, the so-called Heavy Neutral Leptons (HNLs) [10,11]. This model suggests an explanation for the phenomena that cannot fit into the SM, by introducing the smallest possible number of new particles without adding any new physical principles, such as supersymmetry or extra dimensions, or new energy scales, like the Grand Unified scale. Within the νMSM, the leptonic sector has the same structure as the quark sector, which means every left-handed fermion has its right-handed counterpart. This model is consistent with the data on neutrino oscillations, provides a candidate for a dark matter particle, which is the lightest of the newly introduced singlet fermions, and can explain the BAU [11]. A crucial feature of the νMSM is the relatively small mass scale of the new neutral leptonic states considered, which allows for possible direct searches of these particles. In this Chapter, the Neutrino Minimal Standard Model is introduced, based on the work detailed in [12].

1.1 Key features of the Neutrino Minimal Standard Model

The νMSM contains 18 new parameters with respect to the SM:

- 3 Majorana masses for singlet fermions;
- 3 Dirac masses associated with the mixing between left-handed and right-handed neutrinos;

- 6 mixing angles;
- 6 CP-violating phases.

These 18 parameters can describe any pattern (and in particular the observed one) of masses and mixings of active neutrinos, which is characterised by 9 parameters only (3 active neutrino masses, 3 mixing angles and 3 CP-violating phases) [10,11,13]. The choice of a small mass scale for singlet fermions leads to small values of the Yukawa coupling constants, at the level of $(10^{-6}, 10^{-12})$ [10, 14, 15].

Although the νMSM does not present any extra stable particle in comparison with the SM, the lightest singlet fermion, N_1, may have a lifetime τ_{N_1} greatly exceeding the age of the Universe, playing a role as a dark matter candidate and likely having a mass in the O(10) keV/c^2 region [16–19]. No upper limit on the mass of sterile neutrinos exists, as they could be produced in interactions beyond the νMSM [20–22]. An astrophysical lower bound on their mass is 0.3 keV/c^2, following from the analysis of the rotational curves of dwarf spheroidal galaxies [23].

In 1967, Andrei Sakharov proposed a set of three necessary conditions that a mechanism must satisfy to produce matter and antimatter at different rates, causing the BAU. These are [24]:

- baryon number violation;
- C-symmetry and CP-symmetry violation;
- interactions out of thermal equilibrium.

The baryon number B and the lepton number L are not conserved in the νMSM. L is violated by the Majorana neutrino masses, while $B + L$ is broken by the electroweak anomaly, which ensures that the first Sakharov condition is fulfilled. In the νMSM, the CP-violating phase of the quark sector alone would not be enough to fulfill the second Sakharov condition, which is achieved by adding the 6 extra phases of the lepton sector. Moreover, the νMSM contains extra degrees of freedom, the sterile neutrinos, which may be out of thermal equilibrium, since their Yukawa couplings to ordinary fermions are very small. This ensures the validity of the third Sakharov condition as well.

The BAU could be generated through CP-violating sterile neutrino oscillations, provided that the sterile neutrino masses are sufficiently small. In fact, for small Majorana masses, the total lepton number of the system, defined as the lepton number of active neutrinos plus the total helicity of sterile neutrinos, is conserved and equal to zero during the evolution of the universe. However, because of oscillations,

the lepton number of active neutrinos becomes different from zero and gets transferred to the baryon number. For sterile neutrino masses exceeding 20 GeV/c^2, the mechanism does not work as the sterile neutrinos equilibrate [25].

The phenomenological success of the νMSM requires several fine tunings: one of the singlet fermion masses should be in the O(10) keV/c^2 region, to provide a candidate for dark matter, while two other masses would have to be much larger but almost degenerate, to enhance the CP-violating effects in the sterile neutrino oscillation sector, leading to the BAU [10–12, 25]. Moreover, the Yukawa coupling of the dark matter sterile neutrino should be much smaller than the Yukawa couplings of the heavier singlet fermions, to satisfy cosmological and astrophysical constraints [10, 14].

Within the νMSM, not all 18 new parameters are fixed: the allowed region in parameter space is large and yields a variety of signatures to be tested with different experiments and methods. Moreover, two hierarchies can be defined: normal hierarchy means $m_1 < m_2 < m_3$, while inverted hierarchy means $m_3 < m_1 < m_2$.

1.2 The νMSM Lagrangian

The electroweak Lagrangian that describes the νMSM is [12, 26]

$$\begin{aligned} L_{\nu MSM} = L_{SM} + i\bar{\tilde{N}}_i\partial_\mu\gamma^\mu\tilde{N}_i - F_{\alpha i}\bar{L}_\alpha\tilde{N}_i\Phi - F_{\alpha i}\bar{L}_\alpha\gamma^\mu(1-\gamma_5)\tilde{N}_i W_\mu \\ -F_{\alpha i}\bar{\tilde{N}}_\alpha\gamma^\mu Z_\mu N_i - M\bar{\tilde{N}}_2^c\tilde{N}_3 - \frac{\Delta M_{ij}}{2}\bar{\tilde{N}}_i^c\tilde{N}_j + h.c., \end{aligned} \tag{1.1}$$

where L_{SM} is the SM Lagrangian, N_i are the right-handed singlet leptons, Φ and L_α ($\alpha = e, \mu, \tau$) are the Higgs and lepton doublets, respectively, and F is a matrix of Yukawa coupling constants; γ^μ ($\mu = 0, 1, 2, 3$) and γ_5 are the Dirac matrices, W_μ and Z_μ are the W and Z boson fields, respectively, and M is the common mass of two heavy neutral fermions; ΔM_{ij} are the mass differences between each degenerate state and the lightest sterile neutrino, N_1, and produce the small mass splitting of N_2 and N_3 ($\Delta M_{ij} \ll M$).

The mass eigenstates $N_{2,3}$ are related to $\widetilde{N}_{2,3}$ by the unitary transformation

$$\widetilde{N} = U_R N, \tag{1.2}$$

where the 2×2 matrix U_R has the form

$$U_R \simeq \frac{e^{i\phi_0}}{\sqrt{2}} \begin{bmatrix} e^{i\phi_1} & e^{i\phi_2} \\ -e^{-i\phi_2} & e^{-i\phi_1} \end{bmatrix}. \tag{1.3}$$

Here, the phases ϕ_k ($k = 0, 1, 2$) can be expressed through the elements of ΔM_{ij}, the explicit form of which is irrelevant for the νMSM.

The interaction of the mass eigenstates N_2 and N_3 has this form:

$$L_N \simeq -\frac{1}{\sqrt{2}} F_{\alpha i} \bar{L}_\alpha (N_2 + N_3) \widetilde{\Phi} - \frac{M_2}{2} \bar{N}_2^c N_2 - \frac{M_3}{2} \bar{N}_3^c N_3 + h.c. \tag{1.4}$$

The masses M_2 and M_3 must be almost equal (this is a baryogenesis constraint). The baryon asymmetry generation occurs most effectively if $\Delta M^2 \simeq (2 \text{ keV/c}^2)^2$ [11, 12, 25, 26].

The fact that two heavy fermions are almost degenerate in mass may be important for analysis of the experimental constraints. A coherent combination of $(N_2 + N_3)$ would be created, whereas, in a detector of size l located at a distance L from the production point, an admixture of the $(N_2 - N_3)$ state would occur. This admixture would have an appearance probability of $P \sim \sin \phi^2$, with $\phi = \frac{\Delta M^2 L}{4E}$, E being the HNL energy. For $\frac{\phi l}{L} \gg 1$, coherence effects are not essential and the description of the process in terms of only N_2 and N_3 is adequate. On the other hand, if $\frac{\phi l}{L} \sim 1$, the coherence effects are not negligible, and higher order terms describing the interactions of $(N_2 - N_3)$ with the SM particles must be included. For example, at NA62, if $\Delta M^2 \sim (2 \text{ keV/c}^2)^2$, $l \sim 300$ m $= 1.51 \cdot 10^{18}$ GeV^{-1}, $E \sim 100$ GeV, then $\frac{\phi l}{L} \sim 1.5 \cdot 10^4 \gg 1$, which implies that $N_2 \leftrightarrow N_3$ oscillations can be safely neglected.

The coupling constants $F_{\alpha i}$ can be expressed through the elements of the active neutrino mass matrix M_ν [3, 26, 27], where

$$M_\nu = V^* \cdot diag(m_1, m_2 e^{2i\delta_1}, m_3 e^{2i\delta_2}) \cdot V^\dagger, \tag{1.5}$$

and $V = R(\theta_{23}) \cdot diag(1, e^{i\delta_3}, 1) R(\theta_{13}) R(\theta_{12})$ is the active neutrino mixing matrix.

The coupling F is given by [26]

$$F^2 \simeq \kappa \frac{m_{atm} M}{2 v^2 \epsilon}, \tag{1.6}$$

where $v = 174$ GeV is the Vacuum Expectation Value (VEV) of the Higgs field, $\epsilon \ll 1$, $\kappa \simeq 1(2)$ for the case of normal (inverted) hierarchy and M is the mass of the two degenerate states N_2 and N_3 (considered as unique because of the small difference ΔM_{23}).

In most of the works, the strength of the coupling of a neutral lepton X to charged or neutral currents of flavour α is characterised by $U_{\alpha X}$ and $V_{\alpha X}$. Since two of the HNLs have almost identical couplings, $|U_{\alpha 1}| = |V_{\alpha 1}| = |U_{\alpha 2}| = |V_{\alpha 2}| = |U_\alpha|$. The

overall strength of the coupling is given by

$$U^2 = \sum_{\alpha} |U_{\alpha}^2| = \frac{F^2 v^2}{2M^2}, \tag{1.7}$$

where, for successful baryogenesis, F has to be small enough, namely $F \leq 1.2 \cdot 10^{-6}$ [11, 12, 25, 26]. This leads to the upper bound

$$U^2 < 2\kappa \cdot 10^{-8} \left(\frac{\mathrm{GeV}}{Mc^2}\right)^2. \tag{1.8}$$

It is the smallness of the required coupling strength which makes the search for HNLs a very challenging task, especially for large masses. In the framework of the νMSM, a lower bound on U^2 can also be derived:

$$U^2 < 1.3\kappa \cdot 10^{-11} \frac{\mathrm{GeV}}{Mc^2}. \tag{1.9}$$

Some freedom between Yukawa couplings to different leptonic flavours is allowed, since the Majorana CP-violating phases in the active neutrino mass matrix are not known.

The work presented in this thesis focuses on HNL production from D mesons at the NA62 experiment and its decay to pion-muon final states. The whole chain is proportional to two flavour-specific couplings: one that governs the HNL production, according to the lepton generated together with it, and one that governs the HNL decay (U_{μ}^2 in this case). From this, it follows that the sensitivity of this decay search depends on:

$$S(\sum_{\alpha=e,\mu,\tau} U_{\alpha}^2 U_{\mu}^2) = \sum_{\alpha=e,\mu,\tau} C_{\alpha,\mu} U_{\alpha}^2 U_{\mu}^2, \tag{1.10}$$

where $C_{\alpha,\mu}$ are functions of the couplings themselves and of the HNL mass, and include the effects of acceptance, trigger and selection efficiencies at the NA62 experiment.

Two benchmark models have been chosen for this study. The first one, called "generic", is described by the following ratios:

$$U_e^2 : U_{\mu}^2 : U_{\tau}^2 = 1 : 1 : 1 \tag{1.11}$$

and it allows to study the νMSM with a generic approach, in which all three flavour-specific couplings are considered to have the same strength.

A second scenario, called "tau dominant", has also been chosen:

$$U_e^2 : U_{\mu}^2 : U_{\tau}^2 = 0 : 1 : k, \tag{1.12}$$

where $k \gg 1$ can vary to allow for studying the sensitivity in a two-flavour scenario, where one coupling is dominant with respect to the other and the third is kept negligible with respect to both.

The scenario in which U_τ^2 is dominant compared to U_μ^2, while U_e^2 is zero, has been chosen since it is the model where NA62 could set more restrictive limits for HNL decay searches, with the data set collected in 2016-2018, in the mass region between the kaon and D meson masses. This region has been explored by fewer experiments, with respect to the one below the kaon mass.

The NA62 proton beam is particularly suitable to produce D mesons, which can decay into τ leptons via $D, D_S \to \tau\nu_\tau$, with the τ decaying itself to an HNL via two- or three-body processes (as detailed in Section 1.3.1). Since $BR(D \to \tau\nu_\tau) = 9.91 \cdot 10^{-4}$ [28], the HNL production chain originating from this decay gives a negligible contribution with respect to the one from D_S, being $BR(D_S \to \tau\nu_\tau) = 5.55 \cdot 10^{-2}$ [28]. As it can be seen in Fig. 1.7, in the U_τ^2-enhanced scenario with HNL masses below 1 GeV/c^2, the sum of all production BRs from τ leptons amounts to about 0.6, giving a total contribution of about $2 \cdot 10^{-2}$ when multiplying it for $BR(D_S \to \tau\nu_\tau)$. All BRs of direct production modes from D meson species contribute in a comparable way in that mass region. This shows that NA62 is particularly sensitive to scenarios where the HNL coupling to τ leptons is enhanced, the production chain originates from $D_S \to \tau\nu_\tau$, and the HNL mass is below 1 GeV/c^2.

Information on other relevant theoretical scenarios can be found in Appendix C.

1.3 Heavy Neutral Lepton phenomenology

The semi-leptonic channel $N \to \pi\mu$ has been chosen to perform the decay search discussed in this work. In fact, this is a fully-reconstructible mode that gives the greatest contribution in the mass range below the D meson mass, and it is therefore particularly interesting for the NA62 case. This channel opens at a mass of $\sim$ 0.25 GeV/c^2 (the sum of m_π and m_μ). Therefore, this thesis focuses on the HNL production from D mesons and its subsequent decay to pion-muon final states, in the mass range 0.25 GeV/c^2 $\lesssim m_N \lesssim$ 1.9 GeV/c^2.

It must be noted that, in the benchmark models studied, the HNL is considered to be a Majorana particle. The only effect of this assumption is that rates and BRs are twice what they would be if the HNL were a Dirac particle.

1.3.1 Heavy Neutral Lepton production modes

HNLs are produced through the decays of all SM particles that can generate a light neutrino, where the small mixing between the sterile neutrinos and the SM leptons must be accounted for when computing the BRs of each production mode. In the νMSM framework, sterile neutrinos are produced mostly via virtual W bosons (charged current).

Fig. 1.1 and Fig. 1.2 show the Feynman diagrams of two HNL production modes.

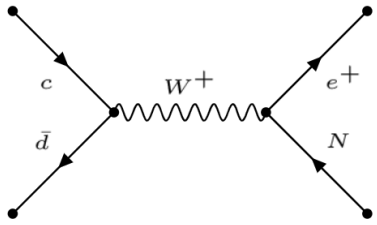

Figure 1.1: *Feynman diagram for the $D^+ \to e^+ N$ production mode.*

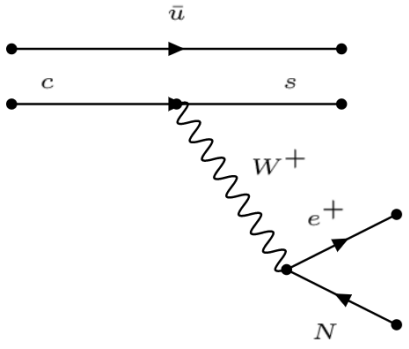

Figure 1.2: *Feynman diagram for the $D^0 \to K^- e^+ N$ production mode.*

For this study, it is considered that an HNL could be produced via any of the dominant decay modes of D, D_S and D^0 mesons, detailed in the following:

$$D \to Nl; \quad l = e, \mu; \tag{1.13}$$

$$D_S \to Nl; \quad l = e, \mu, \tau; \tag{1.14}$$

$$D \to H'Nl; \quad H' = \pi^0, K^0, K^{0*}(895), \quad l = e, \mu; \tag{1.15}$$

$$D^0 \to H'Nl; \quad H' = \pi, K, K^*(891), \quad l = e, \mu; \tag{1.16}$$

$$D_S \to \tau\nu_\tau, \quad \tau \to NH; \quad H = \pi, K, \rho; \tag{1.17}$$

$$D_S \to \tau\nu_\tau, \quad \tau \to Nl\nu_l; \quad l = e, \mu; \tag{1.18}$$

$$D_S \to \tau\nu_\tau, \quad \tau \to Nl\nu_\tau; \quad l = e, \mu. \tag{1.19}$$

The formulae for computing each BR from [12] are detailed in Appendix A. It must be noted that the form factors considered in the formulae of the three-body production modes neglect the kinematic dependence. Nonetheless, the approximation is negligible within this simulation.

To compute the BRs of any three-body production mode, the differential BR formulae detailed in [12] must be numerically integrated in two variables, E_N and

q^2. The former quantity is the energy of the HNL in the mother rest frame, while the latter (also called m^2_{Nl}) is the squared invariant mass of the leptonic pair Nl. For a fixed value of E_N, the minimum and maximum values of q^2 change. The squared invariant mass of the hadron-lepton pair Hl, m^2_{Hl}, is a function of E_N, as seen in eq. 1.22. This means that the maximum and minimum values of $q^2 = m^2_{Nl}$ change for a fixed value of m^2_{Hl}, according to the Dalitz plot of the chosen mode, as seen in Fig. 1.3 and Fig. 1.4. It is therefore necessary to compute these values analytically, before numerically integrating the formula detailed in [12].

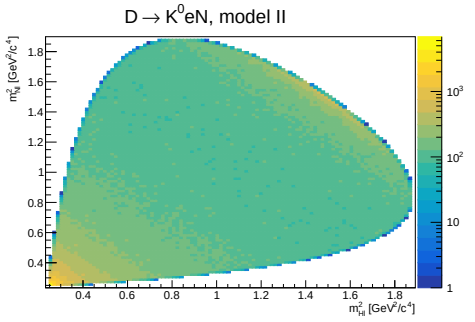

Figure 1.3: *Dalitz plot of the three-body production mode $D \to K^0 eN$, for $m_N = 0.5$ GeV/c^2, for normal hierarchy of the active neutrino masses, generic model ($U_e^2 : U_\mu^2 : U_\tau^2$ =1:1:1) and $U^2 = 1$.*

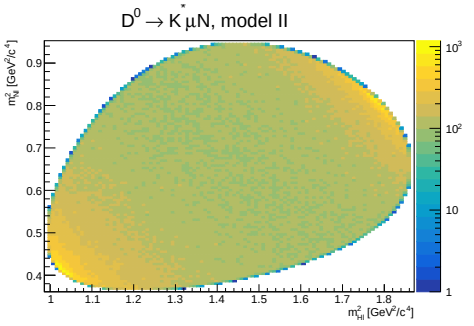

Figure 1.4: *Dalitz plot of the three-body production mode $D^0 \to K^* \mu N$, for $m_N = 0.5$ GeV/c^2, for normal hierarchy of the active neutrino masses, generic model ($U_e^2 : U_\mu^2 : U_\tau^2$ =1:1:1) and $U^2 = 1$.*

To perform this computation, the chosen three-body decay is considered as a sequential two-body decay, where the mother m (either a D meson or a τ lepton) decays to an HNL, N, and a hadron-lepton pair, Hl, and then Hl decays to a hadron, H, and a lepton, l.

First, a scan on E_N is performed between its absolute minimum and maximum values in the mother rest frame. These are given by

$$E_N^{min} = \frac{(m_m^2 - m_{Hl}^{2\,max} + m_N^2)}{2m_m}, \tag{1.20}$$

and

$$E_N^{max} = \frac{(m_m^2 - m_{Hl}^{2\,min} + m_N^2)}{2m_m}. \tag{1.21}$$

Here, m_m is the mother mass, $m_{Hl}^{2\,max} = (m_m - m_N)^2$ is the maximum squared invariant mass of the Hl pair, corresponding to the case where H and l are produced back to back and N is generated at rest (in the mother rest frame); $m_{Hl}^{2\,min} = (m_H + m_l)^2$ is the minimum invariant mass of the Hl pair, corresponding to the case where Hl is produced back to back with respect to N (in the mother rest frame);

m_N is the HNL mass, m_H is the hadron mass and m_l is the lepton mass.

For a fixed value of E_N, several quantities are computed:

$$m_{Hl}^2 = m_m^2 - 2m_m E_N + m_N^2, \tag{1.22}$$

$$E_{l,H} = \frac{(m_{Hl}^2 - m_{H,l}^2 + m_{l,H}^2)}{2m_{Hl}}, \tag{1.23}$$

and

$$|\vec{p}_{N,H,l}| = \sqrt{E_{N,H,l}^2 - m_{N,H,l}^2}, \tag{1.24}$$

where m_{Hl} is the invariant mass of the Hl pair, $E_{l,H}$ are the energies of the lepton and hadron respectively, in the Hl rest frame, and $|\vec{p}_{N,H,l}|$ are the momentum moduli, respectively, of the HNL (in the mother rest frame) and of the hadron and lepton (in the Hl rest frame).

To compute the minimum and maximum values of $q^2 = m_{Nl}^2$ for a fixed E_N, the quantities related to the hadron and lepton must be boosted from the Hl rest frame to the mother rest frame. In the latter frame, the Hl pair has equal and opposite momentum with respect to the HNL:

$$|\vec{p}_{Hl}| = |\vec{p}_N| \tag{1.25}$$

$$E_{Hl} = \sqrt{|\vec{p}_{Hl}|^2 + m_{Hl}^2}, \tag{1.26}$$

$$|\vec{\beta}_{Hl}| = \frac{|\vec{p}_{Hl}|}{E_{Hl}}, \tag{1.27}$$

and

$$\gamma_{Hl} = \frac{1}{\sqrt{1 - |\vec{\beta}_{Hl}|^2}}, \tag{1.28}$$

where $|\vec{\beta}_{Hl}|$ is the modulus of the β velocity and γ_{Hl} is the Lorentz factor of the Hl pair in the mother rest frame.

The minimum value of the invariant mass of the Nl pair, q_{min}^2, is obtained in the configuration where the lepton momentum (in the Hl rest frame) and the HNL momentum (in the mother rest frame) are parallel, whereas the maximum value of the invariant mass of the Nl pair, q_{max}^2, is obtained in the configuration where l and N momenta are anti-parallel (in the rest frames mentioned above). Therefore, for these two extreme cases, the lepton momentum and energy in the mother rest frame, $\vec{p}_l^{\,\prime}$ and $E_l^{\prime}$, and $\vec{p}_l^{\,\prime\prime}$ and $E_l^{\prime\prime}$, respectively, are computed by boosting $\vec{p}_l$ and E_l (in the Hl rest frame) to the mother rest frame, considering that $\vec{p}_l = (|\vec{p}_l|, 0, 0)$, $\vec{p}_l^{\,\prime} = (|\vec{p}_l^{\,\prime}|, 0, 0)$ and $\vec{p}_l^{\,\prime\prime} = (|\vec{p}_l^{\,\prime\prime}|, 0, 0)$, since H and l lie on a plane in the Hl rest frame and the transverse components of all momenta are conserved in a Lorentz boost.

$$|\vec{p}_l^{\,'}| = \gamma_{Hl}(|\vec{p}_l| - |\vec{\beta}_{Hl}|E_l), \tag{1.29}$$

$$E_l^{'} = \gamma_{Hl}(E_l - |\vec{\beta}_{Hl}||\vec{p}_l|), \tag{1.30}$$

$$|\vec{p}_l^{\,''}| = \gamma_{Hl}(-|\vec{p}_l| - |\vec{\beta}_{Hl}|E_l), \tag{1.31}$$

$$E_l^{''} = \gamma_{Hl}(E_l + |\vec{\beta}_{Hl}||\vec{p}_l|), \tag{1.32}$$

where $|\vec{p}_l^{\,'}|$ and $E_l^{'}$ are, respectively, the momentum modulus and the energy of the lepton in the mother rest frame, in the case where the N momentum (in the mother rest frame) and the l momentum (in the Hl rest frame) are anti-parallel, while $|\vec{p}_l^{\,''}|$ and $E_l^{''}$ indicate the same quantities when the HNL and lepton momenta are parallel (in the rest frames mentioned above).

The minimum and maximum values of the invariant mass of the Nl pair can then be computed:

$$q^2_{min} = (E_N + E_l^{'})^2 - (\vec{p}_N + \vec{p}_l^{\,'})^2, \tag{1.33}$$

and

$$q^2_{max} = (E_N + E_l^{''})^2 - (\vec{p}_N + \vec{p}_l^{\,''})^2. \tag{1.34}$$

The differential BR of the chosen three-body production mode can now be integrated between q^2_{min} and q^2_{max} for a fixed value of E_N and then multiplied by the size of the E_N step used for the scan. This procedure (from eq. 1.22 to eq. 1.34) is repeated scanning on E_N and summing the resulting integrals, to compute the BR of the chosen mode.

Fig. 1.6 and Fig. 1.7 show the BRs of all listed production modes, as a function of the HNL mass (for masses up to m_{D_S}), according to the models described in Section 1.2. Here, the choice of setting $U^2 = 1$ is arbitrary and it is only used when plotting the BRs, while a range suitable to the νMSM framework is used in the following Chapters when computing the NA62 sensitivity to $N \to \pi\mu$ decays. Moreover, if the overall HNL coupling to SM leptons had a large enough value ($U^2 \sim 1$), it would affect the D meson lifetime, which would be smaller than the predicted one. Therefore, U^2 values must be small enough to be consistent with such experimental measurements.

Several considerations can be made for the production modes plotted in Fig. 1.6, where the chosen scenario is $U_e^2 : U_\mu^2 : U_\tau^2 = 1 : 1 : 1$.

The $D_S \to N\tau$ channel is the process with the lowest kinematic endpoint, due to the mass difference $m_{D_S} - m_\tau$.

When a production mode reaches its kinematic endpoint, its BR starts to decrease, due to the shrinking of the available phasespace.

The two-body leptonic decays $D \to Ne$ and $D_S \to Ne$ are not helicity-suppressed compared to $D \to N\mu$ and $D_S \to Nl$ ($l = \mu, \tau$) respectively, as it happens to the analogous modes involving a SM neutrino. This is due to the fact that HNLs are massive particles and their helicity can, therefore, be left or right.

Moreover, when the HNL mass approaches the SM neutrino mass and becomes negligible, all BRs approach the values of the analogous modes involving SM neutrinos.

To have all production modes plotted on the same scale in Fig. 1.6, the τ lepton modes have not been multiplied by $BR(D, D_S \to \tau\nu_\tau)$.

In the mass range exploited for this study, namely $(m_\pi + m_\mu) \leq m_N \leq m_{D_S}$, two modes, $D_S \to Ne$ and $D_S \to N\mu$, give the greatest contributions, since their phasespaces are the largest of all considered production modes.

Analogous considerations can be made for the modes shown in Fig. 1.7, where the chosen scenario is $U_e^2 : U_\mu^2 : U_\tau^2 = 0 : 1 : 10$. By neglecting the U_e^2 coupling, all production modes involving electrons are switched off, while the ones where τ leptons are involved are enhanced (compared to Fig. 1.6), due to the value taken by U_τ^2. Production modes that include muons are still present, due to $U_\mu^2 = 1$.

A more detailed understanding of the BRs shown in Fig. 1.6 and Fig. 1.7 can be achieved by comparing three relevant mass points between the two plots: $m_N = 0.3$ GeV/c^2, 1 GeV/c^2 and 1.8 GeV/c^2.

At $m_N = 0.3$ GeV/c^2, in the generic scenario of Fig. 1.6, three-body production modes are dominant with respect to the two-body ones. This is true also in the tau-dominant scenario (Fig. 1.7), where all production modes involving an electron are suppressed and the ones from τ leptons are enhanced.

For HNLs of a 1 GeV/c^2 mass, in the generic scenario, the three-body production modes are subdominant with respect to the $D_S \to Ne$ and $D_S \to N\mu$ ones. In the tau-dominant case, the $D_S \to Ne$ mode is removed, while the $D_S \to N\mu$ channel gives comparable contribution to the three-body production modes from τ leptons, which are enhanced.

At $m_N = 1.8$ GeV/c^2, only the two-body channels $D, D_S \to Ne$ and $D, D_S \to N\mu$ are still open, with the D_S ones being dominant. In the case shown in Fig. 1.7, the $D, D_S \to Ne$ channels are removed, while the $D \to N\mu$ one is subdominant with respect to $D_S \to N\mu$.

Information on the HNL production modes within other relevant theoretical scenarios can be found in Appendix C.

1.3.2 Heavy Neutral Lepton decay modes

Several quantities need to be studied as a function of the coupling U^2, to perform this decay search. The HNL lifetime depends on its total decay width, which is the sum of all possible HNL partial decay widths scaled by their specific-flavour coupling. For this reason, all main HNL decay modes, for masses up to 1.9 GeV/c^2, have been considered.

Semi-leptonic and leptonic HNL decay channels to SM particles are open, while decay modes to a sterile neutrino of a different leptonic species, such as $N \to N_\alpha N_\beta \bar{N}_\beta$ ($\alpha = e, \mu, \tau$ and $\beta = e, \mu, \tau$) are strongly suppressed. All the decays are proportional to the mixing between HNLs and SM leptons they decay into, and lepton number and lepton-family number are conserved.

Fig. 1.5 shows the Feynman diagram of the $N \to \pi\mu$ decay mode chosen for the searches presented in this thesis.

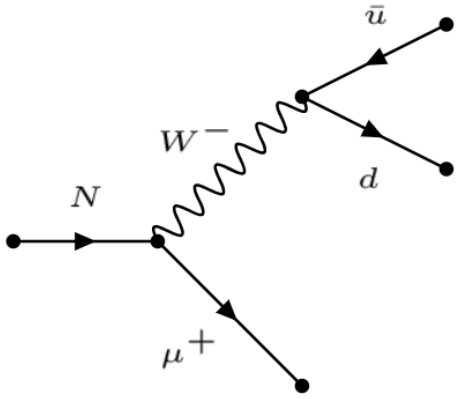

Figure 1.5: *Feynman diagram for the chosen $N \to \pi\mu$ decay mode.*

Several dominant HNL decay modes are listed in [12] and in the following:

$$N \to H\nu_l; \quad H = \pi^0, \rho^0, \eta, \eta', \quad l = e, \mu, \tau; \tag{1.35}$$

$$N \to Hl; \quad H = \pi, K, \rho, \quad l = e, \mu, \tau; \tag{1.36}$$

$$N \to \nu_\alpha \nu_\beta \bar{\nu}_\beta; \quad \alpha = e, \mu, \tau, \quad \beta = e, \mu, \tau; \tag{1.37}$$

$$N \to l_\alpha \bar{l}_\beta \nu_\beta; \quad \alpha = e, \mu, \tau, \quad \beta = e, \mu, \tau; \tag{1.38}$$

$$N \to l_\alpha \bar{l}_\alpha \nu_\beta; \quad \alpha = e, \mu, \tau, \quad \beta = e, \mu, \tau. \tag{1.39}$$

All other decay modes have been excluded from this study. Nonetheless, the validity of this work in this respect holds and is explained in Chapter 3.

The formulae for computing each partial decay width and BR are detailed in

Appendix B.

In Fig. 1.8 and Fig. 1.9, the partial decay widths of all mentioned decay modes are shown. Fig. 1.10 to Fig. 1.11 display the BRs of all the decay modes (which are the partial decay widths normalised to the total decay width), according to the models described in Section 1.2. Here, the choice of setting $U^2 = 1$ is arbitrary and it is only used when plotting the BRs, while a range suitable to the νMSM framework ($10^{-10} \leq U^2 \leq 10^{-1}$) is used in the following Chapters when computing the NA62 sensitivity to $N \to \pi\mu$ decays.

Several observations can be made about the BRs shown in Fig. 1.10. All BRs have a kinematic startpoint that depends on the sum of masses of the HNL decay products. The $N \to \nu\nu\nu$ startpoint is close to zero, due to the negligible masses of SM neutrinos, while the $N \to ee\nu$ channel opens at $m_N = 2m_e + m_\nu \sim 1$ MeV/c^2.

The $N \to e\tau\nu$, $N \to \mu\tau\nu$ and $N \to \pi\tau$ decay modes give negligible contributions to this study, since they open at $m_N > 1.8$ GeV/c^2, which is close to the D_S mass that marks the kinematic endpoint for HNLs to be produced from D mesons.

For $m_N < 0.5$ GeV/c^2, the trend of several decay modes is non trivial, due to different channels opening almost simultaneously. Analogous considerations apply to the partial decay widths plotted in Fig. 1.8.

Concerning the decay modes shown in Fig. 1.11, similar observations to the ones in Fig. 1.10 can be made, considering that modes involving electrons, such as $N \to \pi e$, $N \to Ke$ and $N \to \rho e$, are switched off due to U_e^2 being neglected.

BRs of modes involving muons are present ($U_\mu^2 = 1$), while τ modes are enhanced, due to the choice $U_\tau^2 = 10$.

The three-body decays $N \to el\nu$ ($l = e, \mu, \tau$) are present because the flavour-specific coupling by which they are scaled depends on the species of the SM neutrino produced. For example, a process such as $N \to ee\nu_e$ is proportional to U_e^2 and is therefore neglected in this scenario, while $N \to ee\nu_\alpha$ ($\alpha = \mu, \tau$) is still present.

The $N \to \pi e$ and $N \to \pi\mu$ decays are the modes that give the largest contributions in the explored mass range of $(m_\pi + m_\mu) < m_N < m_{D_S}$, considering that only two-body decays are fully reconstructible at NA62. The choice of studying $N \to \pi\mu$ decays for this thesis is motivated by the fact that at NA62 a trigger for $\pi\mu$ final states is simpler than one for πe.

Analogous considerations apply to the partial decay widths plotted in Fig. 1.9.

A more detailed understanding of the BRs shown in Fig. 1.10 and Fig. 1.11 can be achieved by comparing three relevant mass points between the two plots: $m_N =$ 0.3 GeV/c^2, 1 GeV/c^2 and 1.8 GeV/c^2.

For an HNL of a 0.3 GeV/c^2 mass, in the generic scenario, the $N \to \pi^0\nu$, $N \to \pi e$ and $N \to \pi\mu$ decay modes are dominant, the $N \to \nu\nu\nu$, $N \to ee\nu$, $N \to e\mu\nu$ and

$N \to \mu\mu\nu$ channels are negligible, and all other modes are not kinematically open. In the tau-dominant case, only the $N \to \pi^0\nu$ and $N \to \pi\mu$ modes are dominant, while the $N \to \pi e$ one is suppressed, and $N \to \nu\nu\nu$, $N \to ee\nu$, $N \to e\mu\nu$ and $N \to \mu\mu\nu$ are negligible.

At $m_N = 1$ GeV/c^2, all kinematically-open decay modes give comparable contribution in both the generic and tau-dominant scenarios, but in the latter all modes involving third (first) generation leptons and neutrinos are enhanced (suppressed).

For HNLs of a 1.8 GeV/c^2 mass, in the generic scenario the $N \to \pi^0\nu$, $N \to \pi e$ and $N \to \pi\mu$ processes are subdominant, while the others are comparable to the case where $m_N = 1$ GeV/c^2. This is also true in the tau-dominant case, considering that several modes are enhanced (suppressed) because they are proportional to U_τ^2 (U_e^2).

Information on the HNL decay modes within other relevant theoretical scenarios can be found in Appendix C.

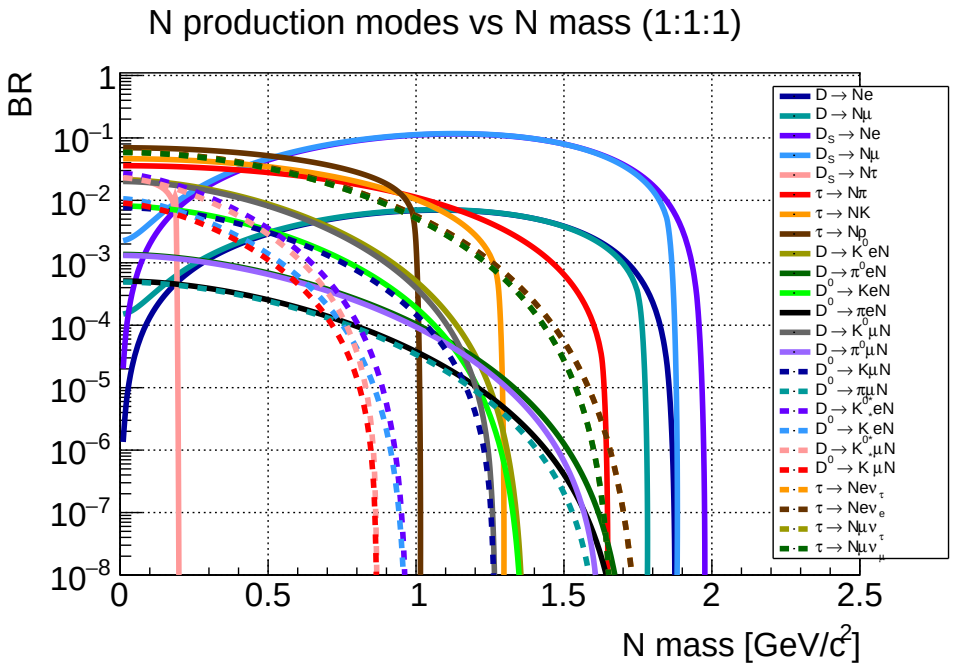

Figure 1.6: *BRs for HNL production modes as a function of the HNL mass, for normal hierarchy of the active neutrino masses and for the generic model ($U^2 = 1$ and $U_e^2 : U_\mu^2 : U_\tau^2$ =1:1:1).*

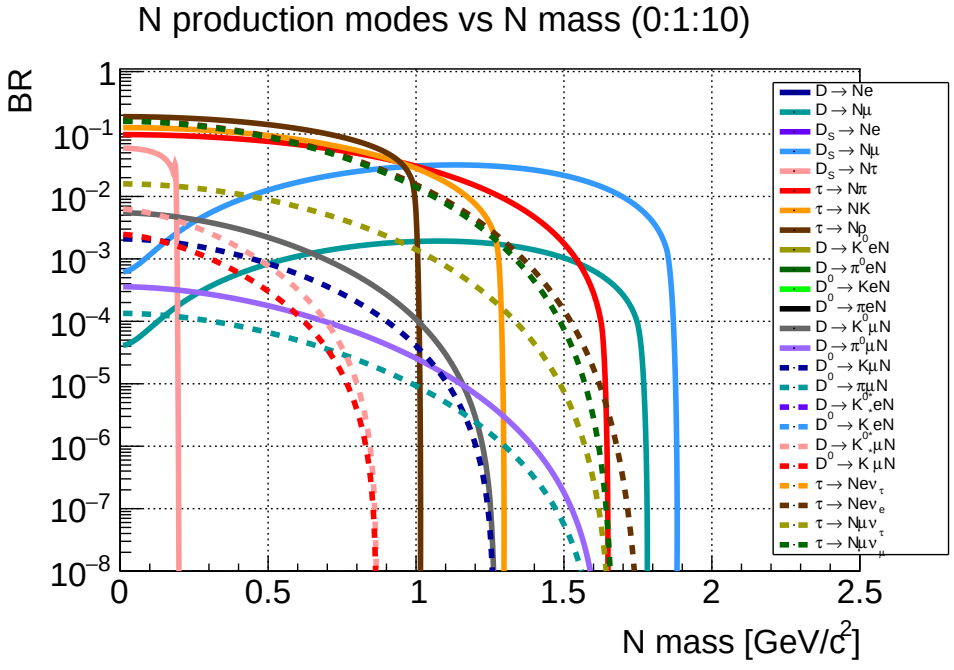

Figure 1.7: *BRs for HNL production modes as a function of the HNL mass, for normal hierarchy of the active neutrino masses and for the tau-dominant model ($U^2 = 1$ and $U_e^2 : U_\mu^2 : U_\tau^2$ =0:1:10).*

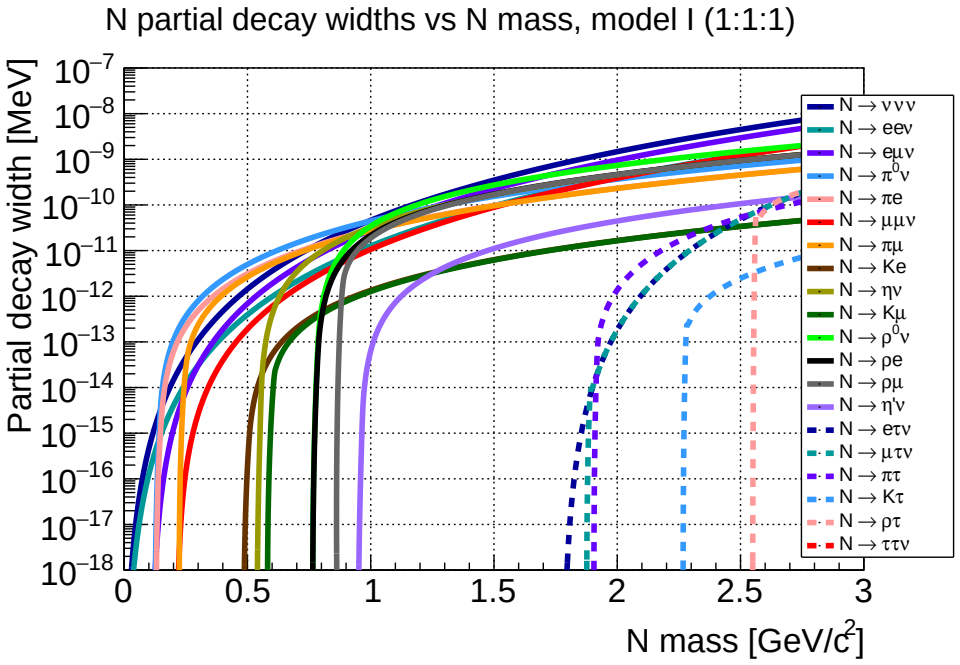

Figure 1.8: *HNL partial decay widths as a function of the HNL mass, for the generic model ($U^2 = 1$ and $U_e^2 : U_\mu^2 : U_\tau^2 = 1{:}1{:}1$) and normal hierarchy of the active neutrino masses.*

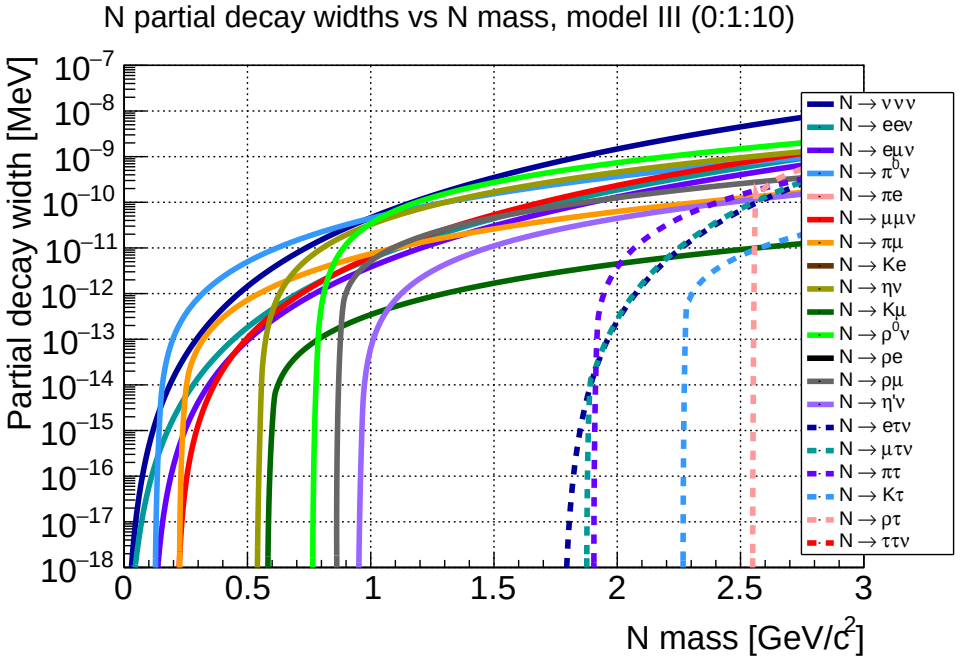

Figure 1.9: *HNL partial decay widths as a function of the HNL mass, for the tau-dominant model ($U^2 = 1$ and $U_e^2 : U_\mu^2 : U_\tau^2 = 0{:}1{:}10$) and normal hierarchy of the active neutrino masses.*

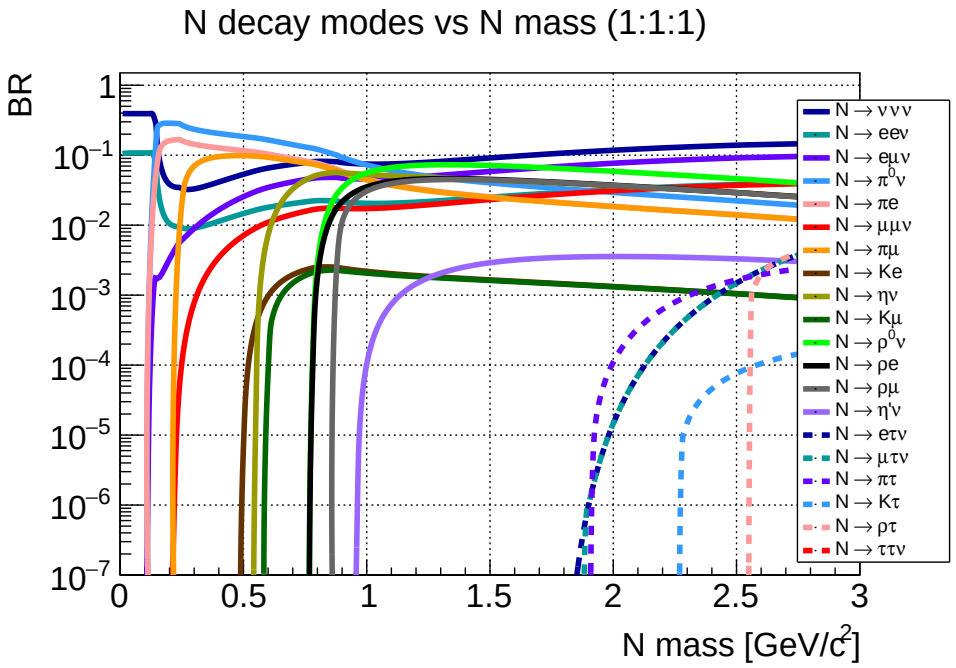

Figure 1.10: *BRs for HNL decay modes as a function of the HNL mass, for the generic model ($U_e^2 : U_\mu^2 : U_\tau^2 = 1{:}1{:}1$), normal hierarchy of the active neutrino masses and $U^2 = 1$.*

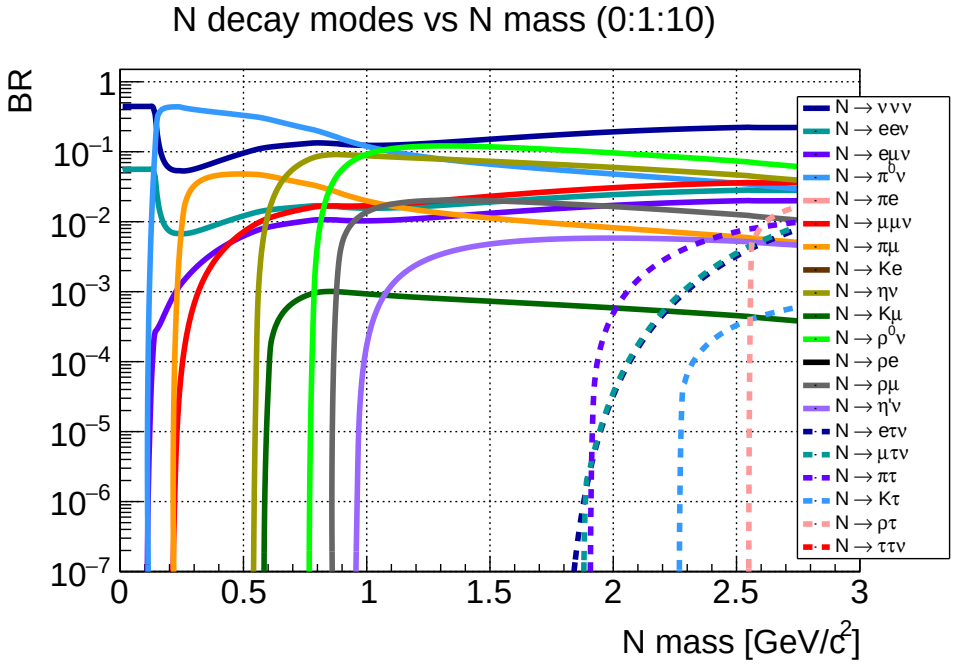

Figure 1.11: *BRs for HNL decay modes as a function of the HNL mass, for the tau-dominant model ($U_e^2 : U_\mu^2 : U_\tau^2 = 0{:}1{:}10$), normal hierarchy of the active neutrino masses and $U^2 = 1$.*

1.4 Status of Heavy Neutral Lepton searches

1.4.1 Techniques and general current status

Two classes of experimental techniques have been exploited so far to search for HNLs. These are decay searches, in which the final states of a specific decay mode are reconstructed; and production searches, in which the emission of an HNL is deduced from the study of the missing mass distribution (defined as the squared difference between the four-momenta of the initial and visible final states).

The decay search technique looks for specific HNL decay products and is used in the so-called "beam-dump" experiments. A high-intensity proton beam is delivered to a fixed target for meson production (mainly kaons, D and B mesons). Their decay products, together with the beam remnants, are completely absorbed by a shield, so that only feebly interacting particles can survive, passing through the shield. If those particles are long-lived enough, they can reach the fiducial volume and decay to SM final states via charged or neutral current interactions.

The bounds obtained from searches for HNL decays into visible particles are in general less robust than the ones coming from production searches. In fact, these searches are model dependent and the bounds obtained with HNL visible decays would be weakened if the HNLs had dominant decay modes into invisible particles.

Searches have been performed for HNL decays to selected final states, below the D meson mass. The $N \to e\mu\nu_e$ decay has been explored by PS191 [29], whereas $N \to e^+e^-\nu_e$, $N \to \mu^+\mu^-\nu_\mu$, $N \to e^+\mu^-\nu_\mu$ and $N \to e^-\mu^+\nu_e$ processes have been studied by CHARM [30]. BEBC focused on $N \to \pi e$ [31], while NuTeV studied $N \to \mu^+\mu^-\nu_\mu$ decays [32]. The T2K experiment performed decay searches of $N \to l\pi$ and $N \to l_\alpha l_\beta \nu$ $(\alpha, \beta = e, \mu)$ [33].

The only experiment able to exclude a region allowed by BAU was PS191, for masses below 350 MeV/c^2 [29].

Production searches have been performed in $K, \pi \to l\nu_l$ decays (where $l = e, \mu$). If an HNL exists, the distribution of the missing mass $m^2_{miss} = (p_K - p_l)^2$ is expected to have a peak at the HNL mass. No peak has been observed so far, allowing upper limits to be set on the coupling of HNLs to SM leptons as a function of the HNL mass. The bounds set in these searches are more robust than the decay serach ones because they only assume that an HNL exists and mixes with a SM neutrino and are, therefore, less model dependent.

The production search technique has been exploited in several general-purpose experiments, to look for HNL production below the kaon mass. The PiENu experiment searched for $\pi^+ \to e^+N$ and $\pi^+ \to \mu^+N$ decays [34], whereas KEK, NA62 and E949 studied $K^+ \to \mu^+N$ and $K^+ \to e^+N$ processes [35], [36], [37], [38]. Limits on

the HNL mixing to electrons have also improved by testing lepton universality and re-analyzing data for the measurements of $R^{\pi}_{e\mu} = \frac{BR(\pi^+ \to e^+ \nu_e)}{BR(\pi^+ \to \mu^+ \nu_\mu)}$, $R^{K}_{e\mu}$ and $R^{D_S}_{e\tau}$ [39].

1.4.2 Status of searches and future prospects for the tau-dominant scenario

A status of decay searches with HNLs coupling only to third generation leptons is discussed in the following, to allow for comparison with results presented in this work. Further details can be found in the Beyond the Standard Model (BSM) working group of the Physics Beyond Collider (PBC) report [40]. This is an exploratory study aimed at exploiting the full scientific potential of the CERN accelerator complex and scientific infrastructures through projects complementary to the LHC and other possible future colliders.

Two experiments have set limits on U^2_τ as a function of the HNL mass, so far, as seen in Fig. 1.12. CHARM set bounds on the mixing in the mass range 10-290 MeV/c^2, by re-interpreting the null result of a search for events produced by the decay of neutral particles with electrons in the final state, using the neutrino flux produced by 400 GeV/c protons on a solid copper target [41]. DELPHI studied HNL decays to two-body final states at the LEP (Large Electron Positron) collider [42].

According to the PBC studies, several experiments will be able to set more restrictive limits on HNL coupling to τ leptons, below the B meson mass, in a 10-15 year time scale. This is shown in Fig. 1.12, where shorter timescale projections (2021-2023) for NA62 are plotted as well. A brief description of each experiment considered in Fig. 1.12 follows.

NA62 will perform a second phase of data-taking at the restart of SPS operations, after the CERN long shutdown ending in 2021. This phase foresees a data-taking period dedicated to HSM and DF searches and the opportunity of collecting 10^{18} POT. Construction of a new scintillator hodoscope is ongoing, which will be commissioned by 2021 and installed at the beginning of the NA62 decay region, to improve background rejection for HSM and DF searches.

FASER, a new approved experiment to be built downstream of the ATLAS interaction point at the LHC, will look for a plethora of light, feebly-interacting HSMs [43].

SHiP is a new experiment to be installed at the SPS, specifically designed to search for a wide range of HSMs with the so-called "beam dump" technique, where a high-intensity beam impinges on a thick, dense material to potentially produce feebly interacting particles [44].

MATHUSLA200, a dedicated large-volume displaced vertex detector for the high-

luminosity upgrade of LHC, will be installed on the surface above ATLAS or CMS, to look for neutral, long-lived particles [45].

CODEX-b is a new proposed detector element at the LHCb experiment, designed to search for displaced decays of BSM long-lived particles [46].

Finally, FCC-ee, the Future Circular Collider with high-luminosity e^+e^- beams that could be built as an expansion of the LHC, could search for decays of HNLs produced in Z boson decays [40]. This is a long-term project expected to be commissioned in 30-40 years.

In Fig. 1.12, Big Bang Nucleosynthesis (BBN) and see-saw constraints are visible. An HNL with parameters to the left of the BBN line would live sufficiently long in the early universe to result in an overproduction of primordial Helium-4 [40, 47]. Below the see-saw limit, the mixing of the HNL with active neutrinos becomes too weak to produce the observed pattern of neutrino flavour oscillations [40].

Experiments such as NA62, SHiP, FASER, MATHUSLA200 and CODEX-b will be able to exploit a wider range of HNL decay searches and to explore broader regions of the HNL mixing to electrons, U_e^2, and to muons, U_μ^2, as a function of the HNL mass. More details on this can be found in Appendix D.

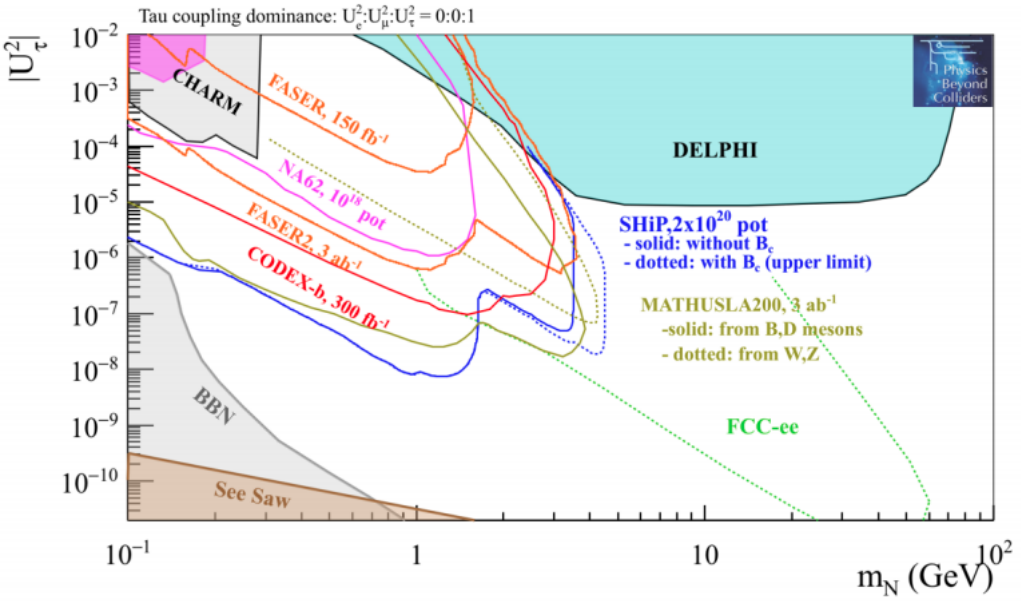

Figure 1.12: *Sensitivity at 90% Confidence Level (CL) to HNLs with coupling to the τ lepton generation only, for a scenario in which $U_e^2 : U_\mu^2 : U_\tau^2 = 0{:}0{:}1$. Current bounds (filled areas), 2021-2023 projections for NA62, and 10-15 years prospects (solid and dotted curves) for PBC projects (SHiP, MATHUSLA200, CODEX-b and FASER). Projections from FCC-ee are also shown. BBN and see-saw model constraints are visible [40].*

Chapter 2

The NA62 experiment at CERN

2.1 The NA62 physics programme

The main goal

NA62 is a fixed-target experiment located in the CERN North Area. Its main goal is to measure the BR of the rare decay $K^+ \to \pi^+\nu\bar{\nu}$ to a 10% precision, by collecting 100 SM events [9].

Kaons have always played a pivotal role in experimental flavour physics. Their study led to the postulation of the strangeness quantum number, while the neutral kaon sector provided the first evidence of both direct and indirect CP violation [48, 49].

The $K^+ \to \pi^+\nu\bar{\nu}$ decay is rare due to the GIM mechanism, which forbids Flavour-Changing Neutral Current (FCNC) processes at tree level, and it proceeds via a top-quark loop. Therefore, its BR is proportional to $|V_{td}|^2$, the second smallest element of the CKM matrix. The SM prediction of $BR(K^+ \to \pi^+\nu\bar{\nu})$ has a precision of 10%, so an experimental measurement of the same precision would allow for deepening knowledge on the CKM matrix element and would be sensitive to PBSM [50].

By analyzing the data sample collected in 2016, NA62 has put an upper limit on $BR(K^+ \to \pi^+\nu\bar{\nu}) < 14 \cdot 10^{-10}$ at 95% confidence level (CL) [51].

Other searches

Beside the $K^+ \to \pi^+\nu\bar{\nu}$ measurement, NA62 performs a broad programme of rare and forbidden decays and HSM and DF searches, by exploiting the high flux of protons delivered to the experiment ($\sim 10^{12}$ protons/s).

Limits have been set on Lepton-Number Violating (LNV) kaon decays recently, namely $K^+ \to \pi^- e^+ e^+$ and $K^+ \to \pi^- \mu^+ \mu^+$. Lepton-Flavour Violating (LFV) processes, such as $K \to \pi\mu e$, are currently studied at NA62 as well [52].

HNLs can be studied by exploiting both the production search technique (as mentioned in Section 1.4) [36, 37] and the decay search technique (this thesis). An HSM that is looked for at NA62 is the Dark Photon (DP), by performing production searches in π^0 decays to a SM photon and a DP [53]. Decays of Axion-Like Particles (ALPs) to two SM photons are also studied at the NA62 experiment.

2.2 The kaon operation mode

Besides dedicated data-taking periods in different conditions, NA62 runs in kaon mode for the majority of the time. During each 3 s long beam-delivery period (called "spill" or "burst"), the 400 GeV/c proton beam extracted from the SPS impinges on the T10 target, with a nominal beam intensity of $\sim 3 \cdot 10^{12}$ POT per burst. During the 2016-2018 data taking, the beam intensity varied from 30% to 90% of the nominal one. This was due to SPS beam instability and large instantaneous beam intensity fluctuations that the NA62 data acquisition system could not sustain. As a consequence, the beam intensity was kept lower than the nominal one in order to improve the data acquisition efficiency. In stable conditions, the instantaneous beam intensity fluctuations throughout a single spill, was observed to have variations amounting to less than 10%.

The secondary, positive K12 beam is extracted with an average momentum of 75 GeV/c, a 6% content of kaons (the remaining is $\sim$ 70% pions, $\sim$ 23% protons and $\sim$ 1% muons) and an instantaneous rate of 750 MHz, at nominal beam intensity [54]. This intensity can be decreased by either pulling closer the set of copper beam collimators (called TAXes) or by regulating the intensity of the primary proton beam delivered by the SPS.

The majority of the NA62 programme is studied in kaon mode, namely: the $K^+ \to \pi^+\nu\bar{\nu}$ process, LFV and LNV kaon decays, and processes involving HSMs such as DPs and DFs such as HNLs. These mediators can be produced in K, D and B meson decays generated via interaction of the beam protons with the beryllium target itself.

Data for HSM and DF searches can be collected in this operation mode during the whole data-taking period, without the need of dedicated runs, by allocating a fraction of the available bandwidth to the so-called "exotic" triggers. However, decays of kaons, pions and muons in the beamline constitute background sources for these studies and must be proved to be kept under control or eliminated.

The data sample analyzed for the HNL decay search discussed in this thesis has been collected in kaon mode during the data-taking period of 2016-2018, at various beam intensities, using the "muon exotic" trigger described in Section 2.5.4. The

full data set collected with this trigger during 2016-2018 corresponds to $2.4 \cdot 10^{17}$ POT, whereas only a subset reconstructed with the NA62 offline framework and corresponding to $1 \cdot 10^{17}$ POT has been analysed for the work detailed in this thesis.

2.3 The beam-dump operation mode

A different operation mode from the kaon one is the beam-dump mode. In this data-taking setup, the beryllium target is pulled up and the TAXes are completely closed, so that they act as a dump for the SPS proton beam. The protons interact with the dump, potentially generating HSMs (direct production) or K, D and B mesons which decay to produce long-lived, feebly-interacting particles (indirect production). Extra intermediate mesons can be produced in the hadronic showers generated by the SPS proton beam, since the TAXes correspond to 22 interaction lengths. This potentially yields enhanced production of HSMs and DFs through secondary interactions [55].

Data samples have been collected in dedicated beam-dump runs during the 2017 data taking, for a total of $2 \cdot 10^{16}$ POT.

Collecting data in beam-dump mode means that the only background sources still present come from muon- and neutrino-induced processes, via their inelastic interaction with the material of the NA62 upstream detectors [55]. Moreover, no beam-intensity restrictions are present, and there is only need for a minimum-bias trigger on charged tracks. On the other hand, this operation mode requires dedicated data-taking runs, which means that a significantly smaller sample (compared to the one in kaon mode) has been collected between 2016 and 2018.

After the current CERN long shutdown, when NA62 resumes data-taking operations, a longer period will be dedicated to the beam-dump mode, with the goal of collecting a sample for HSM and DF studies that corresponds to 10^{18} POT. This will make NA62 competitive to several experiments described in Section 1.4 and able to set more restrictive limits on HSM and DF couplings to SM particles for different searches and theoretical models.

2.4 Experimental strategy for Heavy Neutral Lepton decay searches

At NA62, all the HSM and DF searches performed require the proton beam coming from the SPS to impact either on the beryllium target or on the TAXes, to produce strange, charm and beauty mesons that might decay into HSM particles or

DFs, such as the HNLs. If these mediators are long-lived enough, they can travel to the Fiducial decay Volume (FV) and decay into SM particles.

A typical $N \to \pi\mu$ signature includes a two opposite-charge track vertex displaced from the beam axis, in the FV, and no signal upstream of the fiducial decay region.

In the following, a description of the NA62 apparatus is provided, with special focus on the detectors that are crucial to the HNL searches detailed in this thesis. All the NA62 systems that are not used for the detection of the HNL signal, but are fundamental for the background rejection studies detailed in Chapter 5 and performed on a data set collected in kaon operation mode, have been described as well.

2.5 The NA62 experimental apparatus

The information about the NA62 detectors and subsystems provided here, including schematic layouts and pictures, can be found in [54], together with additional details on construction and performances.

2.5.1 The beam line

The NA62 experiment is located in the CERN North Area. The primary 400 GeV/c proton beam is delivered by the SPS onto T10, a beryllium rod that is 400 mm long and has a 4 mm radius, whose centre marks the origin of the NA62 reference frame. The high-intensity secondary hadron beam, K12, is derived from T10 at a central momentum of roughly 75 GeV/c. Since all downstream detectors have a central beam hole, the great majority of the secondary beam particles continue along the beam axis without being detected downstream.

Before the start of the decay volume, a series of magnets and collimators (including the TAXes) is used to shape, focus and steer the K12 beam.

The decay region is contained in the first 65 m of a large 117 m long tank, starting at $Z = 102.4$ m downstream of the target. The pressure in the tank is kept at $\sim 10^{-6}$ mbar by several cryo-pumps.

Downstream of the last NA62 detector, the beam is finally absorbed in a beam dump composed of iron surrounded by concrete.

The K12 beam is not used for the HNL decay searches detailed in this thesis. In fact, HNLs are produced from charmed meson decays generated in the interactions of the SPS proton beam with either the target or the TAXes.

2.5.2 The NA62 detectors

A schematic layout of the NA62 experiment is displayed in Fig. 2.1.

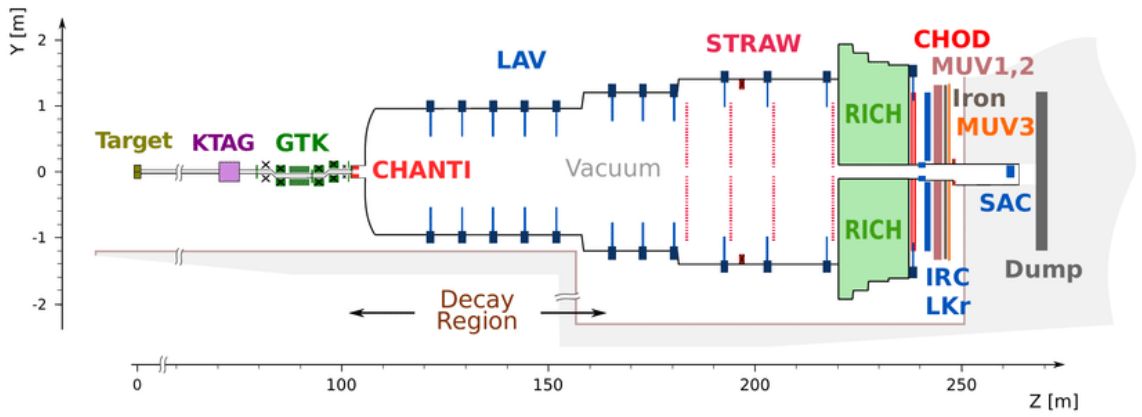

Figure 2.1: *Schematic layout of the full NA62 experimental setup, with all detectors visible [54].*

As K12 is a high-momentum beam, the detector has been designed to be hermetic for particles emitted up to 50 mrad with respect to the Z axis.

A summary of the sub-detector systems is provided in Table 2.1. A description of each subsystem and its purpose for the studies detailed in this thesis is provided as well.

The tracking system

The GigaTracker The GigaTracker (GTK) is designed to provide precision measurements of the momentum, time and position of all the particles in the K12 beam (750 MHz rate). It is located upstream of the fiducial decay volume and consists of three hybrid silicon micro-pixel stations, installed around four dipole magnets arranged as an achromat.

The GTK is not used for HNL decay searches, where no upstream signal is present. In fact, HNLs do not belong to the beam and they would not be detected by the GTK regardless, since they are electrically neutral particles.

The Straw spectrometer The Straw spectrometer is used to measure the momentum and trajectory of the decay products downstream of the fiducial decay volume.

The spectrometer consists of four straw chambers, operated in the vacuum of the decay tank, and the MNP33 large-aperture dipole magnet, located between the second and third chamber. This magnet provides a vertical field integral of about

System	Detector	General purpose	Purpose for HNL searches
Tracking	GigaTracker	Momentum, time and position measurement of all beam particles	Not used
	STRAW	Reconstruction of charged downstream tracks	Reconstruction of final state tracks (charged pions and muons)
Particle ID	KTAG	Identification and time measurement of upstream K^+	Rejection of kaons in time with downstream tracks
	RICH	Downstream track identification ($\pi/\mu/e$ separation)	Trigger
	MUV1 and MUV2	Downstream track identification (π/μ separation)	Not used
Hodoscopes	CHOD and NewCHOD	Time measurement of downstream charged tracks	Trigger; time measurement of downstream charged tracks
Photon veto	LAV	Rejection of photons emitted at 8.5 mrad $\leq \theta \leq$ 50 mrad from the beamline	Rejection of extra activity
	LKr	Rejection of photons emitted at 1.5 mrad $\leq \theta \leq$ 8.5 mrad from the beamline	Rejection of extra activity
	SAV	Rejection of photons emitted at $\theta \leq$ 1.5 mrad from the beamline	Rejection of extra activity
Muon veto	MUV3	Muon identification	Trigger; muon identification
Others	CHANTI	Rejection of inelastic beam interactions in the GTK stations	Rejection of extra activity
	MUV0	Rejection of large-angle downstream π	Not used
	HASC	Rejection of high-momentum π at low angles from the beamline	Not used

Table 2.1: *Summary of the NA62 detector systems, their general purposes and their purposes for the HNL searches detailed in this thesis.*

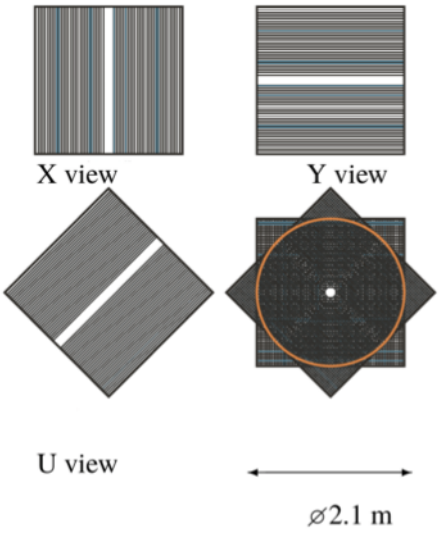

Figure 2.2: *Schematic layout of the four views within a Straw chamber [54].*

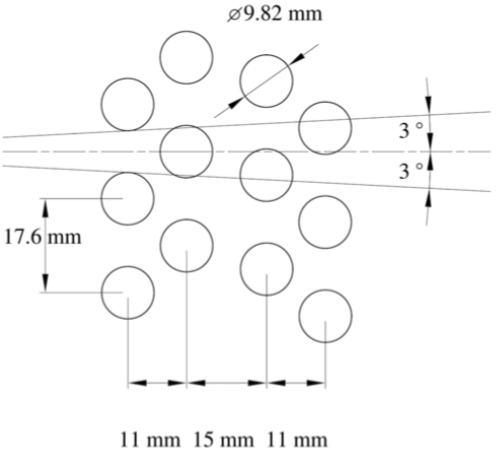

Figure 2.3: *Staggering scheme of the four layers of straw tubes that guarantee at least two hits per view for each track [54].*

0.9 Tm towards the positive Y axis (equivalent to a 270 MeV/c kick towards the negative X axis for positively-charged particles).

The chambers contain four views: the (X, Y) views are placed at (0°, 90°) with respect to the vertical axis, whereas the (U, V) views are rotated with respect to the first two, so that they are at (−45°, 45°) from the Y axis. Each view consists of 448 straw tubes, divided into four layers and staggered to guarantee at least two hits per view. Fig. 2.2 contains a schematic layout of the module orientation in the chambers, while Fig. 2.3 shows the staggering of the straw tubes within a chamber.

The chamber active area is a circle of 2.1 m outer diameter centred on the longitudinal Z axis. A 12 cm wide gap is present at the centre of each view such that, after overlaying the four views, an octagon-shaped hole of 6 cm apothem is created to allow for passage of the beam particles. The straw tubes are filled with a combination of 70% argon and 30% CO_2 at atmospheric pressure. They are coated with a layer of copper, 50 nm thick, and they contain a tensioned gold-plated tungsten anode wire with a diameter of 30 µm.

The track momentum resolution is $\frac{\sigma_p}{p} = 0.3\% \oplus 0.005\% \cdot \frac{p}{GeV/c}$, whereas the angular resolution is $\sigma_\theta = 60\,\mu\text{rad}$, for tracks of momentum $p = 10$ GeV/c, and $\sigma_\theta = 20\,\mu\text{rad}$ at $p = 50$ GeV/c [56].

The Straw spectrometer is a crucial detector for HNL decay searches to pion-muon final states, since both decay products are electrically charged.

The particle identification system

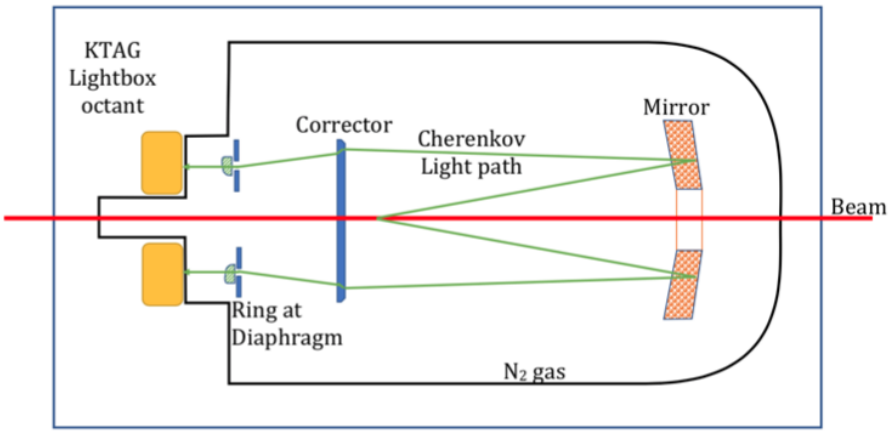

Figure 2.4: *Schematic view of the KTAG tank. The tracing of the K^+ Cherenkov light is visible [54].*

The KTAG The Kaon Tagger (KTAG) is the first detector placed downstream of the T10 target. The KTAG is a Cherenkov detector which identifies the 6% K^+ content of the K12 hadron beam and consists of a nitrogen-filled tank and several photomultiplier (PMT) clusters, called light boxes or sectors. By controlling the pressure in the tank and setting it at 1.7 bar, the opening angle of the Cherenkov light cone can be controlled in such a way that only the rings generated by positive kaons are selected through a diaphragm, after being reflected by a set of spherical mirrors. The light then reaches the KTAG sectors, eight clusters of 48 PMTs each, located in an insulated, cooled Faraday enclosure flushed with nitrogen gas. Fig. 2.4 shows a schematic layout of the KTAG, including the path of Cherenkov light emitted by a positive kaon.

The KTAG is tuned with a pressure and alignment scan to maximise the kaon detection efficiency. The coincidence of signals from multiple sectors is used to timestamp each kaon of the K12 beam [57]. The KTAG time resolution for the individual PMT signals is measured from the difference between the hit time in a PMT and the average time of all signals produced by a beam particle. The time resolution in a single channel is 300 ps while, with 20 PMT signals detected on average per beam kaon (with the average rate of 2.3 MHz/channel at the nominal 45 MHz kaon rate), a kaon time resolution of 70 ps is achieved.

The KTAG is used as a veto for the $N \to \pi\mu$ search, by requiring that the signals sent by five or more KTAG sectors are not in coincidence with the downstream tracks.

The RICH The Ring Imaging Cherenkov (RICH) detector is used for particle identification of the downstream decay products. It is located just downstream of the vacuum tank, and it is used primarily to separate pions, muons and positrons in the momentum range between 15 GeV/c and 35 GeV/c.

The RICH tags downstream particles with a 70 ps time resolution and it can be used in combination with the Straw spectrometer, so that the identification of a track can be inferred from the Cherenkov radius, computed through the momentum measurement provided by the spectrometer.

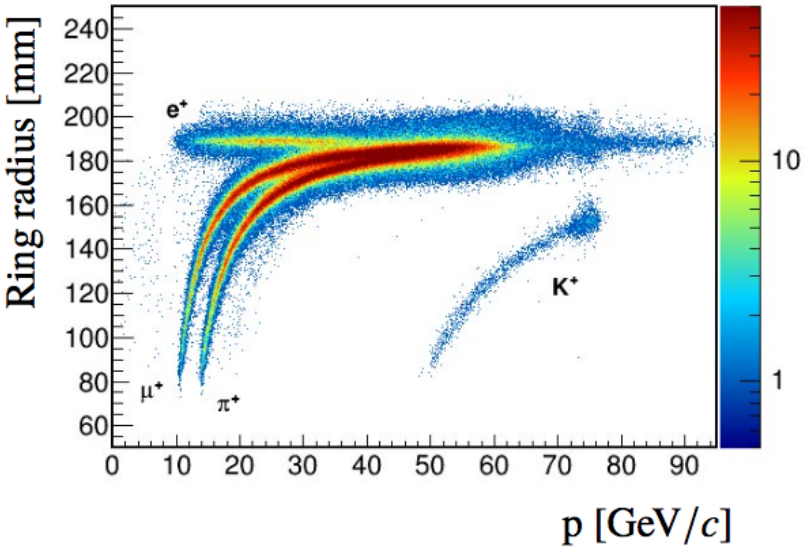

Figure 2.5: *Cherenkov ring radius as a function of particle momentum for electrons, muons, charged pions and scattered beam kaons. Particles with momentum higher than 75 GeV/c are due to muons in the beam halo [54].*

Above 35 GeV/c, the RICH identification efficiency decreases, since the radii of Cherenkov rings produced by different particles start to become more and more similar, as seen in Fig. 2.5. The RICH cannot, therefore, be used for particle identification in HNL decay searches. In fact, the majority of HNL decay products have momenta between 30 GeV/c and 400 GeV/c, a range in which the RICH starts to be less and less efficient. Moreover, one of the two decay products of these DFs is negatively charged, with the RICH not being optimised for detecting these tracks. This is due to the fact that the NA62 apparatus is designed to detect positive particles with the highest possible efficiency (since its main studied decay is $K^+ \to \pi^+\nu\bar{\nu}$). This is achieved by slightly tilting the RICH vessel towards the negative X axis, where positive tracks are deflected by the MNP33 magnet, leaving the positive X axis partially uncovered by this detector.

For these reasons, the particle identification for HNL decay searches is performed by other detectors, described in the following paragraphs.

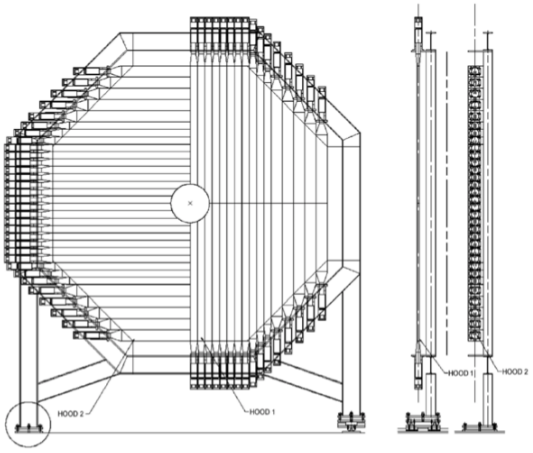

Figure 2.6: *Schematic view of the CHOD. The vertical and horizontal slabs of the two planes are visible [54].*

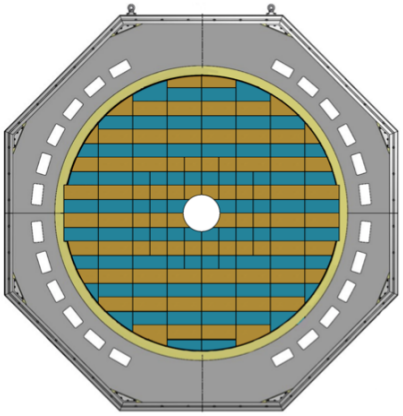

Figure 2.7: *Schematic layout of the NewCHOD [54].*

The MUV1 and MUV2 The MUV1 and MUV2 are two hadronic calorimeters located downstream of the RICH. Their purpose is to provide energy-based separation for pions and muons. Pions deposit some of their energy in the electromagnetic calorimeter upstream of the hadronic calorimeters, then they deposit the remaining energy in the MUV1 and MUV2. Muons, on the contrary, release less energy in all three calorimeters (about 200 MeV), so that they reach the muon detector, further downstream.

The hadronic calorimeter system is not used for the searches detailed in this thesis. The particle identification for HNL decay searches is performed by other detectors, described in the following, namely the LKr and the MUV3, although the MUV1-MUV2 would have been an equally efficient tool for the particle identification required in this study.

The hodoscopes

The CHOD The Charged Hodoscope (CHOD) is a detector used to obtain a fast response to the charged products of K^+ decays. It is located between the RICH and the hadronic calorimeters, and it consists of two consecutive octagonal planes with 64 vertical and 64 horizontal plastic scintillator slabs, as shown in Fig. 2.6. Slab lengths vary from 1.21 m (inner counters) to 0.6 m (outer counters), forming an octagon. The slab thicknesses are 65 mm in the central region close to the beam, where the particle flux is higher, and 99 mm in the outer region [58]. The slabs are read-out at one end by fast PMTs. A central hole is present to allow for the passage of beam particles.

A charged particle traversing the detector produces signals in a single pair of

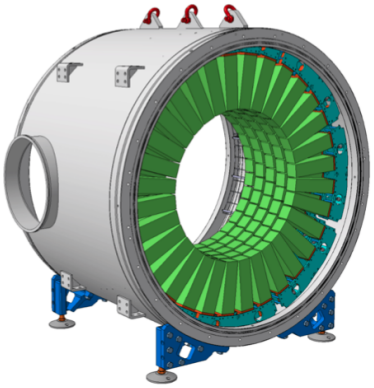

Figure 2.8: *Schematic drawing of a LAV station, with five lead-glass layers visible [54].*

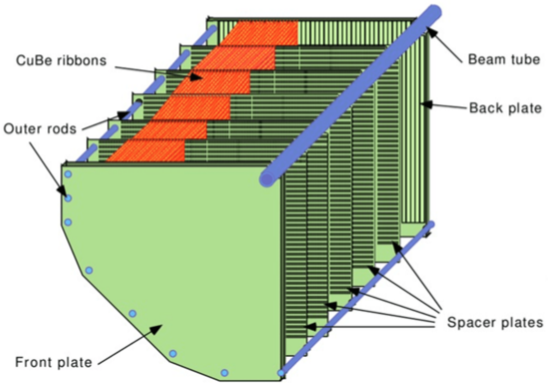

Figure 2.9: *Schematic view of a quadrant of the LKr. The cells traverse the depth of the detector [54].*

slabs from the two planes, from which two time measurements are performed. The time resolution of the CHOD is $\sigma_t = 200$ ps, providing a suitable source for fast minimum-bias triggers.

Since both decay products of HNLs are electrically charged, the CHOD is used to provide precise time measurement for both tracks.

The NewCHOD The NewCHOD is a hodoscope located just upstream of the CHOD, made of a matrix of 152 plastic scintillator tiles, each 30 mm thick (Fig. 2.7). Subdivision of the acceptance surface into tiles leads to an optimised distribution of hit rates, with inner tiles being smaller than outer ones. The beamline runs through the centre of the NewCHOD. The scintillation light from each tile is collected by wavelength-shifting (WLS) fibres and detected by a pair of Silicon PMTs (SiPM).

The detector time resolution is $\sigma_t = 1$ ns. The NewCHOD is used to provide geometrically-based information to be used in the low-level trigger, by defining four quadrants of equal area. These quadrants are used to trigger for decays containing either single or multiple charged tracks.

The photon vetoes

The Large-Angle Veto The Large Angle Veto (LAV) is a system of twelve independent ring-shaped detectors or stations, placed at longitudinal positions between the start of the decay volume and upstream of the CHOD. The LAV covers the angular region of 8.5 mrad $\leq \theta \leq$ 50 mrad with respect to the Z axis, and it is designed to detect photons emitted at wide angles.

Fig. 2.8 displays a single LAV station, containing five layers of lead-glass crystal blocks. High-energy photons interacting with the lead-glass blocks generate electromagnetic showers, which produce Cherenkov light in the material.

The LAV achieves a detection inefficiency of 10^{-4} for photons with energy between 200 MeV and 1 GeV, and it has a time resolution of about 1 ns for photons with energy of about 1 GeV. For these photons, an energy resolution of at least 10% is reached [59].

This subsystem is used as a veto for HNL decay searches.

The Liquid Krypton Calorimeter The Liquid Krypton calorimeter (LKr) is an electromagnetic, quasi-homogeneous calorimeter filled with liquid krypton, kept in a cryostat at a temperature of 120 K. The LKr is located upstream of the hadronic calorimeters, and its main purpose is to veto photons emitted at intermediate angles, 1 mrad $\leq \theta \leq$ 8.5 mrad, with respect to the Z axis. The sensitive volume of the LKr, corresponding to 27 radiation lengths in depth, is divided into quadrants of cells, formed by electrodes aligned along the longitudinal axis of the experiment (Fig. 2.9). In total, 13248 cells cover the transverse face of the detector, allowing for the beam particle passage, with each cell spanning the calorimeter full depth. The signal produced by a particle crossing the LKr is collected by preamplifiers inside the cryostat, directly attached to the calorimeter cells.

The LKr energy resolution is $\frac{\sigma_E}{E} = 1.4\%$ at an energy deposit of 25 GeV, while the spatial and time resolutions are 1 mm and 1 ns.

The LKr is one of the crucial detectors for particle identification in the $N \to \pi\mu$ search detailed in this thesis. In fact, the pion/muon separation is achieved through the study of $\frac{E}{p}$, where E is the deposited energy measured in the LKr and p is the momentum measurement provided by the Straw spectrometer.

The Small-Angle Veto The Small Angle Veto (SAV) consists of two systems, the Intermediate Ring Calorimeter (IRC) and the Small Angle Calorimeter (SAC). The IRC is located just upstream the LKr and wraps directly around the beam pipe, whereas the SAC is the most downstream detector of NA62, installed inside the beam vacuum towards the end of the beam pipe, just upstream of the beam dump. Both are used to detect photons which are emitted almost parallel to the beam, with angles below 1.5 mrad. The detectors are shown in Fig. 2.10 and Fig. 2.11. They are both Shashlik calorimeters that use plastic scintillators as active volume and lead as an absorber.

The inefficiency detection of the SAV system for a single photon has been measured at $7 \cdot 10^{-4}$, for photons with $E \geq 200$ MeV.

The SAV is used as a veto for HNL decay searches.

The muon detector

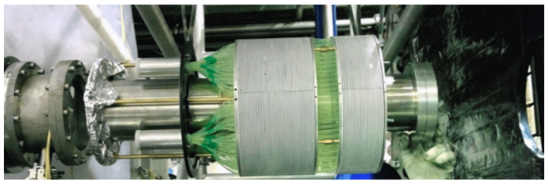

Figure 2.10: *Picture of the IRC, wrapped around the beamline [54].*

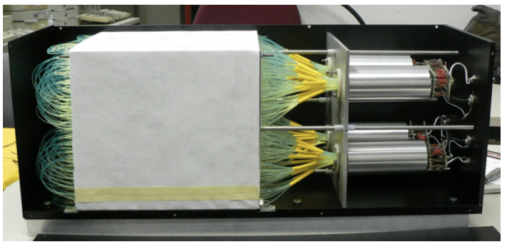

Figure 2.11: *Picture of the SAC, directly inserted into the beamline [54].*

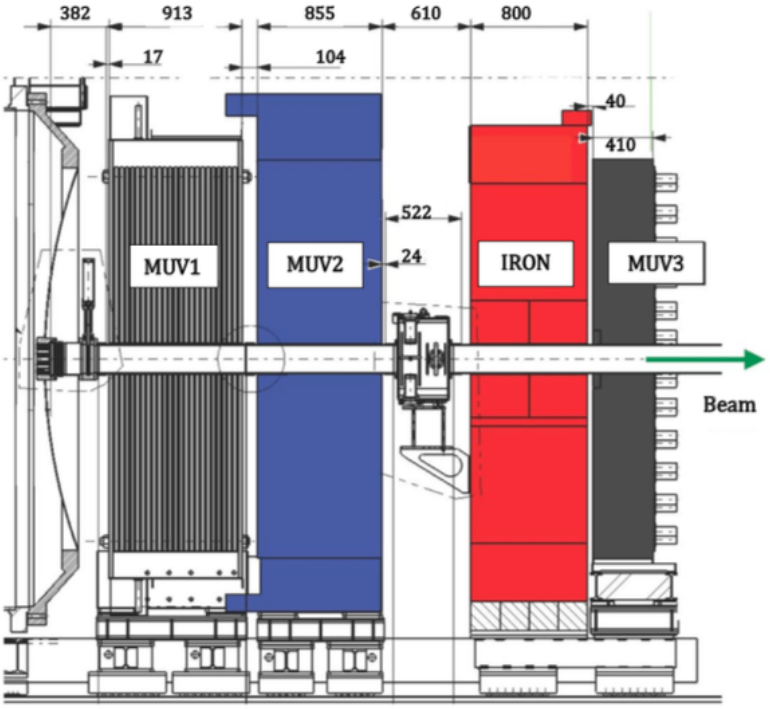

Figure 2.12: *Schematic view of the hadronic calorimeters (striped grey and blue). The iron wall (red) and the muon detector (grey) are also visible [54].*

The MUV3 The MUV3 detector is a muon detector, located downstream of the MUV1-2 system, behind an 80 cm thick iron wall, used to stop any surviving hadrons (Fig. 2.12), and it provides fast identification for muons traversing the whole calorimeter system (LKr, MUV1,2 and the iron wall), which has a total thickness of about 14 interaction lengths. The MUV3 is a square-faced detector with transverse size of 2.64×2.64 m^2. Like the NewCHOD, the MUV3 consists of plastic scintillator tiles, 8 of which have a smaller area and are placed around the beampipe, where the instantaneous beam rate is higher (Fig. 2.13). Two PMTs are placed directly behind each scintillator and are used to read out each tile.

The time resolution of the individual MUV3 channels is $\sigma_t = 600$ ps. The MUV3

muon identification efficiency exceeds 99.5% for momenta above 15 GeV/c. This makes the MUV3 suitable to provide particle identification for $N \to \pi\mu$ searches, where the majority of tracks have momenta above 30 GeV/c. In these decays, one of the two tracks leaves a signal in the muon detector, while the other one does not. This, together with the $\frac{E}{p}$ measured by the LKr and the Straw spectrometer, constitutes all the information used for particle identification for the work detailed in this thesis.

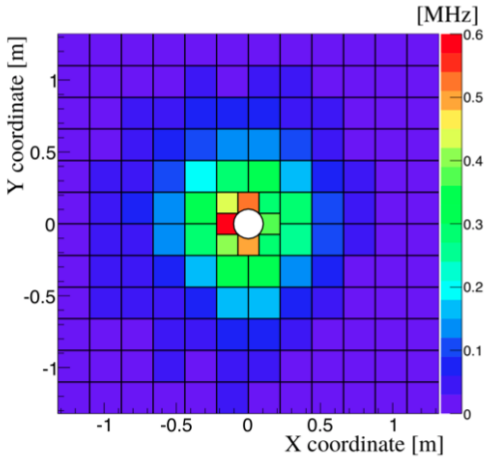

Figure 2.13: *The MUV3 tile rate in nominal beam conditions. A single inner "hot tile" is present due to the decay of beam pions to muons [54].*

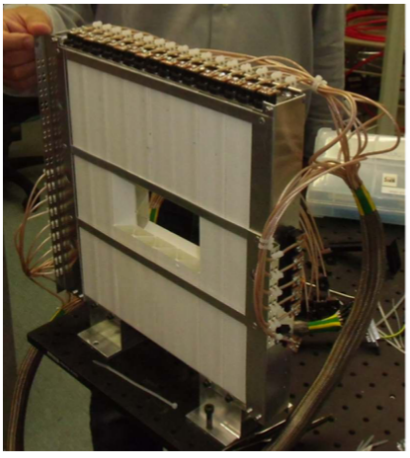

Figure 2.14: *A CHANTI station, with the hole for the passage of the beam particles [54].*

Other detectors

The CHANTI The Charged particle Anticounter (CHANTI) detector provides rejection for inelastic interactions of the beam with the most downstream GTK station, GTK3, with a 99% efficiency. The CHANTI is composed of six square scintillator hodoscope stations (Fig. 2.14), with a hole in the centre to allow for the beam particles to pass.

The single hit time resolution was measured at 1 ns.

The CHANTI detector is used as a veto for $N \to \pi\mu$ decay searches.

The MUV0 The MUV0 detector is a scintillator hodoscope designed to detect negative pions with momenta below 10 GeV/c, deflected towards positive X by the spectrometer magnet, MNP33, and leaving the lateral acceptance near the RICH.

The information provided by the MUV0 is not used for HNL decay searches.

The HASC The Hadronic Sampling Calorimeter (HASC) is located downstream of the MUV3 and is used for the detection of positive pions with momentum above

50 GeV/c and propagating through the beam holes in the centres of the Straw chambers.

The HASC is not used for the search detailed in this thesis.

2.5.3 Summary of detector purposes for Heavy Neutral Lepton decay searches

Several subsystems are exploited to detect the $N \to \pi\mu$ signal for the HNL decay searches described in this work.

The two-track, high-momentum final state that constitutes the signature of $N \to \pi\mu$ decays is detected by the downstream Straw spectrometer, whereas the time measurement of the two tracks is provided by the CHOD detector. Identification of pions and muons in the final state is performed by studying the energy-momentum ratio of the two tracks, combining the information provided by the Straw spectrometer with the one provided by the electromagnetic calorimeter, the LKr. The muon detector, the MUV3, is used to provide muon identification for one of the two final state tracks.

Several detectors are used as veto systems to reject background sources to the pion-muon final states.

The KTAG provides information on whether a kaon signal is found in coincidence with the downstream tracks. The photon veto systems (LAV, SAV and LKr) are exploited to reject any extra activity with final state photons emitted with an angle between 0 mrad and 50 mrad from the beamline, while extra upstream activity is vetoed by the CHANTI.

2.5.4 The trigger and data-acquisition system

The Trigger and Data Acquisition (TDAQ) system collects the data and records it to disk for further analysis. In this Section, an overview of the NA62 TDAQ is provided. Further information can be found in [60].

The trigger levels

The NA62 experiment adopts a multi-level trigger strategy to reduce the downstream particle flux, 10 MHz, to a rate limited by the available bandwidth for storing the data to disk, 100 kHz. A description of the trigger levels follows.

- **L0**: a hardware-based trigger, evaluating sub-detector digitised signals, the so-called "primitives", before passing the decision to the Level 0 Trigger Processor (L0TP). Each trigger primitive can then be used to build a trigger, to

select events with specific features based on the timing coincidence of multiple primitives. The maximum L0 trigger rate is 1 MHz. Six detectors contribute to the L0 trigger, which was in operation during the full 2016-2018 data-taking period;

- **L1**: a software trigger, requiring loose selection criteria for specific sub-detectors, based on the signal decay of interest. Each algorithm is applied sequentially, aiming to reduce the trigger rate to about 100 kHz. None of the calorimeters (LKr, MUV1, MUV2, IRC and SAC) or the GTK are read at L0, because of their amount of channels. The information they collect is read at L1, which performed during the full 2016-2018 data-taking.

The L0 primitives

Each sub-detector participating in the L0 trigger generates primitives, which are time-stamped data packets containing information on whether specific criteria were met according to the trigger firmware for each sub-detector. To build a L0 trigger, the L0TP identifies which primitives were simultaneously true within a 6.25 ns time window. If any of the primitive coincidences match with any of the user-requested triggers, the L0 trigger is issued and the event is passed to the L1 software stage. For the work presented in this thesis, two triggers are relevant:

- **Control**: CHOD, used for normalization purposes and for counting the number of POT;
- **Muon exotics**: RICH-Q2-M(O)1, used to collect $N \to \pi\mu$ events. During the 2016-2018 data taking, this mask was downscaled of different factors, from a minimum of 1 to a maximum of 20, due to the limited bandwidth for data acquisition. For example, a downscaling of 10 means that only one triggered event out of 10 has been written on disk. The data collected with this mask amounted to not more than 1% of the available L0 bandwidth throughout the data-taking period.

These are defined by the combination of different primitives:

- **CHOD**: primitives for any charged track, based on hit multiplicity;
- **RICH**: primitives for any charged track above Cherenkov threshold, based on hit multiplicity;
- **Q2**: primitives for two CHOD quadrants containing hits within a 10 ns time window;
- **M(O)1**: primitives for at least one (outer) MUV3 tile containing hits.

The L1 algorithms

After an event has passed the L0 stage, the L1 software trigger is run on the PC farm, a cluster of 32 computers. Three relevant algorithms are applied at the L1 stage, for the "muon exotics" trigger used for HNL decay searches, which reduce of a factor of about 20 the amount of data that pass through the L1 decision:

- **notKTAG**: rejects events with at least five out of eight KTAG sectors being in time with each others and within 5 ns of the L0 trigger time. This algorithm identifies a beam kaon candidate consistent with the event time and rejects it to reduce the background to $N \to \pi\mu$ signals;
- **notLAV**: used as a veto, the algorithm searches all twelve LAV stations for at least two hits. The time of the hit must be within 10 ns of the L0 trigger time. This suppresses any possible background involving final-state photons emitted at large angles;
- **StrawExo**: this algorithm performs a track reconstruction and searches for one negative track with a momentum between 3 GeV/c and 100 GeV/c.

2.5.5 The NA62 framework

The NA62 Framework (NA62FW) is a software framework developed for the NA62 experiment. The framework is comprised of three independent packages, all based on the ROOT software [61]:

- **NA62MC**: the NA62 Monte Carlo (MC) framework is a simulation based on the Geant4 (G4) package [62]. It is used to produce large simulated event samples of the individual kaon modes, together with several HSM and DF processes. A full Monte Carlo simulation of the HNL production from different D mesons and its subsequent decay to two-body final states has been designed, within the scope of this thesis, to study the NA62 expected sensitivity to $N \to \pi\mu$ decays. Within the MC simulation, the G4 package tracks the decay products through the full geometry of the detector. This includes the simulation of electromagnetic and hadronic interactions, multiple scattering and the effect of magnetic fields.
- **NA62Reconstruction**: the reconstruction package is modularised to reconstruct events and candidates from either raw data or MC simulations, for each sub-detector system. NA62Reconstruction is also used to create an online monitor for data acquisition, and is particularly useful during the run to spot systematic issues with any of the sub-detectors;

- **NA62Analysis**: the analysis package contains a series of libraries and tools to perform data analysis, reading events provided by the reconstruction software.

In this thesis, significant contributions to both the NA62MC and the NA62Analysis frameworks have been made. For the analysis described in the following Chapters, all three packages were extensively used. The full documentation about the NA62 framework can be found in [63].

Chapter 3

Full Monte Carlo simulation for Heavy Neutral Lepton production and decay

In this Chapter, the full MC simulation for HNL production and decay at NA62 is detailed, in the case of kaon-beam operation mode.

Protons from the SPS beam interact with either the Be target or the Cu-Fe TAXes to produce D mesons, which may decay to an HNL via the modes listed in Section 1.3.2. In the Fiducial Volume (FV), the HNL decays to two-body final states, which are propagated through the NA62 detector via the Geant4 software [62].

Several factors must be taken into account when computing the probability of generating HNL two-body decays with both decay products in the NA62 geometric acceptance:

- the probability of a D meson to be generated from proton interactions;
- the BRs of HNL production modes from D mesons;
- the probability for the HNL to reach the FV and decay in it;
- the BR of the chosen two-body HNL decay channel;
- the probability of the HNL decay products to be in the NA62 geometric acceptance.

For example, for $U^2 = 10^{-6}$, $m_N = 1$ GeV, $|p_N| = 10$ GeV/c and a ≈ 100 m long fiducial region, the probability for an HNL to reach the FV and decay in it is about 10^{-2}. For this reason, the probability of generating a signal event with final states in the NA62 geometric acceptance is boosted, in the MC simulation, by neglecting some of the probabilities listed above and by manually forcing some processes, so

that less time and computing power are needed to generate good signal events; this ensures that the efficiency of the MC simulation is much higher than otherwise. The boosting procedures used within the MC simulation are described in detail in the following and are corrected for at a further stage (the analysis).

The MC simulation detailed in this thesis is the first full one to simulate a DF production through multiple modes, its propagation up to the experimental FV and its decay to selected two-body final states at the NA62 experiment. No software was available that could already simulate the whole chain through the NA62 detector. Moreover, at the MC stage, the boosting techniques that neglect the probabilities listed above are necessary to ensure that the probability to generate a signal event with decay products in the NA62 geometric acceptance is several orders of magnitude higher than the one without the use of any boosting technique. These are the reasons why this full MC simulation has been coded by hand, without the use of external tools and libraries, except for the Pythia software [64], when producing the D meson momentum distributions from proton interactions, and the Geant4 package, [62] when tracking the HNL decay products through the NA62 apparatus.

The MC simulation is kept coupling-independent, to allow for studying different scenarios, according to the value of U^2 and the relative ratios of U_e^2, U_μ^2 and U_τ^2 that can be set at the analysis stage. This means that the following assumption is made at the MC stage:

$$U_e^2 : U_\mu^2 : U_\tau^2 = 1 : 1 : 1; \quad U^2 = 3. \tag{3.1}$$

Even though this U^2 value is unphysical, it can be used within the simulation because it is replaced by proper physical values (between 10^{-10} and 10^{-1}) during the analysis.

Within this simulation, the HNL can decay to several two-body, fully-reconstructible final states:

- $\pi^\pm e^\mp$,
- $\pi^\pm \mu^\mp$,
- $\rho^\pm e^\mp$,
- $\rho^\pm \mu^\mp$.

It must be noted that the ρ particle would decay within the NA62 fiducial volume, so that the last two listed modes would have effectively more than two particles in the final state.

Choosing a decay mode of a specific sign also produces the opposite-sign mode half of the times; for example, if the $\pi^\pm\mu^\mp$ mode is set, half of the final states are $\pi^+\mu^-$ and half are $\pi^-\mu^+$.

Moreover, the HNL mass is a parameter that can be changed within this simulation, so that HNLs of different masses can be generated and studied. All the distributions and results presented in this thesis have been produced on a sample of about $5 \cdot 10^6$ generated MC events, starting at a mass of 250 MeV/c^2 and ending at a mass of 1960 MeV/c^2.

3.1 D meson production

As the event simulation begins, the D meson species is chosen, according to the relative production yields provided within the NA62 collaboration via the Pythia software, used to simulate interactions between 400 GeV/c protons and Be target protons [65]:

- $D^+ = 0.140$,
- $D_S^+ = 0.042$,
- $D^- = 0.175$,
- $D_S^- = 0.050$,
- $D^0 = 0.264$,
- $\bar{D}^0 = 0.329$.

Both proton-proton (p-p) and proton-neutron (p-n) interactions occur when the proton beam interacts with the target. The difference between the resulting momentum distributions is negligible, so that kinematic distributions originated from p-p interactions can be used also in the p-n case. Moreover, these kinematic distributions are generated simulating hard interactions between partons. Therefore, the distributions do not change if the protons interact with different materials. The type of material is taken into account later, at the analysis stage, when the total p-X cross section (X being either Be or Cu, in this case) is computed. For this reason, the momenta distributions of the D mesons produced using Pythia can be used for both target and TAX interactions.

Additional D mesons can be produced in cascades generated by secondary interactions between the target or TAXes and the hadrons produced from proton-Be or proton-Cu interactions. This secondary production is dominant in the TAX case, due to Cu having a higher mass number compared to Be, but it was not accounted for in this full MC simulation, due to time constraints. This aspect is nonetheless worth further investigation and study.

In case the HNL is too massive to be produced in any decay of a certain D meson, that species cannot be sampled for that particular event generation.

The proton interacts with the target with a probability of $\epsilon_p = 1 - e^{-\frac{l}{\lambda_p}} = 0.61$, where $l = 40$ cm is the target length and λ_p is the proton nuclear interaction length (42.1 cm in the target case). The protons that do not interact with the target (39% of the total) have an interaction with the TAXes, with a probability of $\epsilon_p = 0.99999$ ($l = 323$ cm, $\lambda_p = 15.3$ cm for the TAX case).

The Z coordinate of the D meson production point, z_0, is computed, using the centre of the target as origin of the reference frame. The beam intercepts the target at $X = Y = 0$ mm, whereas it intercepts the TAXes at $X = 0$ mm and $Y = -22$ mm, because of two dipole magnets that divert the beam downwards and then steer it back horizontally. The Z coordinate of the D meson production point is:

$$z_0 = -\lambda_p \ln(1 - \epsilon_p R) + L, \tag{3.2}$$

where R is a random number uniformly generated in the [0,1) range and L ensures that z_0 is computed with respect to the origin of the reference frame, in the target centre ($L = -20$ cm for target production and $L = 23.07$ m in the TAX case).

The D meson production point is shown in Fig. 3.1 for target production and in Fig. 3.2 in the TAX production case. In this simulation, it is assumed that a beam proton interacting in the target/TAXes always produces a D meson. This is the first technique used to boost the the probability of generating a signal event with final states in the NA62 geometric acceptance, but needs to be corrected for at a later stage, to account for the D meson production cross-section in Be/Cu, together with the fact that several other processes can occur, when a proton interacts with the target/TAXes.

Then, the transverse and longitudinal momenta of the D meson, p_t and p_z, are generated, randomly extracted from the Pythia kinematic distributions provided within the collaboration; in what follows, the specific D meson species is denoted as D.

The D meson kinematics is worked out in the laboratory rest frame. The azimuthal angle, ϕ_D, is randomly, uniformly generated in the [0,2π) range. The polar angle is

$$\theta_D = \arctan\left(\frac{p_t}{p_z}\right) \tag{3.3}$$

and its distribution is shown in Fig. 3.3.

The modulus of the D meson three-momentum (Fig. 3.4) is computed as

$$|\vec{p}_D| = \sqrt{p_t^2 + p_z^2}, \tag{3.4}$$

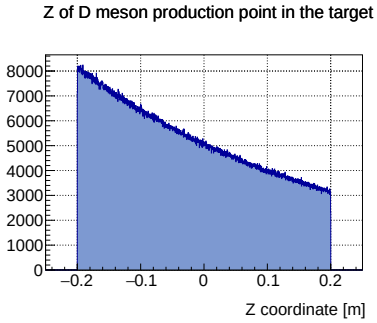

Figure 3.1: *D meson production point, for all D meson species produced in the target, for $m_N = 1\ GeV/c^2$, $U^2 = 3$ and $U_e^2 : U_\mu^2 : U_\tau^2 = 1:1:1$.*

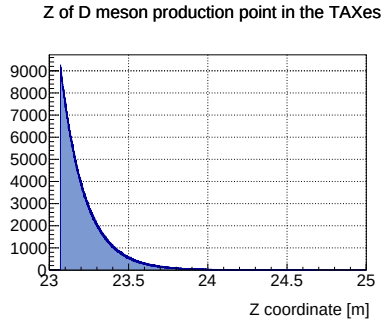

Figure 3.2: *D meson production point, for all D meson species produced in the TAXes, for $m_N = 1\ GeV/c^2$, $U^2 = 3$ and $U_e^2 : U_\mu^2 : U_\tau^2 = 1:1:1$.*

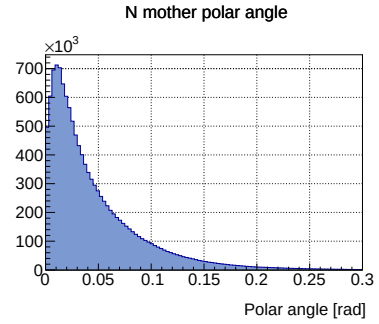

Figure 3.3: *Polar angle of the D meson at production, in the laboratory frame, for all D meson species, for $m_N = 1\ GeV/c^2$, $U^2 = 3$ and $U_e^2 : U_\mu^2 : U_\tau^2 = 1:1:1$.*

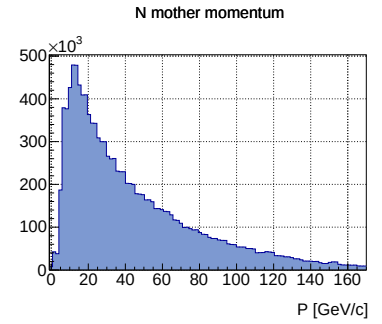

Figure 3.4: *Momentum of the D meson at production, in the laboratory frame, for all D meson species, for $m_N = 1\ GeV/c^2$, $U^2 = 3$ and $U_e^2 : U_\mu^2 : U_\tau^2 = 1:1:1$.*

and its X and Y components are

$$|\vec{p}_D^{\,x}| = |\vec{p}_D| \sin\theta_D \cos\phi_D \tag{3.5}$$

and

$$|\vec{p}_D^{\,y}| = |\vec{p}_D| \sin\theta_D \sin\phi_D. \tag{3.6}$$

It must be taken into account that the 400 GeV/c proton beam, which is narrowly focused when impinging on the T10 target (and it is therefore called "pencil" beam), is more spread at the TAX impact plane, as it is shown in Fig. 3.5. Moreover, the momenta of the protons are not parallel to the Z axis, as it can be seen in Fig. 3.6 and Fig. 3.7, where the angles the proton momenta form with the X and Y axes are plotted versus the X and Y spread, respectively.

As a result, when the D meson is produced in the TAXes, its production point

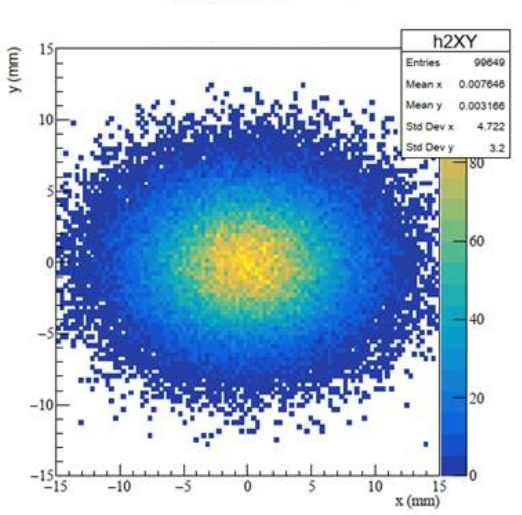

Figure 3.5: *$X-Y$ spread of the beam protons at the TAX impact plane. The Y coordinate of the impact point has been shifted from -22 mm to 0 mm in this distribution. This plot has been provided by the beam experts within the collaboration.*

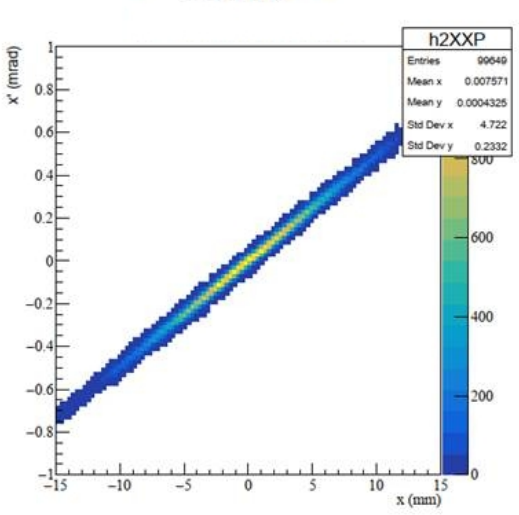

Figure 3.6: *X component of the proton direction with respect to the Z axis as a function of the X coordinate at the TAX impact plane. This plot has been provided by the beam experts within the collaboration.*

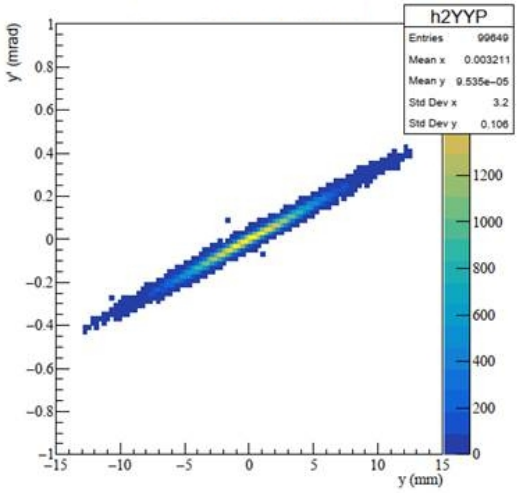

Figure 3.7: *Y component of the proton direction with respect to the Z axis as a function of the Y coordinate at the TAX impact plane. The Y coordinate of the impact point has been shifted from -22 mm to 0 mm in this distribution. The slope is different from the one shown in Fig. 3.6 due to the presence of quadrupoles along the beamline. This plot has been provided by the beam experts within the collaboration.*

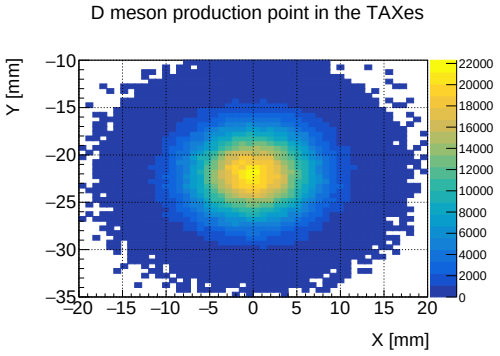

Figure 3.8: *$X-Y$ spread of the D meson production point at the TAXes, broadly distributed because of the non-pencil shape of the proton beam at the TAX plane.*

does not have $X, Y = (0, -22)$ mm coordinates, but its X, Y production coordinates (called x_0 and y_0) are randomly extracted from two Gaussian distributions, the first one with mean $\mu = 0$ mm and standard deviation $\sigma = 4.7$ mm, and the second one with $\mu = -22$ mm and $\sigma = 3.2$ mm.

The D meson momentum, with its components (p_t and p_z) extracted from Pythia, must be rotated to take into account the parent-proton non-zero components in X and Y: according to the distributions shown in Fig. 3.6 and Fig. 3.7, the X and Y components of the proton direction with respect to the Z axis are

$$\frac{dx}{dz} = 0.05 \cdot 10^{-3} mm^{-1} \cdot x_0, \tag{3.7}$$

$$\frac{dy}{dz} = 0.03 \cdot 10^{-3} mm^{-1} \cdot y_0 - 0.03 \cdot 10^{-3}, \tag{3.8}$$

where the slopes in X and Y are different due to the presence of quadrupoles along the beamline.

Therefore, the rotation angles around the Y and X axis, respectively, are:

$$\theta_D^x = \arctan\left(\frac{dx}{dz}\right), \tag{3.9}$$

and

$$\theta_D^y = \arctan\left(\frac{dy}{dz}\right). \tag{3.10}$$

The rotated D meson momentum is:

$$p'_D = B \cdot A \cdot p_D, \tag{3.11}$$

where p_D is the momentum to be rotated, and B and A are rotation matrices around the Y and X axis, respectively:

$$B = \begin{bmatrix} \cos\theta_D^x & 0 & \sin\theta_D^x \\ 0 & 1 & 0 \\ -\sin\theta_D^x & 0 & \cos\theta_D^x \end{bmatrix} \tag{3.12}$$

and

$$A = \begin{bmatrix} 1 & 0 & 0 \\ 0 & \cos\theta_D^y & -\sin\theta_D^y \\ 0 & \sin\theta_D^y & \cos\theta_D^y \end{bmatrix}. \tag{3.13}$$

After performing the rotation, the new rotated angles are computed:

$$\theta'_D = \arctan\left(\frac{\sqrt{(p'^x_D)^2 + (p'^y_D)^2}}{p'^z_D}\right) \tag{3.14}$$

and

$$\phi'_D = \arctan\left(\frac{p'^y_D}{p'^x_D}\right). \tag{3.15}$$

From now on, for simplicity, all the D meson quantities after the rotation drop the prime notation: $p'_D \to p_D$, $p'^{x,y,z}_D \to p^{x,y,z}_D$, $\theta'_D \to \theta_D$, $\phi'_D \to \phi_D$, while x_0, y_0 and z_0 are still the coordinates of the D meson production point (in both target and TAX cases) in the reference frame where the origin is placed in the centre of the T10 target.

3.2 D meson propagation and decay

All production BRs listed in Section 1.3.1 are computed, and the HNL production mode is randomly chosen accordingly. One should keep in mind that, even though all formulae detailed in Appendix B include the coupling, in this simulation it is assumed that $U_l^2 = 1$ and, therefore, $U^2 = 3$, to keep the whole procedure coupling-independent; the coupling is properly considered only at the analysis stage.

It also needs to be noted that, for HNL production from $D, D_S \to \tau\nu_\tau$; $\tau \to NX$, only $BR(\tau \to NX)$ is considered. As an arbitrary choice, the MC simulation does not account for the fact that HNL production modes from τ leptons are sub-dominant with respect to direct production modes from D mesons, since they are scaled by an extra factor, the BR of τ lepton production from D, D_S meson decays. This extra factor is accounted for at the analysis stage.

The D meson mean path length and the modulus of the β velocity are computed:

$$\lambda_D = \frac{c|\vec{p}_D|\tau_D}{m_D} \tag{3.16}$$

and

$$|\vec{\beta}_D| = \frac{|\vec{p}_D|}{\sqrt{m_D^2 + |\vec{p}_D|^2}}, \tag{3.17}$$

where c is the speed of light, τ_D is the D meson lifetime and m_D is the D meson mass.

The distance between the D meson production point and its decay point is then computed:

$$|\vec{r}^{\,decay}_D| = -\lambda_D \ln(1 - R), \tag{3.18}$$

where R is a random number uniformly generated in the [0, 1) range.

The coordinates of the D meson decay point, with respect to the origin of the

system, chosen to be in the centre of the target, are:

$$(x, y, z)_D^{decay} = (x_0 + |\vec{r}_D^{decay}| \sin(\theta_D) \cos(\phi_D), y_0 + |\vec{r}_D^{decay}| \sin(\theta_D) \sin(\phi_D), \\ z_0 + |\vec{r}_D^{decay}| \cos(\theta_D)). \tag{3.19}$$

The distribution of the Z coordinate of the D meson decay point is plotted in Fig. 3.9 for D produced in the target and in Fig. 3.10 for D generated in the TAXes.

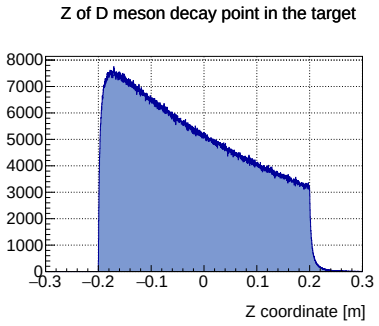

Figure 3.9: *D meson decay point, for all D meson species produced in the target, for U^2 =3 and $U_e^2 : U_\mu^2 : U_\tau^2$ =1:1:1. The tail above 0.2 m is due to D mesons produced right before the end of the target.*

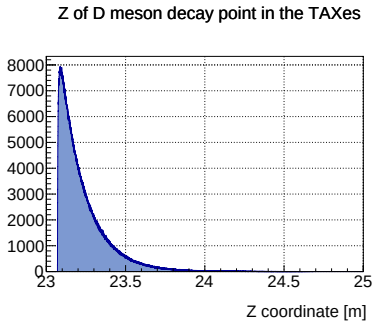

Figure 3.10: *D meson decay point, for all D meson species produced in the TAXes, for U^2 =3 and $U_e^2 : U_\mu^2 : U_\tau^2$ =1:1:1.*

The D meson decay point is also the HNL production point, for all production modes in which the HNL is directly generated through D decays. Otherwise, the D decay point is the τ lepton production point.

In the latter case, the τ lepton kinematics is worked out. The cosine of the polar angle in the D meson rest frame, $\cos\theta_\tau$, is randomly, uniformly generated in the [0,1) range, since the D is a pseudo-scalar meson and, therefore, the angular distribution of two-body decay products is isotropic. The azimuthal angle, ϕ_τ, is randomly, uniformly extracted in the [0, 2π) range. The modulus of the τ lepton three-momentum in the D meson rest frame is defined as:

$$|\vec{p}_\tau| = \frac{\sqrt{m_D^4 + m_\nu^4 + m_\tau^4 - 2m_D^2 m_\nu^2 - 2m_D^2 m_\tau^2 - 2m_\nu^2 m_\tau^2}}{2m_D}, \tag{3.20}$$

where the SM neutrino mass, m_ν, can be neglected and m_τ is the τ lepton mass.

The components of the three-momentum along the axes are then computed in the D meson rest frame, together with the energy:

$$p_\tau^x = |\vec{p}_\tau| \sin(\theta_\tau) \cos(\phi_\tau), \tag{3.21}$$

$$p_\tau^y = |\vec{p}_\tau| \sin(\theta_\tau) \sin(\phi_\tau), \tag{3.22}$$

$$p_\tau^z = |\vec{p}_\tau| \cos(\theta_\tau), \tag{3.23}$$

$$E_\tau = \sqrt{|\vec{p}_\tau|^2 + m_\tau^2}. \tag{3.24}$$

The τ lepton is then boosted into the laboratory frame: the β velocity of the D meson is calculated and used to compute the τ lepton three-momentum components and energy in the new reference frame:

$$\vec{\beta}^D = (|\vec{\beta}^D| \sin(\theta_D) \cos(\phi_D), |\vec{\beta}^D| \sin(\theta_D) \sin(\phi_D), |\vec{\beta}^D| \cos(\theta_D)), \tag{3.25}$$

$$E' = \gamma_D(-\beta_x^D p_x - \beta_y^D p_y - \beta_z^D p_z + E), \tag{3.26}$$

$$p'_x = \gamma_D(-\beta_x^D E + \beta_y^D p_y + \beta_z^D p_z + p_x), \tag{3.27}$$

$$p'_y = \gamma_D(-\beta_y^D E + \beta_x^D p_x + \beta_z^D p_z + p_y), \tag{3.28}$$

$$p'_z = \gamma_D(-\beta_z^D E + \beta_x^D p_x + \beta_y^D p_y + p_z), \tag{3.29}$$

where $\gamma_D = \frac{\sqrt{|\vec{p}_D|^2 + m_D^2}}{m_D}$ is the D meson Lorentz factor in the laboratory frame, p_x, p_y, p_z and E are the τ lepton kinematic components before the boost, and p'_x, p'_y, p'_z and E' are its components after the boost.

The τ lepton is let decay in the laboratory rest frame. The mean path length and the modulus of the β velocity are

$$\lambda_\tau = \frac{c|\vec{p}_\tau|\tau_\tau}{m_\tau} \tag{3.30}$$

and

$$|\vec{\beta}_\tau| = \frac{|\vec{p}_\tau|}{\sqrt{m_\tau^2 + |\vec{p}_\tau|^2}}, \tag{3.31}$$

where τ_τ is the τ lepton lifetime and $|\vec{p}_\tau|$ is the modulus of the τ lepton three-momentum.

The probability for the τ lepton to decay before the TAXes (in the target production case) or the beginning of the FV (in case of TAX production) is assumed to be 1, and it is used to calculate the distance between the τ lepton production point and its decay point:

$$|\vec{r}_\tau^{decay}| = -\lambda_\tau \ln(1 - \epsilon_\tau^{decay} R), \tag{3.32}$$

where $\epsilon_\tau^{decay} = 1$.

The coordinates of the τ lepton decay point, with respect to the origin of the system, are:

$$x_\tau^{decay} = x_D^{decay} + |\vec{r}_\tau^{decay}| \sin(\theta_\tau) \cos(\phi_\tau); \tag{3.33}$$

$$y_\tau^{decay} = y_D^{decay} + |\vec{r}_\tau^{decay}| \sin(\theta_\tau) \sin(\phi_\tau); \tag{3.34}$$

$$z_\tau^{decay} = z_D^{decay} + |\vec{r}_\tau^{decay}| \cos(\theta_\tau). \tag{3.35}$$

3.3 Heavy Neutral Lepton production

At this point, the HNL is produced, either directly from the D meson or from the τ lepton. One further distinction must be made: if the HNL is produced through two-body decays, the kinematics can be worked out straightforwardly. In the case of production via three-body decays, the so-called "hit-and-miss" procedure must be performed, as described in the following.

The ROOT *TGenPhaseSpace* class is used to randomly extract two invariant masses in the mother particle rest frame (where the mother is either a D meson or a τ lepton), within the boundaries of the Dalitz plot of the chosen production mode. The two variables are m^2_{Hl} and m^2_{Nl}, the squared invariant masses of the Hl and Nl pairs, respectively.

Then, two other variables are defined, that are needed for the formulae detailed in Appendix A:

$$q^2 = m^2_{Nl} \tag{3.36}$$

and

$$E_N = \frac{m_m^2 - m^2_{Hl} + m^2_N}{2m_m}, \tag{3.37}$$

where E_N is the HNL energy in the mother rest frame, m_m is the mother mass and m_N is the HNL mass.

The chosen production-mode function detailed in Appendix A, $f(q^2, E_N)$, is then computed for the generated values of q^2 and E_N. A random number R is then uniformly extracted in the $[0, 1)$ range. The procedure starting with the call to *TGenPhaseSpace* is performed as many times as needed for this condition to be satisfied:

$$R \leq \frac{f(q^2, E_N)}{f_{max}}, \tag{3.38}$$

where f_{max} is computed with the software Minuit and is the maximum value the function can take within the absolute maximum and minimum values of E_N and q^2, defined as:

$$E_N^{min} = \frac{(m_m^2 - m^{2\,max}_{Hl} + m^2_N)}{2m_m}, \tag{3.39}$$

$$E_N^{max} = \frac{(m_m^2 - m^{2\,min}_{Hl} + m^2_N)}{2m_m} \tag{3.40}$$

and

$$q^2_{min} = (m_N + m_l)^2, \tag{3.41}$$

$$q^2_{max} = (m_m - m_H)^2. \tag{3.42}$$

Here, $m^{2\,max}_{Hl} = (m_m - m_N)^2$ is the maximum squared invariant mass of the Hl pair, corresponding to the case where H and l are produced back to back and N is generated at rest (in the mother rest frame); $m^{2\,min}_{Hl} = (m_H + m_l)^2$ is the minimum invariant mass of the Hl pair, corresponding to the case where Hl is produced back to back with respect to N (in the mother rest frame).

At this point of the MC simulation, the HNL kinematics can be worked out, in the mother rest frame, for both two- and three-body production modes.

The azimuthal angle, ϕ_N, is randomly, uniformly extracted in the [0,2π) range. The cosine of the polar angle, $\cos\theta_N$, is randomly, uniformly generated in the [0,1) range. This assumption is correct if the HNL is produced through two-body D decays, since the D is a pseudo-scalar meson and, therefore, the angular distribution of its two decay products is isotropic. In case the HNL is generated in three-body D meson decays or from τ leptons (which have non-zero spin), this is not correct; this dependence has been neglected in this work, due to time constraints, but it would need to be included in case this simulation were to be further developed, since it is supposed to lower the expected sensitivity.

The distribution of the HNL polar angle in the laboratory frame is shown in Fig. 3.11.

In case of two-body production, both from D mesons and τ leptons, the modulus of the HNL three-momentum in the mother rest frame is defined as:

$$|\vec{p}_N| = \frac{\sqrt{m_m^4 + m_N^4 + m_V^4 - 2m_m^2 m_N^2 - 2m_m^2 m_V^2 - 2m_N^2 m_V^2}}{2m_m}, \tag{3.43}$$

where V denotes both leptons and mesons the HNL is produced in pair with.

In case of three-body production, both from D mesons and τ leptons, the modulus of the HNL three-momentum in the mother rest frame is worked out from:

$$|\vec{p}_N| = \sqrt{E_N^2 - m_N^2}. \tag{3.44}$$

At this point, the components of the three-momentum along the axes are computed:

$$p_N^x = |\vec{p}_N| \sin(\theta_N)\cos(\phi_N), \tag{3.45}$$

$$p_N^y = |\vec{p}_N| \sin(\theta_N)\sin(\phi_N), \tag{3.46}$$

$$p_N^z = |\vec{p}_N| \cos(\theta_N). \tag{3.47}$$

Then, the procedure from this moment on is unified, both for two- and three-body decays, and for production from D mesons and τ leptons. The HNL is boosted

into the laboratory frame: the β velocity of the mother particle is calculated and used to compute the three-momentum components and the energy of the HNL in the new reference frame:

$$\vec{\beta}^m = (|\vec{\beta}^m|\sin(\theta_m)\cos(\phi_m), |\vec{\beta}^m|\sin(\theta_m)\sin(\phi_m), |\vec{\beta}^m|\cos(\theta_m)). \tag{3.48}$$

The energy and momentum components after the boost are:

$$E' = \gamma_m(-\beta_x^m p_x - \beta_y^m p_y - \beta_z^m p_z + E), \tag{3.49}$$

$$p'_x = \gamma_m(-\beta_x^m E + \beta_y^m p_y + \beta_z^m p_z + p_x), \tag{3.50}$$

$$p'_y = \gamma_m(-\beta_y^m E + \beta_x^m p_x + \beta_z^m p_z + p_y), \tag{3.51}$$

$$p'_z = \gamma_m(-\beta_z^m E + \beta_x^m p_x + \beta_y^m p_y + p_z), \tag{3.52}$$

where $\gamma_m = \frac{\sqrt{|\vec{p}_m|^2 + m_m^2}}{m_m}$ is the mother-particle Lorentz factor in the laboratory frame, p_x, p_y, p_z and E are the HNL kinematic components before the boost, and p'_x, p'_y, p'_z and E' are its components after the boost.

The modulus of the HNL three-momentum, in the laboratory frame, is plotted in Fig. 3.12.

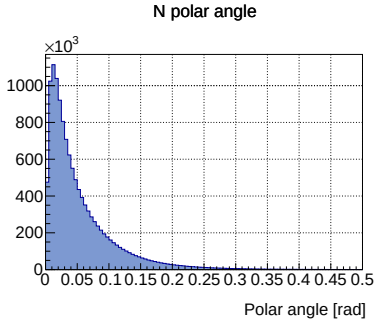

Figure 3.11: *Polar angle of the HNL at production, in the laboratory frame, for $m_N = 1$ GeV/c^2, $U^2 = 3$ and $U_e^2 : U_\mu^2 : U_\tau^2 = 1:1:1$.*

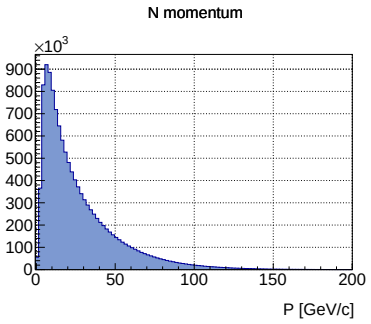

Figure 3.12: *Momentum modulus of the HNL at production, in the laboratory frame, for $m_N = 1$ GeV/c^2, $U^2 = 3$ and $U_e^2 : U_\mu^2 : U_\tau^2 = 1:1:1$.*

3.4 Heavy Neutral Lepton decay

At this point, to further boost the probability of generating a signal event with final states in the NA62 geometric acceptance, and to keep the simulation coupling-independent, the HNL lifetime is ignored and the HNL is manually propagated up to the beginning of the FV, and forced to decay within it, according to a flat Z

distribution. The HNL decay point in the lab frame is

$$\vec{r}_N^{decay} = R(\vec{r}_M - \vec{r}_m) + \vec{r}_m, \tag{3.53}$$

where R is randomly and uniformly generated in the [0,1) range, and $\vec{r}_m$ and $\vec{r}_M$ are, respectively, the positions of the HNL at $z_m^{FV} = 102.4$ m and $z_M^{FV} = 180.0$ m (the Z coordinates of the FV boundaries). Their components are defined as:

$$r_{m,M}^x = x_m^{decay} + \frac{p_N^x}{p_N^z}(z_{m,M}^{FV} - z_m^{decay}), \tag{3.54}$$

$$r_{m,M}^y = y_m^{decay} + \frac{p_N^y}{p_N^z}(z_{m,M}^{FV} - z_m^{decay}), \tag{3.55}$$

$$r_{m,M}^z = z_{m,M}^{FV}, \tag{3.56}$$

where x_m^{decay}, y_m^{decay} and z_m^{decay} are, respectively, the X, Y and Z coordinates of the HNL production point (which is also the D meson decay point). The Z coordinate of the HNL decay point is shown in Fig. 3.13.

After forcing the HNL to decay in the FV, its two charged decay products are generated. In the following, $\pi\mu$ final states are considered. Their kinematics are computed in the HNL rest frame. The azimuthal angles, $\phi_{\pi,\mu}$, are randomly, uniformly generated in the [0,2π) range and the cosines of the polar angles, $\cos\theta_{\pi,\mu}$, are randomly, uniformly extracted in the [0,1) range.

Even though the HNL does not have an isotropic angular decay distribution, since its spin is $s_N = \frac{1}{2}$, this dependence is here neglected and an isotropic angular distribution is considered for its decay products, due to time constraints. However, this aspect deserves further investigation, as including it is supposed to lower the expected sensitivity.

The kinematics of the decay products are then computed in the HNL rest frame:

$$|\vec{p}_{\pi,\mu}| = \frac{\sqrt{m_N^4 + m_\pi^4 + m_\mu^4 - 2m_N^2 m_\pi^2 - 2m_N^2 m_\mu^2 - 2m_\pi^2 m_\mu^2}}{2m_N}, \tag{3.57}$$

where m_π is the pion mass and m_μ is the muon mass. Then,

$$p_{\pi,\mu}^x = |\vec{p}_{\pi,\mu}| \sin(\theta_{\pi,\mu}) \cos(\phi_{\pi,\mu}), \tag{3.58}$$

$$p_{\pi,\mu}^y = |\vec{p}_{\pi,\mu}| \sin(\theta_{\pi,\mu}) \sin(\phi_{\pi,\mu}), \tag{3.59}$$

$$p_{\pi,\mu}^z = |\vec{p}_{\pi,\mu}| \cos(\theta_{\pi,\mu}), \tag{3.60}$$

$$E_{\pi,\mu} = \sqrt{|\vec{p}_{\pi,\mu}|^2 + m_{\pi,\mu}^2}. \tag{3.61}$$

Moreover,

$$\vec{p}_{\mu,\pi} = -\vec{p}_{\pi,\mu} \tag{3.62}$$

and

$$E_{\mu,\pi} = \sqrt{|\vec{p}_{\mu,\pi}|^2 + m^2_{\mu,\pi}}. \tag{3.63}$$

Then, each decay product is boosted in the laboratory frame. The HNL β velocity is calculated:

$$\vec{\beta}^N = (|\vec{\beta}^N| \sin(\theta_N)\cos(\phi_N), |\vec{\beta}^N| \sin(\theta_N)\sin(\phi_N), |\vec{\beta}^N| \cos(\theta_N)). \tag{3.64}$$

The energy and momentum components of each HNL decay product after the boost are:

$$E' = \gamma_N(-\beta^N_x p_x - \beta^N_y p_y - \beta^N_z p_z + E), \tag{3.65}$$

$$p'_x = \gamma_N(-\beta^N_x E + \beta^N_y p_y + \beta^N_z p_z + p_x), \tag{3.66}$$

$$p'_y = \gamma_N(-\beta^N_y E + \beta^N_x p_x + \beta^N_z p_z + p_y), \tag{3.67}$$

$$p'_z = \gamma_N(-\beta^N_z E + \beta^N_x p_x + \beta^N_y p_y + p_z), \tag{3.68}$$

where $\gamma_N = \frac{E_N}{m_N}$ is the HNL Lorentz factor in the laboratory frame, p_x, p_y, p_z and E are the decay-product kinematic components before the boost, and p'_x, p'_y, p'_z and E' are its components after the boost.

In Fig. 3.14 and Fig. 3.15, the distributions of the pion and muon three-momentum moduli are shown, only for the final states in the NA62 geometric acceptance (as described in the next paragraph).

3.5 Acceptance for Heavy Neutral Lepton decay products

The probability of producing a signal event with final decay products in the NA62 geometric acceptance is further boosted by manually propagating both HNL decay products up to the CHOD plane ($z_{CHOD} = 239.009$ m), to check whether they are in the CHOD geometric acceptance. If not, the event will not pass the analysis selection, so a procedure is designed to treat these cases.

The minimum and maximum radii of the CHOD used for the check are different from the ones used in the standard NA62 tool for computing detector geometric acceptances. This is due to the fact that the MNP33 magnet kick is approximated to a constant in the MC simulation, while the bluetube field and the multiple scat-

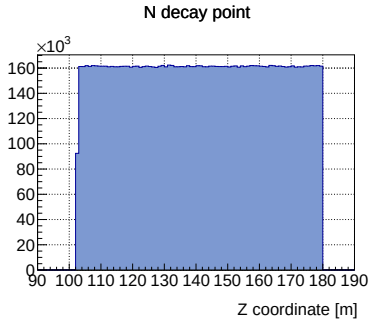

Figure 3.13: *Z coordinate of the HNL decay point, generated from a flat distribution, for $m_N = 1$ GeV/c^2, U^2 =3 and $U_e^2 : U_\mu^2 : U_\tau^2$ =1:1:1.*

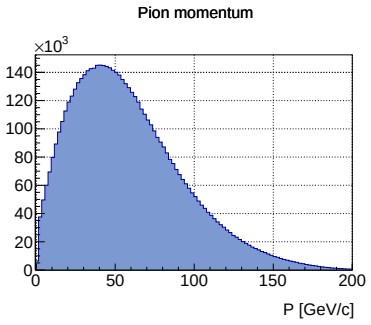

Figure 3.14: *Pion momentum, in the laboratory frame, for final states in the NA62 geometric acceptance, for $m_N = 1$ GeV/c^2, U^2 =3 and $U_e^2 : U_\mu^2 : U_\tau^2$ =1:1:1.*

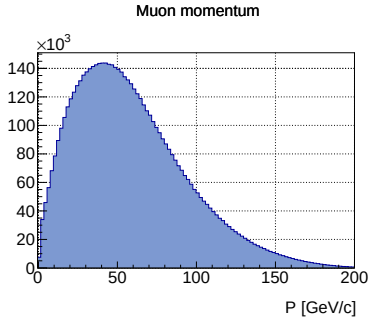

Figure 3.15: *Muon momentum, in the laboratory frame, for final states in the NA62 geometric acceptance, for $m_N = 1$ GeV/c^2, U^2 =3 and $U_e^2 : U_\mu^2 : U_\tau^2$ =1:1:1.*

tering of the decay products in the detectors are not taken into account at all. To compensate for these approximations, the CHOD geometric acceptance is bigger: $r_{min}^{CHOD} = 0$ cm and $r_{max}^{CHOD} = 130$ cm, whereas the standard values are $r_{min}^{CHOD} = 13$ cm and $r_{max}^{CHOD} = 110$ cm [54].

To check for the decay products to be in the CHOD geometric acceptance, the Straw spectrometer magnet (MNP33) kick must be included.

First of all, the decay products are propagated to the MNP33 plane ($z_{MNP33} = 196.345$ m). The components of the path they travel between the HNL decay point and the MNP33 plane are:

$$r_{[\pi,\mu],x}^{MNP33} = r_{N,x}^{decay} + \frac{p_{[\pi,\mu],x}}{p_{[\pi,\mu],z}}(z_{MNP33} - r_{N,z}^{decay}), \tag{3.69}$$

$$r_{[\pi,\mu],y}^{MNP33} = r_{N,y}^{decay} + \frac{p_{[\pi,\mu],y}}{p_{[\pi,\mu],z}}(z_{MNP33} - r_{N,z}^{decay}), \tag{3.70}$$

$$r^{MNP33}_{[\pi,\mu],z} = z_{MNP33}. \tag{3.71}$$

Then, the magnet kick is included: $p_{kick} = -270.0$ MeV/c for positively charged particles ($q = 1$). The decay products are propagated to the CHOD plane. The components of the path they travel between the MNP33 plane and the CHOD plane are:

$$r^{CHOD}_{[\pi,\mu],x} = r^{MNP33}_{[\pi,\mu],x} + q_{\pi,\mu}\frac{p_{kick}}{|\vec{p}_{\pi,\mu}|}(z_{CHOD} - r^{MNP33}_{[\pi,\mu],z}) + \frac{p_{[\pi,\mu],x}}{p_{[\pi,\mu],z}}(z_{CHOD} - r^{MNP33}_{[\pi,\mu],z}), \tag{3.72}$$

$$r^{CHOD}_{[\pi,\mu],y} = r^{MNP33}_{[\pi,\mu],y} + \frac{p_{[\pi,\mu],y}}{p_{[\pi,\mu],z}}(z_{CHOD} - r^{MNP33}_{[\pi,\mu],z}), \tag{3.73}$$

$$r^{CHOD}_{[\pi,\mu],z} = z_{CHOD}, \tag{3.74}$$

where $q_{\pi,\mu}$ is the electric charge of the considered decay product and $|\vec{p}_{\pi,\mu}|$ is its three-momentum modulus.

Then, the distance from the Z axis at the CHOD plane is calculated for both decay products:

$$\rho^{CHOD}_{\pi,\mu} = \sqrt{(r^{CHOD}_{[\pi,\mu],x})^2 + (r^{CHOD}_{[\pi,\mu],y})^2}. \tag{3.75}$$

If either distance is greater than r^{CHOD}_{max}, a regeneration process happens, in order to boost the probability of generating a signal event with final states in the NA62 geometric acceptance. Every quantity is recomputed, starting from the D meson species, as described from Section 3.1 onwards. The regeneration loop occurs as many times as needed to have both HNL decay products in the CHOD geometric acceptance (about 1000 times for $m_N = 1$ GeV/c^2), which are then passed to the Geant4 package to be tracked through the NA62 detector with high precision, including several effects that have been neglected or approximated at the manual propagation stage, namely the MNP33 magnetic field map, the bluetube field and the multiple scattering effects. If these effects were to be included in the manual propagation, their contribution would account for about 1% on the final acceptance. This has been studied by comparing the difference in the number of accepted events in case of manual or Geant4 propagation. Since this difference was found to be negligible, the choice of manually propagating the HNL decay products to check their acceptance at the CHOD plane, before passing the event to G4, has been considered preferable for the purposes of this simulation, as it allows optimising the overall computing time by orders of magnitude.

To summarise, the regeneration procedure has been introduced to boost the probability of generating an in-acceptance signal event, while keeping the computing time of the event generation as low as possible, and considering that the approximations that are included in the procedure only account for about 1% on the final signal

acceptance.

Each time the HNL is regenerated from scratch, it is stored as an entry of the output file produced by the MC simulation. This is needed at the analysis stage, to take into account all HNLs, also the ones that were discarded.

3.6 Monte Carlo simulation summary

A brief summary of the procedure detailed so far is given in the following.

To simulate the HNL production and decay to two-body final states that can be fully reconstructed, the D meson species is generated either in the Be target or in the Cu TAXes.

The HNL production mode is then chosen: if the D meson decays to an HNL, the HNL production point is computed; otherwise, the τ lepton is produced and let decay to an HNL.

Then, in both cases, the HNL kinematics are computed (either straightforwardly, in case of two-body production modes, or through the hit-and-miss procedure, when three-body production modes occur) and the HNL is boosted in the laboratory frame.

The HNL is then manually propagated to the beginning of the FV volume and forced to decay in it according to a flat distribution in Z, to keep the simulation lifetime- (and thus coupling-) independent.

At this point, the HNL decays to two-body final states, and its decay products are manually propagated to the CHOD plane, to check whether they are both in its geometric acceptance. If not, a regeneration procedure occurs, recomputing the whole simulation from scratch, until both decay products are in the CHOD geometric acceptance. During this regeneration procedure, every quantity is extracted again, starting from the D meson species onwards.

When the two HNL decay products are within the CHOD acceptance, they are then passed to Geant4 to be tracked, and the generation of the following MC event starts.

To summarise, each MC event contains:

- all the simulated HNLs (the many that have their decay products outside the CHOD acceptance and the one whose decay products are within the CHOD acceptance); each HNL is stored with its production and decay points, initial and final momenta and energies;
- two HNL decay products, both in the CHOD acceptance, stored and tracked by Geant4 and associated with their HNL parent.

3.7 Reconstruction of Monte Carlo events

Before being analysed, the MC events are reconstructed using the *NA62Reconstruction* framework.

The standard Straw spectrometer reconstruction only considers tracks with momentum between 5 GeV/c and 90 GeV/c and at an angle from the Z axis smaller than 0.02 mrad.

Since a non-negligible number of final-state pions and muons, generated with the MC simulation described in this Chapter, are high-momentum particles (as seen in Fig. 3.14 and Fig. 3.15), a customised spectrometer reconstruction is used. The momentum range has been extended between 5 GeV/c and 400 GeV/c, and the emission angle has been enlarged up to 0.05 rad, which is the maximum opening angle for tracks to be in the acceptance of all four Spectrometer chambers: $\frac{R_4}{D_{1-4}} = 0.05$, where $R_4 \approx 1$ m is the fourth chamber radius and $D_{1-4} \approx 20$ m is the distance between the first and the fourth chamber.

As can be seen in Fig. 3.16 and Fig. 3.17, the customised spectrometer reconstruction allows to reconstruct 15% more two-track MC HNL decays than the standard one. For this reason, the 5 million MC event sample that has been used to produce the results presented in this thesis has been reconstructed with this configuration.

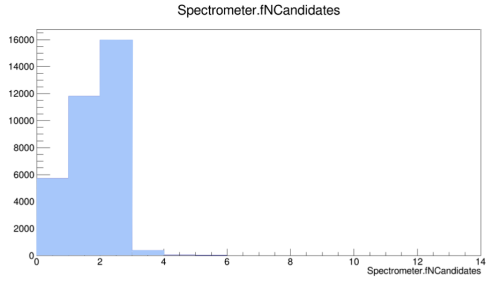

Figure 3.16: *Number of reconstructed tracks per event, for a MC sample reconstructed with the standard configuration (5 GeV/c^2 $\leq p \leq$ 90 GeV/c^2 and $\theta \leq$ 0.02 mrad).*

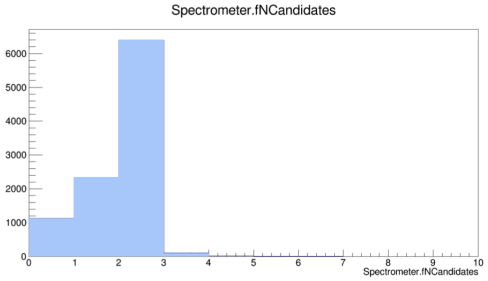

Figure 3.17: *Number of reconstructed tracks per event, for a different MC sample reconstructed with the customised configuration (5 GeV/c^2 $\leq p \leq$ 400 GeV/c^2 and $\theta \leq$ 0.05 mrad).*

3.8 Weight computation

At the MC simulation stage, the properties of all HNLs, also the ones with their decay products outside the CHOD acceptance, are stored in the output file. This is because the regeneration process is one of the techniques used to boost the probability of generating a signal event with final decay products in the NA62

geometric acceptance. At the analysis stage, all the discarded HNLs have to be taken into account.

Therefore, a weight must be associated with each HNL, representing the total probability of a two-body, fully-reconstructed HNL decay to occur with specific HNL properties, such as mass, coupling, lifetime, momentum, etc. Two libraries have been coded within the NA62 analysis framework, to compute the weight associated with each HNL in the MC output tree, so that the user can study the NA62 sensitivity to such decays as a function of the HNL coupling to SM leptons and its mass.

The weight depends on $U_\alpha^2, U_e^2, U_\mu^2$ and U_τ^2, where $\alpha = e, \mu, \tau$ is the flavour of the lepton produced in pair with the HNL. The weight corrects for all the techniques and approximations performed at the MC simulation stage. It is defined as follows:

$$W(U_\alpha^2, U_e^2, U_\mu^2, U_\tau^2) = \epsilon_D^{prod} \cdot F_{prod} \cdot U_\alpha^2 \cdot \epsilon_N^{reachFV} \cdot \epsilon_N^{decayFV} \cdot F_Z \cdot F_{decay}(U_e^2, U_\mu^2, U_\tau^2). \quad (3.76)$$

Each component of the weight is described in the following paragraphs. All plots are produced for the general model ($U_e^2 : U_\mu^2 : U_\tau^2 = 1{:}1{:}1$).

3.8.1 D meson weight components

At the MC stage, the probability for a proton to interact in the target/TAXes and produce a D meson has been assumed to be 1, so the weight must correct for this. The probability that a proton interacts with the Be target and a D meson is generated is

$$\epsilon_D^{prod-Be} = (\frac{\sigma_D^{prod}}{\sigma_p^{tot}})_{Be} = 0.00348, \quad (3.77)$$

where σ_D^{prod} is the D meson production cross section and σ_p^{tot} is the total proton cross section, in the Be case (target). The ratio $(\frac{\sigma_D^{prod}}{\sigma_p^{tot}})_{Be}$ has been provided within the NA62 collaboration using the Pythia software [64].

The production of D mesons by protons interacting in a material is a hard process and it depends linearly on the number of partons in the atoms of the material, A. The total interaction cross section of a proton is a soft process and a function of the nucleus area, $A^{\frac{2}{3}}$. Therefore, the ratio between the D meson production cross section and the total proton cross section can be computed, in the Cu case (TAXes):

$$\epsilon_D^{prod-Cu} = (\frac{\sigma_D^{prod}}{\sigma_p^{tot}})_{Cu} = (\frac{\sigma_D^{prod}}{\sigma_p^{tot}})_{Be} \cdot \frac{(\frac{\sigma_D^{prod}}{\sigma_p^{tot}})_{Cu}}{(\frac{\sigma_D^{prod}}{\sigma_p^{tot}})_{Be}} = (\frac{\sigma_D^{prod}}{\sigma_p^{tot}})_{Be} \cdot (\frac{A_{Cu}}{A_{Be}})^{\frac{1}{3}} = 0.00665, \quad (3.78)$$

where $A_{Cu} = 63$ and $A_{Be} = 9$ are the mass numbers of Cu and Be.

The first component of eq. 3.76, ϵ_D^{prod}, is either equal to $\epsilon_D^{prod-Be}$ or to $\epsilon_D^{prod-Cu}$ according to the material where the D meson is produced.

The second component in eq. 3.76, F_{prod}, is related to the fact that the HNL can be produced not only straightforward from a D meson decay, but also through the decay chain $D, D_S \to \tau\nu_\tau; \quad \tau \to NX$. Since the MC simulation does not take into account $BR(D, D_S \to \tau\nu_\tau)$ (as explained in Section 3.2), but only $BR(\tau \to NX)$, this must be corrected for. $BR(D_S \to \tau\nu_\tau) = 5.55 \cdot 10^{-2}$ and $BR(D \to \tau\nu_\tau) = 9.91 \cdot 10^{-4}$ [28] must be included in the weight. Therefore, for production modes from τ leptons,

$$F_{prod} = BR(D, D_S \to \tau\nu_\tau), \tag{3.79}$$

while, for any other production mode, $F_{prod} = 1$.

Finally, when computing the total BRs to choose the HNL production mode at the MC stage, it has been assumed that $U_\alpha^2 = 1$ and $U^2 = 3$. Therefore, the third factor in eq. 3.76, U_α^2, needs to be considered in the weight computation, and it must be equal to the flavour-specific coupling indicated in the production BR formula detailed in Appendix A.

3.8.2 Heavy Neutral Lepton weight components

During the MC generation, the HNLs are propagated to the beginning of the FV, to boost the probability of generating a signal event with final states in the NA62 geometric acceptance once more. The probability for the HNL to reach the fiducial volume without decaying is a function of the HNL lifetime and, hence, it depends on the value of the coupling U^2. Moreover, at the MC stage, the HNL is forced to decay in the FV according to a flat distribution; this also must be corrected for.

The product of the probabilities for the HNL to reach the FV and decay in it (fourth and fifth components in eq. 3.76) is:

$$\epsilon_N^{reachFV} \cdot \epsilon_N^{decayFV} = e^{-\frac{L_{bFV}}{\beta\gamma c\tau_N}}(1 - e^{-\frac{L_{FV}}{\beta\gamma c\tau_N}}), \tag{3.80}$$

where L_{bFV} is the distance between the HNL production point and the FV starting point (at $Z = 102.4$ m), $L_{FV} = 77.6$ m is the length of the FV (from 102.4 m to 180 m), β, γ and τ_N are the HNL β velocity, Lorentz factor and lifetime, where the last quantity is defined as

$$\tau_N = \frac{\hbar}{\Gamma_N^{tot}}. \tag{3.81}$$

Here, Γ_N^{tot} is the sum of all the HNL partial decay widths detailed in Appendix B, where also the anti-HNL partial widths are taken into account, since the HNL is

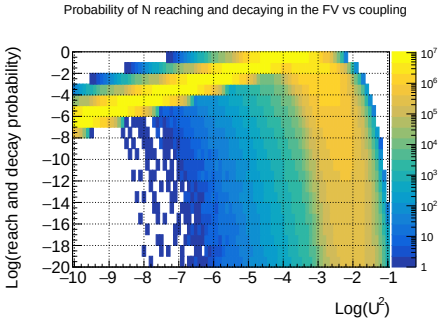

Figure 3.18: *MC event distribution in terms of product of the two probabilities for the HNL to reach the FV and decay in it and of the coupling, for* $m_N = 1\ GeV/c^2$ *and for the general model* ($U_e^2 : U_\mu^2 : U_\tau^2 = 1{:}1{:}1$).

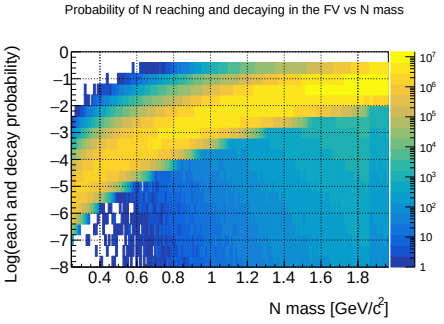

Figure 3.19: *MC event distribution in terms of product of the two probabilities for the HNL to reach the FV and decay in it and of the HNL mass, for* $U^2 = 10^{-6}$ *and for the general model* ($U_e^2 : U_\mu^2 : U_\tau^2 = 1{:}1{:}1$).

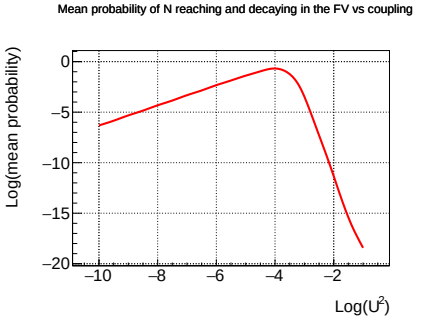

Figure 3.20: *Mean product of the two probabilities for the HNL to reach the FV and decay in it, as a function of the coupling, for* $m_N = 1\ GeV/c^2$ *and for the general model* ($U_e^2 : U_\mu^2 : U_\tau^2 = 1{:}1{:}1$).

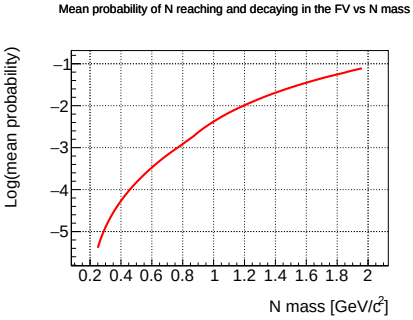

Figure 3.21: *Mean product of the two probabilities for the HNL to reach the FV and decay in it, as a function of the HNL mass, for* $U^2 = 10^{-6}$ *and for the general model* ($U_e^2 : U_\mu^2 : U_\tau^2 = 1{:}1{:}1$).

a Majorana particle in the considered theoretical scenarios. For this reason, the HNL total decay width is twice what it would be if the HNLs were Dirac particles. Each partial decay width has been multiplied by the corresponding flavour-specific coupling, so that

$$\Gamma_N^{tot}(U_e^2, U_\mu^2, U_\tau^2) = \sum_{i=1}^{n} \Gamma_i(U_e^2) + \sum_{j=1}^{m} \Gamma_j(U_\mu^2) + \sum_{k=1}^{l} \Gamma_k(U_\tau^2), \tag{3.82}$$

where n, m, l are the number of decay modes proportional to U_e^2, U_μ^2, U_τ^2 respectively.

All these quantities ($\epsilon_N^{reachFV}$, $\epsilon_N^{decayFV}$, τ_N and $\Gamma_N^{tot}(U_e^2, U_\mu^2, U_\tau^2)$) are coupling-dependent. The MC simulation forces the HNL to reach the FV and decay in it,

because introducing any coupling-dependent quantity would prevent the user from studying different scenarios according to the chosen coupling value. At the analysis stage, this is accounted for by introducing the needed coupling dependence.

In Fig. 3.18 and Fig. 3.19, the distribution of MC events in terms of product of the probabilities for the HNL to reach the FV and decay into it and of coupling and HNL mass, respectively, is shown.

If the mass is fixed, the larger the coupling, the shorter the lifetime and, thus, the smaller the probability to reach the FV without decaying. But the smaller the coupling, the longer the lifetime and, then, the smaller the probability to decay in the FV. Values of $\epsilon_N^{reachFV}\epsilon_N^{decayFV}$, therefore, tend to zero both for small and large couplings.

On the other hand, if the coupling is fixed, the smaller the mass, the fewer the decay modes the HNL can undergo and, then, the greater the probability to reach the FV. But the larger the mass, the greater the probability to decay in the FV. However, the product of the two probabilities is still greater for larger masses.

The mean product of the two probabilities of the whole MC sample is shown in Fig. 3.20 as a function of the coupling, for a fixed HNL mass, and in Fig. 3.21 as a function of the HNL mass, for a fixed coupling.

Another factor that must be computed at the analysis stage is F_Z, which accounts for the fact that the Z coordinate of the HNL decay point is generated flat in the MC simulation, which is not correct. Therefore,

$$F_Z = \frac{e^{-\frac{Z_D - L_{iFV}}{\beta\gamma c\tau_N}}}{1 - e^{-\frac{Z_{fFV} - L_{iFV}}{\beta\gamma c\tau_N}}}, \tag{3.83}$$

where Z_D is the Z coordinate of the HNL decay point, $L_{iFV} = 102.4$ m is the Z coordinate of the beginning of the FV and $Z_{fFV} = 180$ m is the Z coordinate of the end of the FV. The numerator of eq. 3.83 accounts for the fact that the Z coordinate of the HNL decay point should be an exponential function of Z, while the denominator ensures that a factor $F_Z > 1$ ($F_Z < 1$) is assigned to HNLs that decay at low (high) Z.

The distribution of Z_D as a function of the HNL momentum, weighted for the probability defined in eq. 3.83, is shown in Fig. 3.22 for a fixed coupling and HNL mass, and as a function of the coupling, for a fixed HNL mass, in Fig. 3.23.

The HNL total decay width, as defined in eq. 3.82, and the HNL lifetime (eq. 3.81) are also interesting to study as a function of the HNL coupling and its mass. For a fixed mass, the larger the coupling, the shorter the lifetime and the larger the total decay width. The same occurs for a fixed coupling and larger masses. These behaviours are shown in Fig. 3.24 to Fig. 3.27.

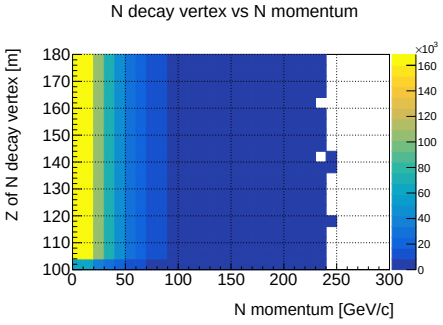

Figure 3.22: *Distribution of MC events in terms of Z coordinate of the HNL decay point and momentum, weighted for F_Z (as defined in eq. 3.83), for $m_N = 1\ GeV/c^2$, $U^2 = 10^{-6}$ and for the general model ($U_e^2 : U_\mu^2 : U_\tau^2 = 1{:}1{:}1$).*

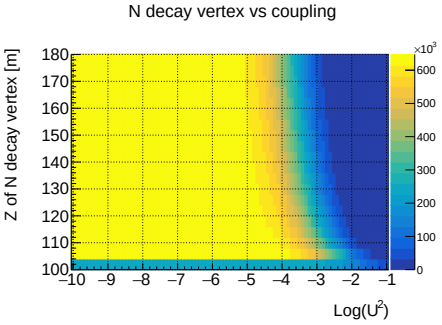

Figure 3.23: *Distribution of MC events in terms of Z coordinate of the HNL decay point and momentum, weighted for F_Z (as defined in eq. 3.83), for $m_N = 1\ GeV/c^2$ and for the general model ($U_e^2 : U_\mu^2 : U_\tau^2 = 1{:}1{:}1$).*

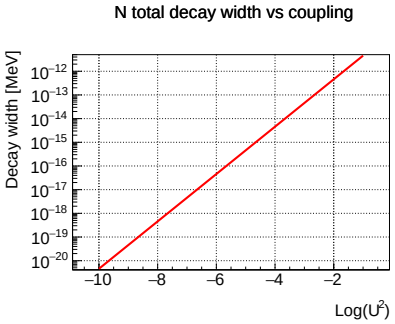

Figure 3.24: *HNL total decay width (as defined in eq. 3.82), as a function of the coupling, for $m_N = 1\ GeV/c^2$ and for the general model ($U_e^2 : U_\mu^2 : U_\tau^2 = 1{:}1{:}1$).*

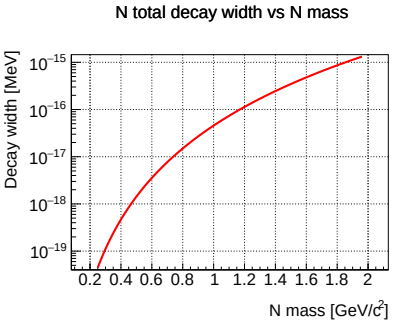

Figure 3.25: *HNL total decay width (as defined in eq. 3.82), as a function of the HNL mass, for $U^2 = 10^{-6}$ and for the general model ($U_e^2 : U_\mu^2 : U_\tau^2 = 1{:}1{:}1$).*

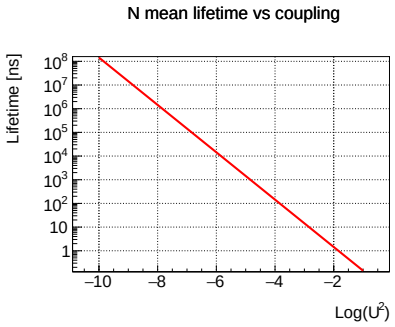

Figure 3.26: *HNL lifetime (as defined in eq. 3.81), as a function of the coupling, for $m_N = 1\ GeV/c^2$ and for the general model ($U_e^2 : U_\mu^2 : U_\tau^2 = 1{:}1{:}1$).*

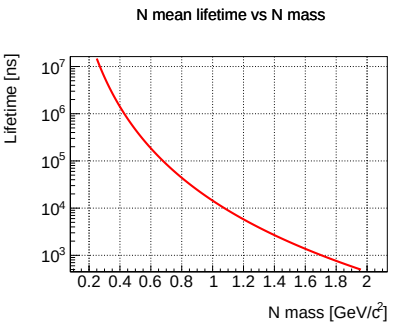

Figure 3.27: *HNL lifetime (as defined in eq. 3.81), as a function of the HNL mass, for $U^2 = 10^{-6}$ and for the general model ($U_e^2 : U_\mu^2 : U_\tau^2 = 1{:}1{:}1$).*

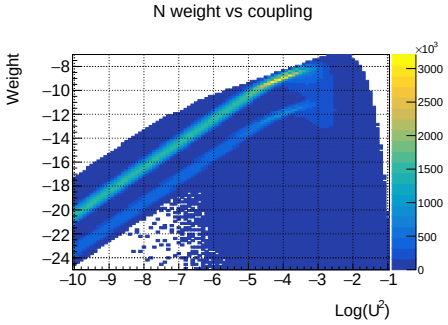

Figure 3.28: *Distribution of MC events in terms of HNL weight (eq. 3.76) and coupling, for $m_N = 1\ GeV/c^2$ and for the general model ($U_e^2 : U_\mu^2 : U_\tau^2 = 1{:}1{:}1$).*

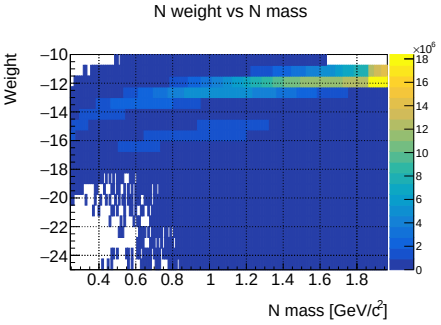

Figure 3.29: *Distribution of MC events in terms of HNL weight (eq. 3.76) and HNL mass, for $U^2 = 10^{-6}$ and for the general model ($U_e^2 : U_\mu^2 : U_\tau^2 = 1{:}1{:}1$).*

In the MC simulation, the HNL has been assumed to decay to $\pi\mu$ states only (or any two-body decay chosen to be simulated). It is therefore necessary to include in the weight a factor taking into account all the possible HNL decay modes:

$$F_{decay}(U_e^2, U_\mu^2, U_\tau^2) = \frac{\Gamma_N^{\pi\mu} \cdot U_\mu^2}{\Gamma_N^{tot}(U_e^2, U_\mu^2, U_\tau^2)}, \tag{3.84}$$

where all the partial decay widths have been defined in Appendix B and the coupling is taken into account.

It is worth noting that Γ_N^{tot} does not include subdominant HNL decay modes and it is not, therefore, the HNL total decay width. For the same reason, τ_N is not the HNL lifetime. These two quantities are referred to as total decay width and lifetime throughout the Chapter for convenience. The number of modes not accounted for in the simulation is unknown and, therefore, so is the underestimation (overestimation) of the HNL total decay width (lifetime). Nonetheless, the whole procedure detailed in this thesis holds.

In fact, the number N_N of HNLs decayed at a time t is proportional to $1 - e^{-\frac{t}{\tau_N}}$. If N_N is expanded into a Taylor series,

$$N_N \approx 1 - (1 - \frac{t}{\tau_N} + \frac{t^2}{\tau_N^2}) = \frac{t}{\tau_N} - \frac{t^2}{\tau_N^2}. \tag{3.85}$$

If the HNL lifetime is sufficiently large, the second term in eq. 3.85 is negligible and

$$N_N \approx \frac{t}{\tau_N}. \tag{3.86}$$

One can consider the case where only one decay mode is searched for and taken into account for computing the HNL total decay width and lifetime, and N_N is calculated according to eq. 3.86.

In the case where only one decay mode is searched for but two of them are considered, the HNL total decay width doubles, the lifetime halves and N_N doubles as a consequence. Nonetheless, an extra factor, $\alpha = \frac{1}{2}$, must be taken into account, since only half of the decayed HNLs now go into the channel searched for:

$$N'_N \approx \frac{t}{\tau'_N} \cdot \alpha = 2 \cdot \frac{t}{\tau_N} \cdot \frac{1}{2} = N_N. \tag{3.87}$$

This proves that, when the HNL lifetime is large enough, the number of decay modes considered to compute τ_N is irrelevant.

If the HNL lifetime is sufficiently small, on the contrary, the second term in eq. 3.85 is not negligible anymore. Therefore, in case two decay channels are considered

to compute τ_N,

$$N'_N \approx (\frac{t}{\tau'_N} - \frac{t^2}{\tau'^2_N}) \cdot \alpha = (\frac{2t}{\tau'_N} - \frac{4t^2}{\tau'^2_N}) \cdot \frac{1}{2} \neq N_N. \tag{3.88}$$

In case the HNL lifetime is small enough, the number of decay modes considered to compute τ_N becomes relevant. Nonetheless, NA62 is not sensitive to short-lived HNLs, since they decay upstream of the fiducial volume. Therefore, the number of HNL decay modes considered in this simulation is irrelevant. They have been included in the MC simulation only for completeness.

This means that the results achieved with this simulation hold, despite not accounting for all possible HNL decay modes, since the weight does not depend on the HNL lifetime, if this is sufficiently large.

In the next Sections, two weights will be used to study the NA62 sensitivity to $N \to \pi\mu$ decays. One is the weight detailed in eq. 3.76, the other is the same weight but without the F_Z factor:

$$W'(U^2_\alpha, U^2_e, U^2_\mu, U^2_\tau) = \epsilon^{prod}_D \cdot F_{prod} \cdot U^2_\alpha \cdot \epsilon^{reachFV}_N \cdot \epsilon^{decayFV}_N \cdot F_{decay}(U^2_e, U^2_\mu, U^2_\tau). \tag{3.89}$$

The reason behind this double definition of the weight is explained in Chapter 4.

3.8.3 Weight computation summary

A brief summary of the detailed weight procedure is given in the following.

At the analysis stage, all HNLs are retrieved from the output file, and a weight (depending on the fourth power of the coupling) is computed for each of them, representing the total probability of a two-body, fully-reconstructed HNL decay to occur with certain HNL properties.

Fig. 3.28 and Fig. 3.29 show the weight distribution (as written in eq. 3.76), respectively, as a function of the coupling and the HNL mass.

Chapter 4

Evaluation of expected sensitivity

4.1 Event selection

By analysing the MC events generated with the simulation and reconstructed using the NA62 framework, the NA62 expected sensitivity to $N \to \pi\mu$ signals can be computed.

In order to do so, a private analyser is run on the HNL MC events. This analyser contains a selection optimised to maximise the signal acceptance and eliminate as much as possible all background sources from the data sample collected for HNL decay searches, in order to achieve the zero-background hypothesis under which expected sensitivity curves are produced, by running the same event selection on the HNL MC sample. To achieve the double goal of signal maximisation and zero-background hypothesis, the event selection is designed to only pick in-time two-track events with:

- zero total charge;
- one track associated to a muon signal and the other one not;
- different ranges of $\frac{E}{p}$ values for each track for pion/muon identification;
- a vertex distant enough from the beamline and no signal in time from the kaon tagger, to reject as much as possible all background sources coming from kaon decays.

The selection is kept independent of any coupling hypothesis. All the figures in this Section are related to the pion-muon pair associated with the good HNLs only, and are produced for HNL with $m_N < 0.5$ GeV/c^2 and $m_N > 1.5$ GeV/c^2, to allow for comparison of distributions at different mass values.

Several cuts are applied: in order, track cuts, energy cuts, veto cuts and geometrical cuts. It has to be noted that events surviving a certain set of cuts have

also survived the cuts listed before those (for example, events passing the veto cuts have also survived the track and energy cuts). All cuts related to the decay-product track times are only effective when the event selection is run on data sets. In fact, the decay products are time aligned in the MC simulation and, therefore, always survive timing cuts.

The same consideration applies to cuts related to the trigger conditions, since MC events do not need to be triggered by either the L0TP or the L1 software.

4.1.1 Track cuts

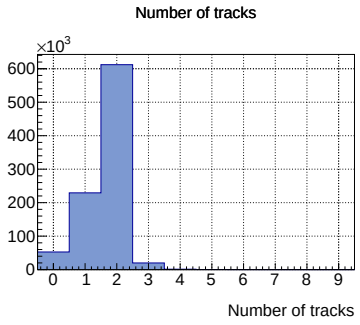

Figure 4.1: *Number of tracks for all reconstructed MC events with $m_N < 0.5$ GeV/c^2.*

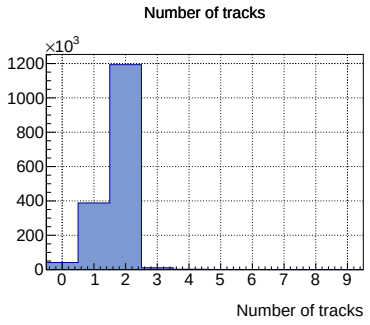

Figure 4.2: *Number of tracks for all reconstructed MC events with $m_N > 1.5$ GeV/c^2.*

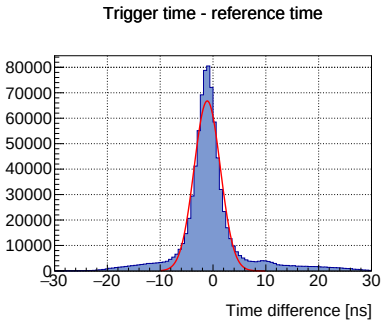

Figure 4.3: *Difference between the L0TP time and each track time, given by the CHOD, for all two-track reconstructed data events (the MC events are time aligned). The distribution is fitted with a Gaussian function whose RMS is used to compute the window of the related time cut.*

The first cut that is applied is related to the L0 trigger. It is required that the

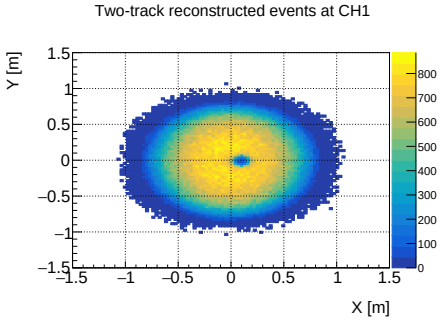

Figure 4.4: *X, Y distribution of two-track reconstructed MC events at the Straw spectrometer chamber 1, with $m_N < 0.5$ GeV/c^2.*

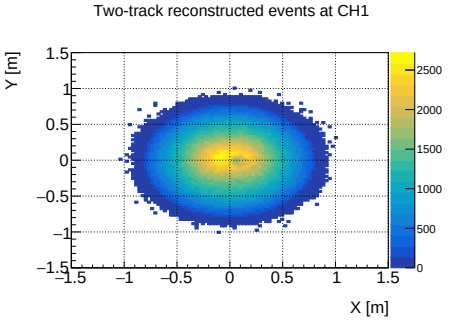

Figure 4.5: *X, Y distribution of two-track reconstructed MC events at the Straw spectrometer chamber 1, with $m_N > 1.5$ GeV/c^2.*

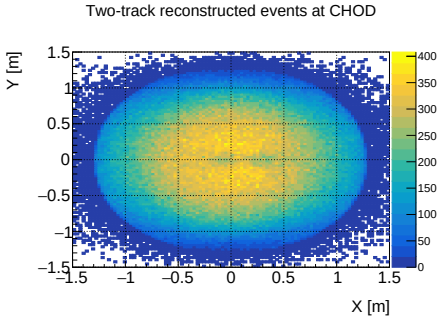

Figure 4.6: *X, Y distribution of two-track reconstructed MC events at the CHOD, with $m_N < 0.5$ GeV/c^2. The halo at distances greater than 1.3 m from the center (the value for the CHOD radius at the MC stage, used to check whether the decay products are in its geometric acceptance) is due to final-state pions decaying in flight.*

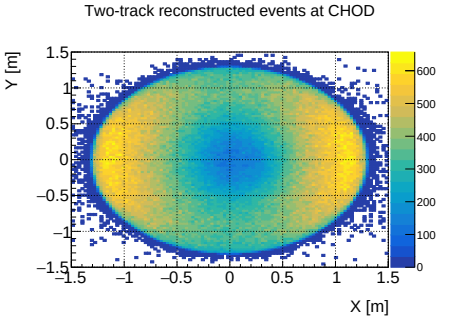

Figure 4.7: *X, Y distribution of two-track reconstructed MC events at the CHOD, with $m_N > 1.5$ GeV/c^2. The halo at distances greater than 1.3 m from the center (the value for the CHOD radius at the MC stage, used to check whether the decay products are in its geometric acceptance) is due to final-state pions decaying in flight.*

event has been triggered by the "muon exotic" primitive, namely RICH-Q2-M(O)1. Then, it is asked that also the L1 requirement of notKTAG-notLAV-StrawExo is fulfilled.

Afterwards, events with two tracks reconstructed in the Spectrometer are selected (Fig. 4.1 and Fig. 4.2). It is required that the times of both tracks (as measured by the CHOD) are in a ± 6 ns window from the event time provided by the L0TP. By studying the distribution of the difference between the L0TP time and the CHOD track times (Fig. 4.3), a time window of $\pm 5\sigma$ has been chosen, where σ is the RMS of this distribution, fitted between [-10, 10] ns. The same procedure has been followed to compute all the time windows used in the timing cuts described in the event selection.

If the CHOD track times meet the above requirement, the L0TP time is considered as the track reference time for all following timing cuts.

No in-time KTAG signals must be found in more than four KTAG sectors and in a time window of ± 5 ns from the L0TP time. This is done to remove as much as possible all background sources originating from beam-kaon decays.

Then, both tracks need to meet several quality requirements.

Each track has to have $\chi^2 < 20$ and the total charge of the two tracks must be zero.

Several standard tools provided by the NA62 framework are used to check that both tracks are in the geometric acceptance of all four Spectrometer chambers (Fig. 4.4 and Fig. 4.5), CHOD (Fig. 4.6 and Fig. 4.7), NewCHOD, LKr, and MUV3 and outside the LAV12 geometric acceptance (all acceptance checks are performed using the standard conditions).

Each downstream track must be associated with at least one signal in the CHOD and the NewCHOD, but the two tracks must not be associated with the same CHOD/NewCHOD signal, and the distance between two signals at the CHOD plane must be greater than 20 cm. Moreover, at least one NewCHOD signal associated with each track must be within a time window of ± 9 ns from the L0TP time.

One of the two tracks is required to be associated with one and only one MUV3 signal, which has to lie in a ± 8 ns time window from the L0TP time. The other track must not be associated with the MUV3 at all, while it has to be associated with at least one signal in the LKr (time window of ± 10 ns from L0TP).

Fig. 4.8, Fig. 4.9, Fig. 4.10 and Fig. 4.11 show the distribution of the HNL decay products after this set of track cuts.

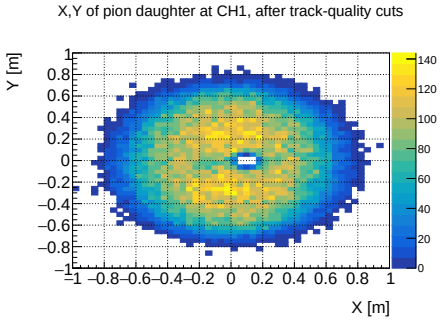

Figure 4.8: *X, Y distribution of pion decay products at the Straw spectrometer chamber 1 after track cuts, with $m_N < 0.5$ GeV/c^2.*

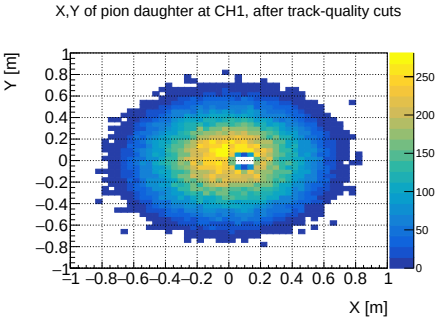

Figure 4.9: *X, Y distribution of pion decay products at the Straw spectrometer chamber 1 after track cuts, with $m_N > 1.5$ GeV/c^2.*

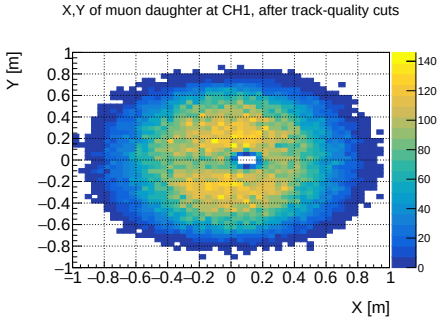

Figure 4.10: *X, Y distribution of muon decay products at the Straw spectrometer chamber 1 after track cuts, with $m_N < 0.5$ GeV/c^2.*

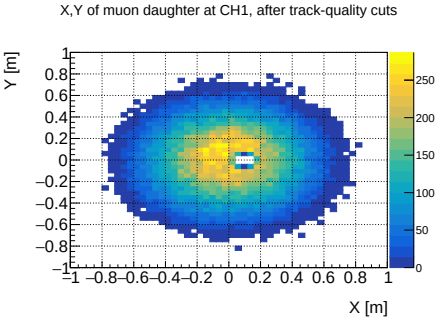

Figure 4.11: *X, Y distribution of muon decay products at the Straw spectrometer chamber 1 after track cuts, with $m_N > 1.5$ GeV/c^2.*

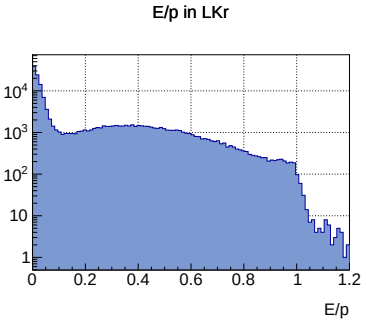

Figure 4.12: *The ratio $\frac{E}{p}$ for each track passing the track cuts, with $m_N < 0.5$ GeV/c^2.*

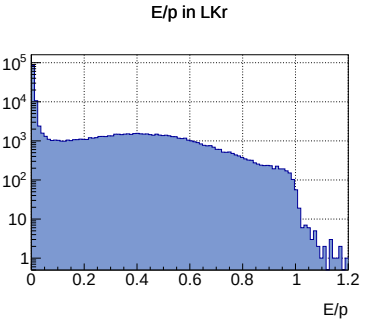

Figure 4.13: *The ratio $\frac{E}{p}$ for each track passing the track cuts, with $m_N > 1.5$ GeV/c^2.*

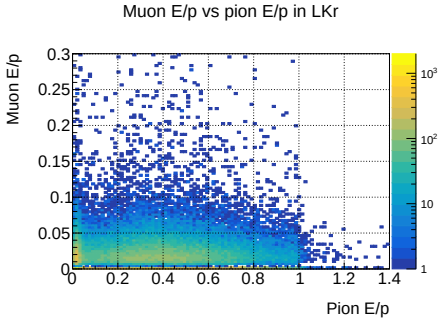

Figure 4.14: *Muon $\frac{E}{p}$ vs pion $\frac{E}{p}$ for two-track reconstructed MC events passing the track cuts, with $m_N < 0.5$ GeV/c^2. The peak at low $\frac{E}{p}$ is due to pions decaying to muons.*

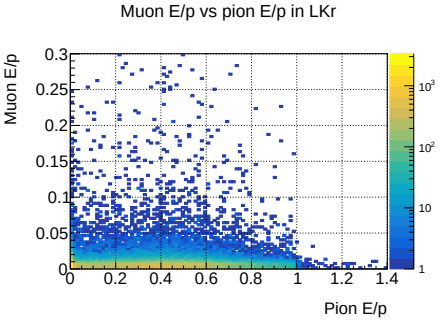

Figure 4.15: *Muon $\frac{E}{p}$ vs pion $\frac{E}{p}$ for two-track reconstructed MC events passing the track cuts, with $m_N > 1.5$ GeV/c^2. The peak at low $\frac{E}{p}$ is due to pions decaying to muons.*

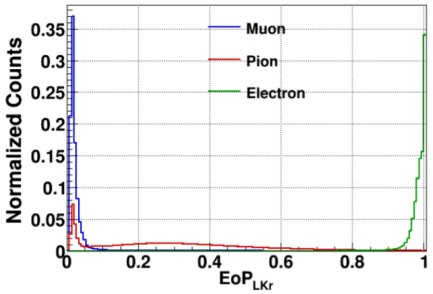

Figure 4.16: *A typical $\frac{E}{p}$ distribution of data events at NA62: the muon (blue), pion (red) and electron (green) peaks are visible. The red peak at low $\frac{E}{p}$ is due to pions decaying to muons.*

4.1.2 Energy and veto cuts

The ratio $\frac{E}{p}$ between the reconstructed track energy and the modulus of its three-momentum is then considered. To further reject two track events in which a muon-pion pair is not present, the track associated to the MUV3 (the muon) must have $\frac{E}{p} < 0.2$, while the other track (the pion) needs to have $\frac{E}{p} < 0.8$ (Fig. 4.12, Fig. 4.13, Fig. 4.14 and Fig. 4.15). A typical $\frac{E}{p}$ distribution at NA62 is shown in Fig. 4.16, where the peaks generated by muons, pions and electrons are visible.

Veto cuts are then applied to events surviving up to this stage. There must be no LAV and SAV activity associated with the event (in a time window of $\pm$ 10 ns). The event time, in this case, is taken as the average of the two track times provided by the CHOD.

It is also required that no activity is detected in the CHANTI in a $\pm$ 13 ns window from the L0TP time.

4.1.3 Geometrical cuts

The last set of cuts applied to the reconstructed events is related to several geometrical quantities, to reject events coming from beam kaon decays, whose products may mimic a signal-like pion-muon pair. The difference between these background events and the signal events is that vertices of pion-muon pairs coming from HNL decays are more displaced with respect to the beam axis than pairs coming from the bulk of kaon decays.

For these cuts, the Closest Distance of Approach (CDA) algorithm is used (provided within the NA62 framework), which computes the distance between two lines. Several geometrical cuts are then applied. The CDA between the two tracks must be less than 1 cm. The distance between the two tracks at the first Spectrometer chamber, in the (X, Y) plane, must be greater than 2 cm. The distance between the reconstructed two-track vertex and the beam axis must be greater than 10 cm, and the Z coordinate of the vertex has to be in the FV, defined as 120 m - 180 m (the range between 102.4 m and 120 m has been reserved for data-driven background studies). Within NA62, fits on track vertices are not carried out yet, since an algorithm to perform them is currently under development. This could be used to further improve the quality of the two-track vertices searched for with this event selection.

Fig. 4.17 and Fig. 4.18 show the distribution of the distance between the two-track vertex and the beam axis as a function of the Z coordinate of the two-track vertex, before any cut and for the two HNL mass ranges of $m_N < 0.5$ GeV/c^2 and $m_N > 1.5$ GeV/c^2, whereas Fig. 4.19 and Fig. 4.20 display the same distribution

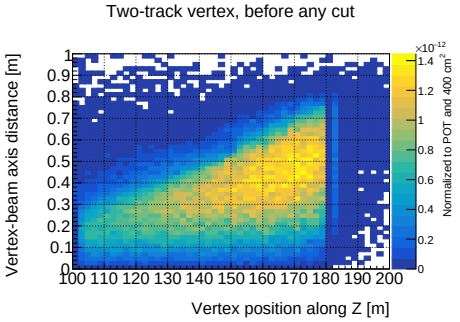

Figure 4.17: *Distance of the two-track vertex from the beam axis vs Z coordinate of the two-track vertex, before any cuts. This plot is produced for two-track reconstructed MC events with $m_N < 0.5$ GeV/c^2, U^2 =10^{-6} and for the general model ($U_e^2 : U_\mu^2 : U_\tau^2$ = 1:1:1).*

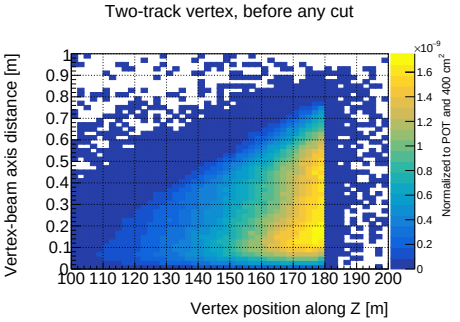

Figure 4.18: *Distance of the two-track vertex from the beam axis vs Z coordinate of the two-track vertex, before any cuts. This plot is produced for two-track reconstructed MC events with $m_N > 1.5$ GeV/c^2, U^2 =10^{-6} and for the general model ($U_e^2 : U_\mu^2 : U_\tau^2$ = 1:1:1).*

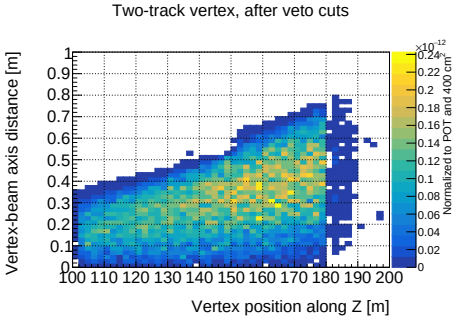

Figure 4.19: *Distance of the two-track vertex from the beam axis vs Z coordinate of the two-track vertex, for two-track reconstructed MC events with $m_N < 0.5$ GeV/c^2 and surviving track, energy and veto cuts, the cut on the track-to-track CDA and the cut on the distance between the two tracks at the first Spectrometer chamber. This plot is produced for U^2 =10^{-6} and for the general model ($U_e^2 : U_\mu^2 : U_\tau^2$ = 1:1:1).*

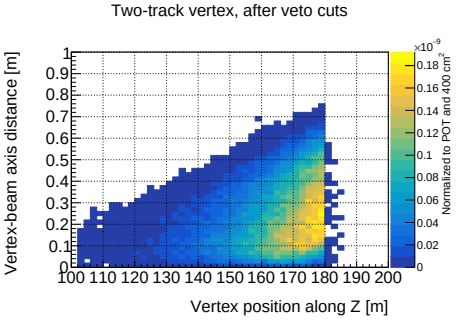

Figure 4.20: *Distance of the two-track vertex from the beam axis vs Z coordinate of the two-track vertex, for two-track reconstructed MC events with $m_N > 1.5$ GeV/c^2 and surviving track, energy and veto cuts, the cut on the track-to-track CDA and the cut on the distance between the two tracks at the first Spectrometer chamber. This plot is produced for U^2 =10^{-6} and for the general model ($U_e^2 : U_\mu^2 : U_\tau^2$ = 1:1:1).*

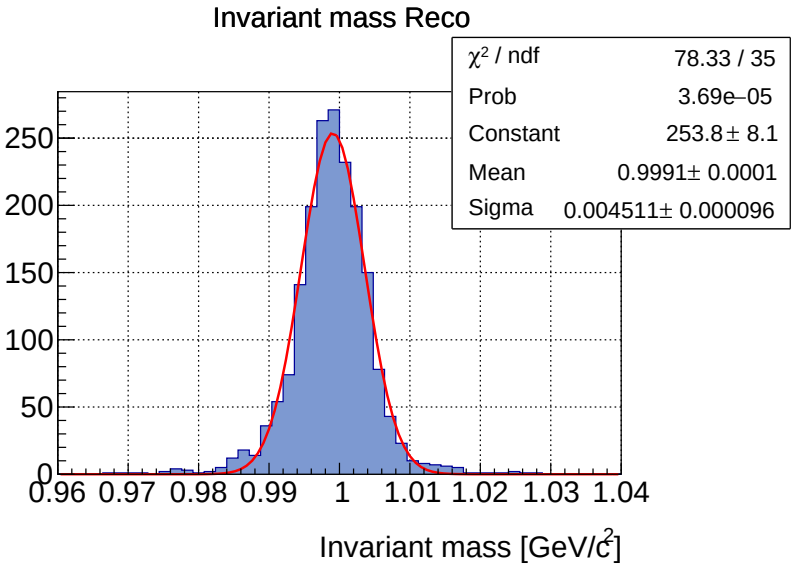

Figure 4.21: *Invariant mass for reconstructed MC events passing the whole selection, for $m_N = 1$ GeV/c^2.*

but after track, energy and veto cuts have been applied. The two-track events in each of these plots are weighted on the Z axis with the corresponding HNL weights, as described in Section 3.8.

4.1.4 Signal regions

The squared invariant mass is computed for all events surviving the whole selection:

$$m^2 = (E_\pi + E_\mu)^2 - |\vec{p}_\pi + \vec{p}_\mu|^2. \tag{4.1}$$

As seen in Fig. 4.21, this distribution is centred, as expected, on the HNL mass (1 GeV/c^2 in this case).

At this point, a signal region for $N \to \pi\mu$ events can be built. The CDA of the HNL trajectory with respect to the proton trajectory (or proton line) is computed which, together with its Z coordinate, are the two variables used to define the signal region. To have a unique signal region for both event types (target-produced and TAX-produced), the proton trajectory is defined as a straight line connecting the average HNL production point in the target, at $X = 0, Y = 0, Z = -26.5$ mm, to the one in the TAXes, at $X = 0, Y = -22$ mm, $Z = 23.23$ m.

Fig. 4.22 and Fig. 4.23 show the signal region for the target-produced component of the events, before and after all cuts, for $m_N < 0.5$ GeV/c^2, while Fig. 4.24 and Fig. 4.25 display such quantities for $m_N > 1.5$ GeV/c^2. Fig. 4.26 and Fig. 4.27 show the same distributions for TAX-produced events, for $m_N < 0.5$ GeV/c^2, and

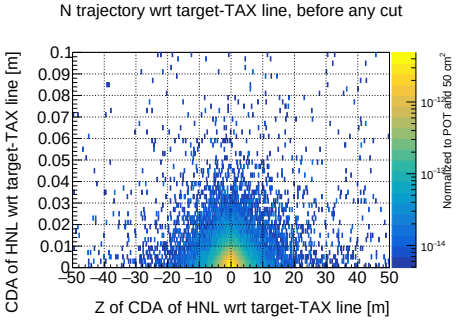

Figure 4.22: *Signal region: CDA vs Z coordinate of the CDA of the HNL trajectory with respect to the proton line. This plot refers to two-track reconstructed MC events produced in the target, before any cuts, with* $m_N < 0.5\ GeV/c^2$, $U^2 = 10^{-6}$ *and for the general model* ($U_e^2 : U_\mu^2 : U_\tau^2 = 1:1:1$).

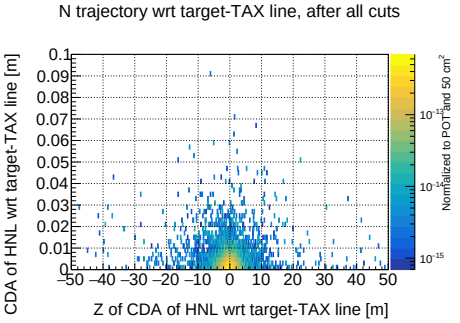

Figure 4.23: *Signal region: CDA vs Z coordinate of the CDA of the HNL trajectory with respect to the proton line. This plot refers to two-track reconstructed MC events produced in the target, after all cuts, with* $m_N < 0.5\ GeV/c^2$, $U^2 = 10^{-6}$ *and for the general model* ($U_e^2 : U_\mu^2 : U_\tau^2 = 1:1:1$).

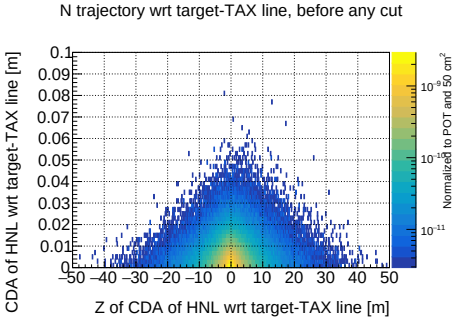

Figure 4.24: *Signal region: CDA vs Z coordinate of the CDA of the HNL trajectory with respect to the proton line. This plot refers to two-track reconstructed MC events produced in the target, before any cuts, with* $m_N > 1.5\ GeV/c^2$, $U^2 = 10^{-6}$ *and for the general model* ($U_e^2 : U_\mu^2 : U_\tau^2 = 1:1:1$).

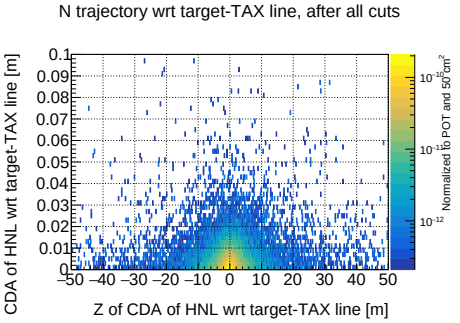

Figure 4.25: *Signal region: CDA vs Z coordinate of the CDA of the HNL trajectory with respect to the proton line. This plot refers to two-track reconstructed MC events produced in the target, after all cuts, with* $m_N > 1.5\ GeV/c^2$, $U^2 = 10^{-6}$ *and for the general model* ($U_e^2 : U_\mu^2 : U_\tau^2 = 1:1:1$).

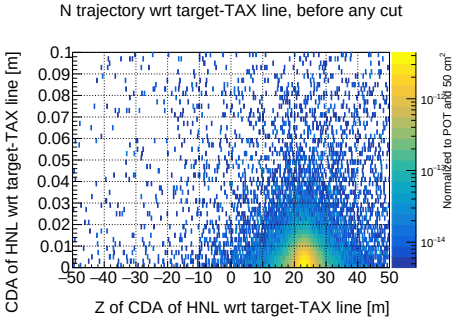

Figure 4.26: *Signal region: CDA vs Z coordinate of the CDA of the HNL trajectory with respect to the proton line. This plot refers to two-track reconstructed MC events produced in the TAXes, before any cuts, with* $m_N < 0.5\ GeV/c^2$, $U^2 = 10^{-6}$ *and for the general model* ($U_e^2 : U_\mu^2 : U_\tau^2 = 1:1:1$).

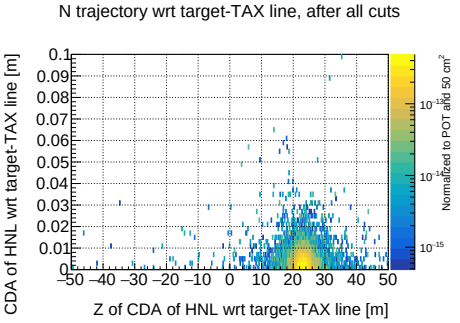

Figure 4.27: *Signal region: CDA vs Z coordinate of the CDA of the HNL trajectory with respect to the proton line. This plot refers to two-track reconstructed MC events produced in the TAXes, after all cuts, with* $m_N < 0.5\ GeV/c^2$, $U^2 = 10^{-6}$ *and for the general model* ($U_e^2 : U_\mu^2 : U_\tau^2 = 1:1:1$).

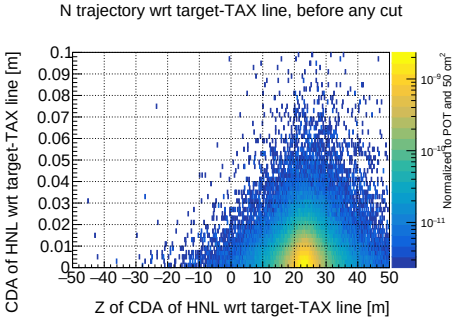

Figure 4.28: *Signal region: CDA vs Z coordinate of the CDA of the HNL trajectory with respect to the proton line. This plot refers to two-track reconstructed MC events produced in the TAXes, before any cuts, with* $m_N > 1.5\ GeV/c^2$, $U^2 = 10^{-6}$ *and for the general model* ($U_e^2 : U_\mu^2 : U_\tau^2 = 1:1:1$).

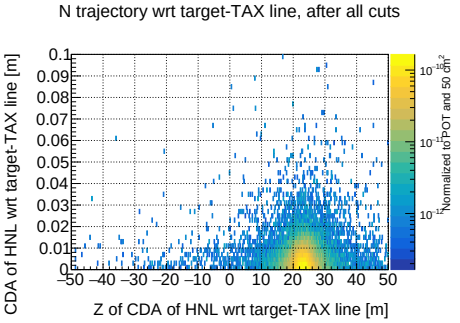

Figure 4.29: *Signal region: CDA vs Z coordinate of the CDA of the HNL trajectory with respect to the proton line. This plot refers to two-track reconstructed MC events produced in the TAXes, after all cuts, with* $m_N > 1.5\ GeV/c^2$, $U^2 = 10^{-6}$ *and for the general model* ($U_e^2 : U_\mu^2 : U_\tau^2 = 1:1:1$).

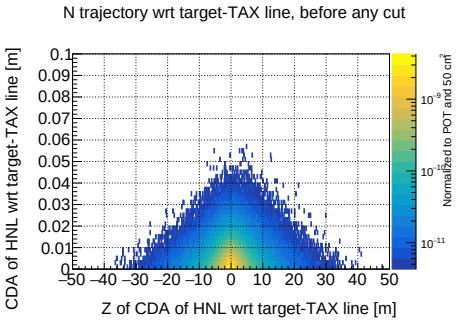

Figure 4.30: *Signal region: CDA vs Z coordinate of the CDA of the HNL trajectory with respect to the proton line. This plot refers to two-track reconstructed MC events produced in the target, before any cuts, generated from all HNL masses, $U^2 = 10^{-6}$ and for the general model ($U_e^2 : U_\mu^2 : U_\tau^2 = 1:1:1$).*

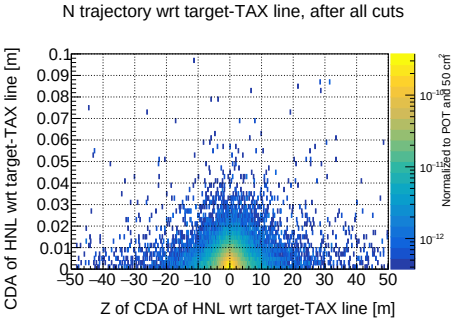

Figure 4.31: *Signal region: CDA vs Z coordinate of the CDA of the HNL trajectory with respect to the proton line. This plot refers to two-track reconstructed MC events produced in the target, after all cuts, generated from all HNL masses, $U^2 = 10^{-6}$ and for the general model ($U_e^2 : U_\mu^2 : U_\tau^2 = 1:1:1$).*

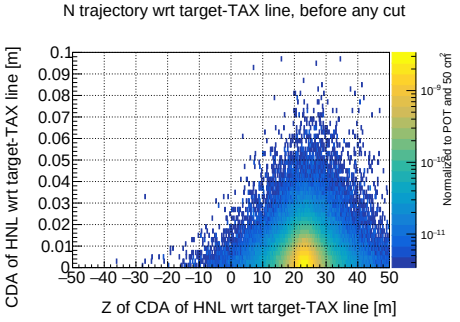

Figure 4.32: *Signal region: CDA vs Z coordinate of the CDA of the HNL trajectory with respect to the proton line. This plot refers to two-track reconstructed MC events produced in the TAXes, before any cuts, generated from all HNL masses, $U^2 = 10^{-6}$ and for the general model ($U_e^2 : U_\mu^2 : U_\tau^2 = 1:1:1$).*

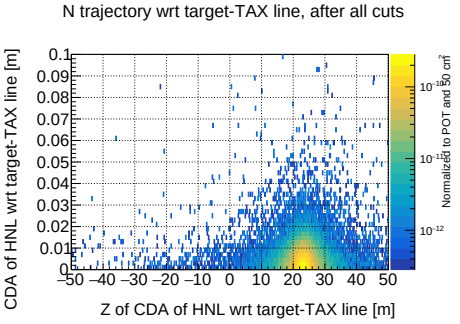

Figure 4.33: *Signal region: CDA vs Z coordinate of the CDA of the HNL trajectory with respect to the proton line. This plot refers to two-track reconstructed MC events produced in the TAXes, after all cuts, generated from all HNL masses, $U^2 = 10^{-6}$ and for the general model ($U_e^2 : U_\mu^2 : U_\tau^2 = 1:1:1$).*

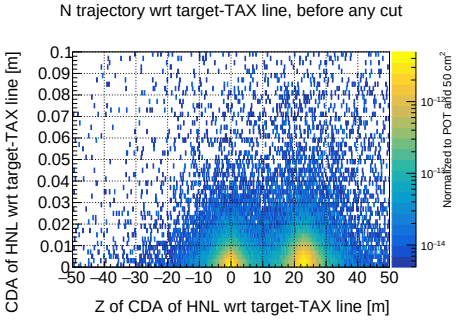

Figure 4.34: *Signal region: CDA vs Z coordinate of the CDA of the HNL trajectory with respect to the proton line. This plot refers to two-track reconstructed MC events produced both in the target and the TAXes, before all cuts, with $m_N < 0.5$ GeV/c^2, $U^2 = 10^{-6}$ and for the general model ($U_e^2 : U_\mu^2 : U_\tau^2 = 1:1:1$).*

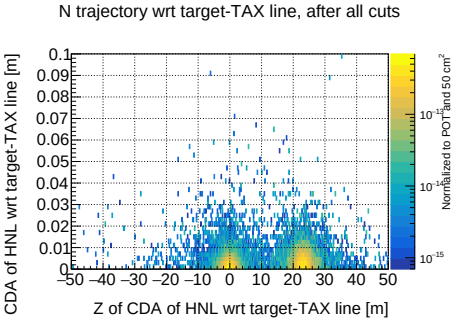

Figure 4.35: *Signal region: CDA vs Z coordinate of the CDA of the HNL trajectory with respect to the proton line. This plot refers to two-track reconstructed MC events produced both in the target and the TAXes, after all cuts, with $m_N < 0.5$ GeV/c^2, $U^2 = 10^{-6}$ and for the general model ($U_e^2 : U_\mu^2 : U_\tau^2 = 1:1:1$).*

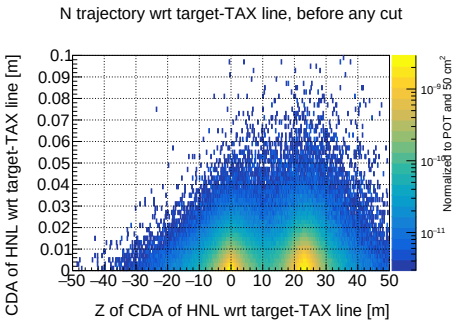

Figure 4.36: *Signal region: CDA vs Z coordinate of the CDA of the HNL trajectory with respect to the proton line. This plot refers to two-track reconstructed MC events produced both in the target and the TAXes, before all cuts, with $m_N > 1.5$ GeV/c^2, $U^2 = 10^{-6}$ and for the general model ($U_e^2 : U_\mu^2 : U_\tau^2 = 1:1:1$).*

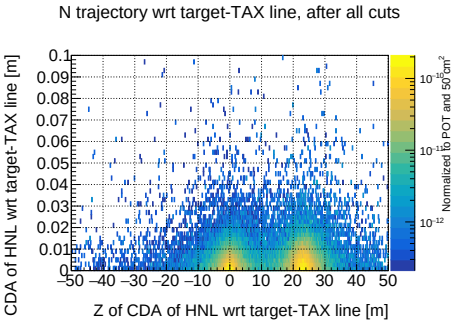

Figure 4.37: *Signal region: CDA vs Z coordinate of the CDA of the HNL trajectory with respect to the proton line. This plot refers to two-track reconstructed MC events produced both in the target and the TAXes, after all cuts, with $m_N > 1.5$ GeV/c^2, $U^2 = 10^{-6}$ and for the general model ($U_e^2 : U_\mu^2 : U_\tau^2 = 1:1:1$).*

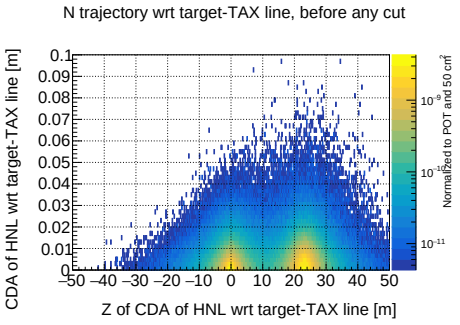

Figure 4.38: *Signal region: CDA vs Z coordinate of the CDA of the HNL trajectory with respect to the proton line. This plot refers to two-track reconstructed MC events produced both in the target and the TAXes, before all cuts, generated from all HNL masses, $U^2 = 10^{-6}$ and for the general model ($U_e^2 : U_\mu^2 : U_\tau^2 = 1{:}1{:}1$).*

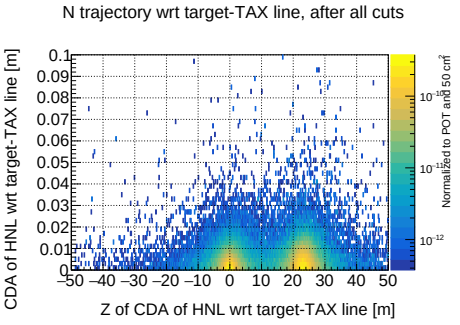

Figure 4.39: *Signal region: CDA vs Z coordinate of the CDA of the HNL trajectory with respect to the proton line. This plot refers to two-track reconstructed MC events produced both in the target and the TAXes, after all cuts, generated from all HNL masses, $U^2 = 10^{-6}$ and for the general model ($U_e^2 : U_\mu^2 : U_\tau^2 = 1{:}1{:}1$).*

Fig. 4.28 and Fig. 4.29 display them for $m_N > 1.5$ GeV/c^2. In Fig. 4.34 and Fig. 4.35, the two components are shown in the same plot for $m_N < 0.5$ GeV/c^2, whereas the same quantities are displayed in Fig. 4.36 and Fig. 4.37 for $m_N > 1.5$ GeV/c^2. Therefore, a unique signal region can be studied for both production components. Analogous distributions are also shown for MC events with all masses generated by the simulation. Fig. 4.30 and Fig. 4.31 display the signal region for the target-produced component of such events, before and after all cuts, while Fig. 4.32 and Fig. 4.33 show the same distributions for TAX-produced events. In Fig. 4.38 and Fig. 4.39, the two components are shown in the same plot. The events in each signal region plot shown in this Section are weighted on the Z axis with the corresponding HNL weights, as described in Section 3.8.

4.2 Expected yield

One can then compute the expected sensitivity to $N \to \pi\mu$ events with the NA62 detector as a function of the HNL coupling to SM leptons and its mass, by retrieving the weights associated with all HNLs in the MC sample, according to their mass and the value assigned to the coupling.

The weights are used to compute the yield per POT, Y_{POT}, as a function of the HNL mass and coupling, which is defined as the probability, for each POT, that a $N \to \pi\mu$ decay occurs, is detected and passes the event selection.

The yield per POT can be defined as the product of three acceptances, as follows:

$$Y_{POT} = A_{FV} \cdot A_{regeneration} \cdot A_{selection} = \frac{\sum_{i=1}^{A} W_i'}{N} \cdot \frac{\sum_{j=1}^{G} W_j}{\sum_{k=1}^{B} W_k} \cdot \frac{\sum_{l=1}^{S} W_l}{\sum_{j=1}^{G} W_j} = \frac{\sum_{i=1}^{A} W_i' \cdot \sum_{l=1}^{S} W_l}{\sum_{k=1}^{B} W_k \cdot N}; \quad (4.2)$$

A_{FV} is the acceptance for the HNLs to reach the FV and decay in it, defined as the ratio between the sum of weights of all the HNLs (A) and the number of HNLs in the whole MC sample (N). This term only considers the number of HNLs that reach the FV and decay in it, out of all the ones that are produced in the simulation. For this reason, the HNL decay point is not considered to compute this term and, therefore, the weight defined in eq. 3.89 is used.

$A_{regeneration}$ is the acceptance of the regeneration process at the MC stage, that is the fraction of all the HNLs (B) with both decay products in the CHOD geometric acceptance (G). In this case, since it is considered that all HNLs have reached the FV and have decayed in it, the HNL decay point must be exponentially reweighted, and the formula in eq. 3.76 is used.

$A_{selection}$ is the acceptance of the event selection, defined as the fraction of all HNLs in the MC sample with both decay products in the CHOD geometric acceptance (G) that also pass all the cuts (S). For analogous considerations as in the case of $A_{regeneration}$, the weight used here is the one in eq. 3.76. This corrects for the flat distribution used to extract the Z coordinate of the HNL decay point at the MC stage.

4.2.1 Expected yield as a function of the coupling

The three acceptances and the yield per POT as a function of the coupling, for a fixed mass, are shown in Fig. 4.40 to Fig. 4.43.

The yields for target and TAX production are computed for each coupling bin and then normalised to the total number of HNLs in the sample. By doing this, the total yield shown in Fig. 4.43 (red dots) is the sum of the target- and TAX-produced yields (blue and green dots respectively) shown in the same plot.

The total acceptances plotted in Fig. 4.40 to Fig. 4.42 (red dots) are the average of the corresponding target- and TAX-related acceptances (blue and green dots).

The FV acceptance (Fig. 4.40) follows the trend of Fig. 3.20, according to the fact that too small and too large couplings minimise the product of the probabilities for the HNL to reach the FV and decay in it. At large couplings, where the HNLs are likely to decay before reaching the FV, the target-production contribution is negligible to the TAX one. This is due to the fact that the HNLs produced in the

TAXes are closer to the beginning of the FV and are therefore more likely to reach it.

The trend of the regeneration acceptance (Fig. 4.41) is due to the fact that, at small couplings, the HNLs decay with a flat distribution along the FV. For large couplings, despite the fact that the majority of the HNLs decay at the beginning of the FV, those that decay close to the end of it give a larger contribution to the trend. Since these HNLs are more boosted, their decay products have small transverse momenta and they more easily get into the CHOD geometric acceptance. In this plot, the trend of the target-produced sample drops at large couplings. This is due to the fact that a boosted HNL, when produced in the target, must travel a longer distance to get to the FV, with respect to an HNL with the same properties but produced in the TAXes. This means that its decay vertex is more distant from the Z axis and its decay products are less likely to be in the CHOD geometric acceptance.

The selection acceptance (Fig. 4.42) is almost flat over the whole coupling range. The increase around $Log(U^2) = -3$ is due to the fact that for that coupling value the HNLs start to be boosted enough so that their decay products hit the CHOD at small distances from its center, ensuring no losses due to different CHOD definitions between the MC simulation and the NA62 reconstruction (any decay product hitting the CHOD at a distance from its center between 1.10 m and 1.3 m is marked as in acceptance at the MC stage but is out of acceptance at the reconstruction stage). For even larger couplings, though, the HNLs are so boosted that their decay vertex is so close to the Z axis that they do not pass the full event selection (as described in Section 4.1.3). The trend of the target-produced sample dominates for large couplings, since highly boosted HNLs produced in the target are more likely to have their decay vertices distant enough from the Z axis that more of them still pass the full event selection, compared to the HNLs produced in the TAXes.

The yield per POT (Fig. 4.43) is the multiplication of the three previous acceptances, where the trend of Fig. 4.40 dominates.

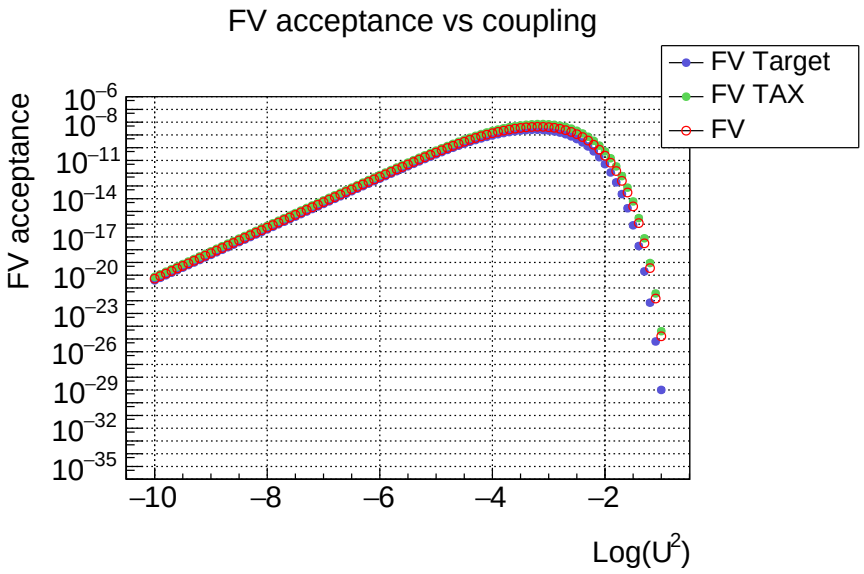

Figure 4.40: *FV acceptance (first component in eq. 4.2) as a function of the coupling, for $m_N = 1\ GeV/c^2$ and for the general model ($U_e^2 : U_\mu^2 : U_\tau^2 = 1{:}1{:}1$), for all events (red dots), events produced in the target (blue dots) and in the TAXes (green dots).*

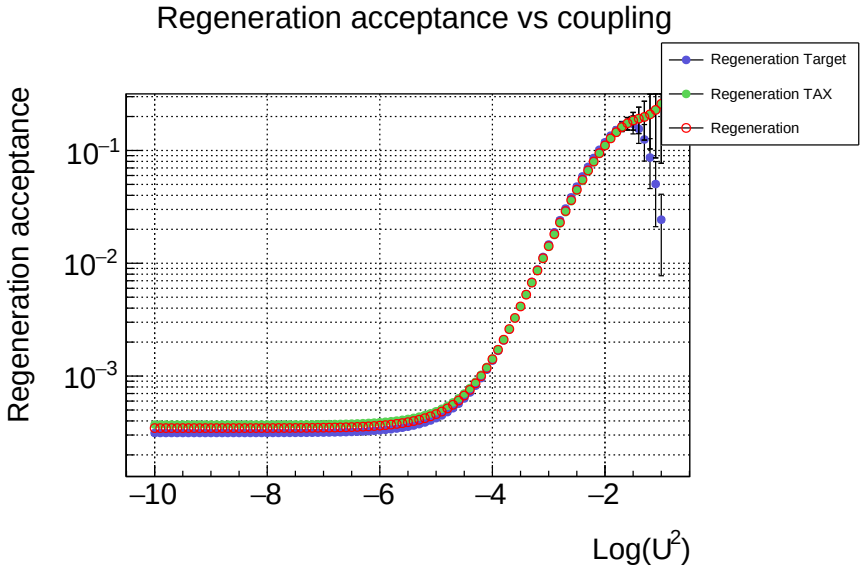

Figure 4.41: *Regeneration acceptance (second component in eq. 4.2) as a function of the coupling, for $m_N = 1\ GeV/c^2$ and for the general model ($U_e^2 : U_\mu^2 : U_\tau^2 = 1{:}1{:}1$), for all events (red dots), events produced in the target (blue dots) and in the TAXes (green dots).*

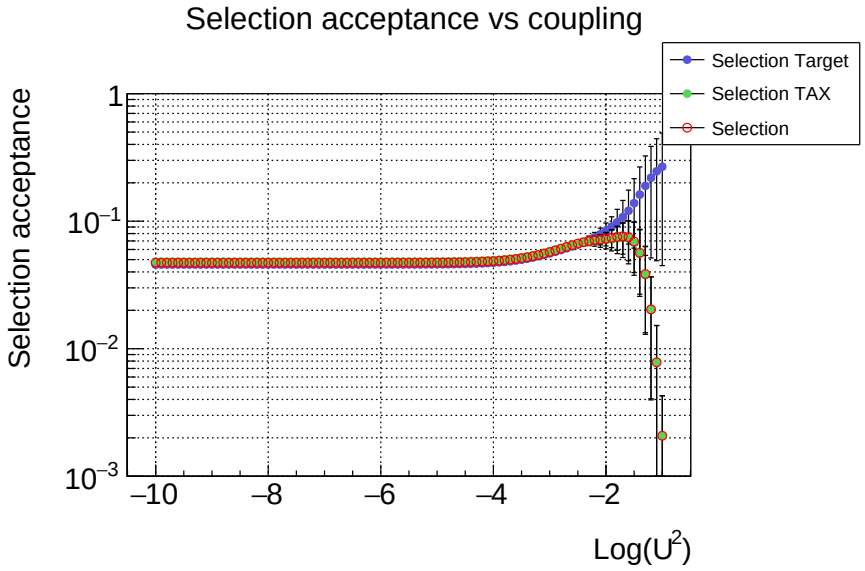

Figure 4.42: *Selection acceptance (third component in eq. 4.2) as a function of the coupling, for $m_N = 1\ GeV/c^2$ and for the general model ($U_e^2 : U_\mu^2 : U_\tau^2 = 1{:}1{:}1$), for all events (red dots), events produced in the target (blue dots) and in the TAXes (green dots).*

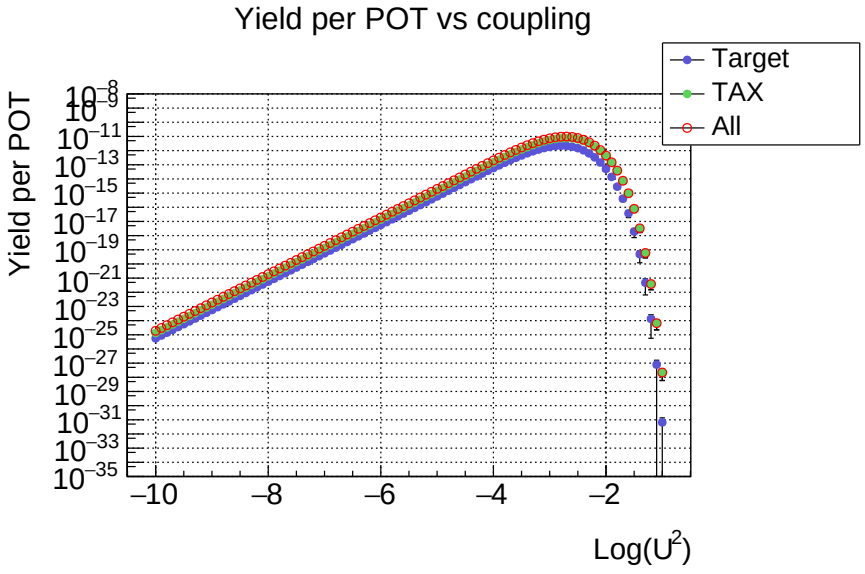

Figure 4.43: *Yield per POT as a function of the coupling, for $m_N = 1\ GeV/c^2$ and for the general model ($U_e^2 : U_\mu^2 : U_\tau^2 = 1{:}1{:}1$), for all events (red dots), events produced in the target (blue dots) and in the TAXes (green dots).*

4.2.2 Expected yield as a function of the mass

The three acceptances and the yield per POT as a function of the HNL mass, for a fixed coupling, are shown in Fig. 4.44 to Fig. 4.47. The yields for target and TAX production are computed for each mass bin and are then normalised to the total number of HNLs in the sample. By doing this, the total yield shown in Fig. 4.47 (red dots) is the sum of the target- and TAX-produced yields (blue and green dots respectively) shown in the same plot. The total acceptances plotted in Fig. 4.44 to Fig. 4.46 (red dots) are the average of the corresponding target- and TAX-related acceptances (blue and green dots).

At $U^2 = 10^{-6}$, the HNLs are likely to reach the FV but not as likely to decay in it. The FV acceptance (Fig. 4.44) increases at large masses, where the HNLs have a smaller Lorentz factor that makes them more likely to decay in the FV. It is worth noticing the discontinuity at $m_N \approx 1.70$ GeV/c^2 and $m_N \approx 1.85$ GeV/c^2 in Fig. 4.45 to Fig. 4.47. This is due to the fact that several production modes reach their kinematic end point around those mass values, as seen in Fig. 1.7, allowing threshold effects to cause non-smooth trends in the acceptance distributions. At $m_N \approx 1.70$ GeV/c^2, the $D \to N\mu$ mode approaches its kinematic end point and therefore the small q-value of the process results in the HNL being generated parallel to the D meson and being highly boosted. This increases the probability of the HNL to decay in the FV, producing a maximization of the acceptance. On the contrary, at $m_N \approx 1.85$ GeV/c^2, two modes approach their kinematic end point: $D_S \to N\mu$ and $D \to Ne$. This gives a more negative contribution to the HNL weight than the previous considered case and therefore the acceptance decreases.

The first increase in the regeneration acceptance (Fig. 4.45) is due to the fact that very light HNLs have their decay vertices too distant from the Z axis for their decay products to be more likely in the CHOD geometric acceptance. Therefore, when the HNL mass increases, fewer regenerations are needed for the decay products to be in the CHOD acceptance. The following decrease in the trend is due to the fact that decay products generated from more massive HNLs have higher transverse momenta and are less likely to be in the CHOD acceptance.

The selection acceptance (Fig. 4.46) is almost flat over the whole mass range, with changes of about 10-20%. Too many factors are involved in producing the plotted trend to understand these increases or losses.

The yield per POT (Fig. 4.47) is the multiplication of the three previous acceptances, where the trend shown in Fig. 4.44 dominates. The sudden changes in trend due to the production-mode kinematic end-points are propagated from each acceptance to the yield.

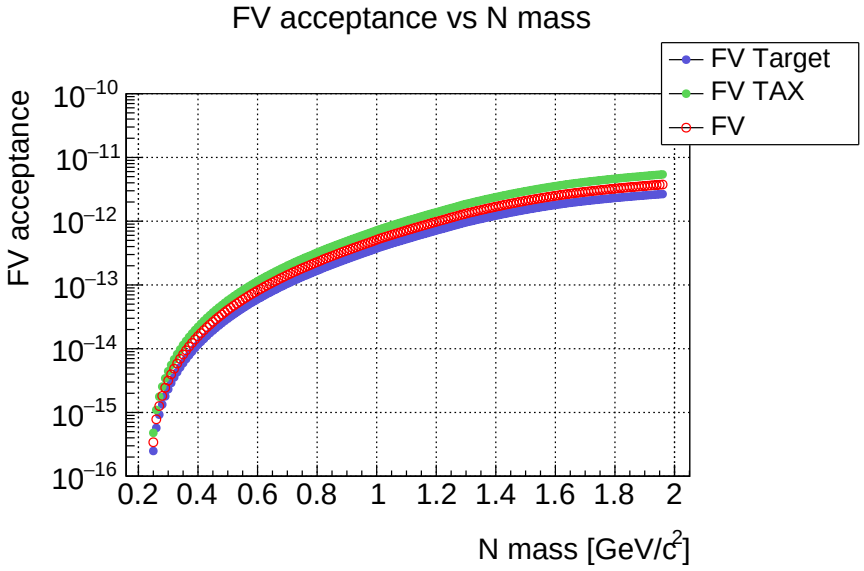

Figure 4.44: *FV acceptance (first component in eq. 4.2) as a function of the HNL mass, for $U^2 = 10^{-6}$ and for the general model ($U_e^2 : U_\mu^2 : U_\tau^2$ = 1:1:1), for all events (red dots), events produced in the target (blue dots) and in the TAXes (green dots).*

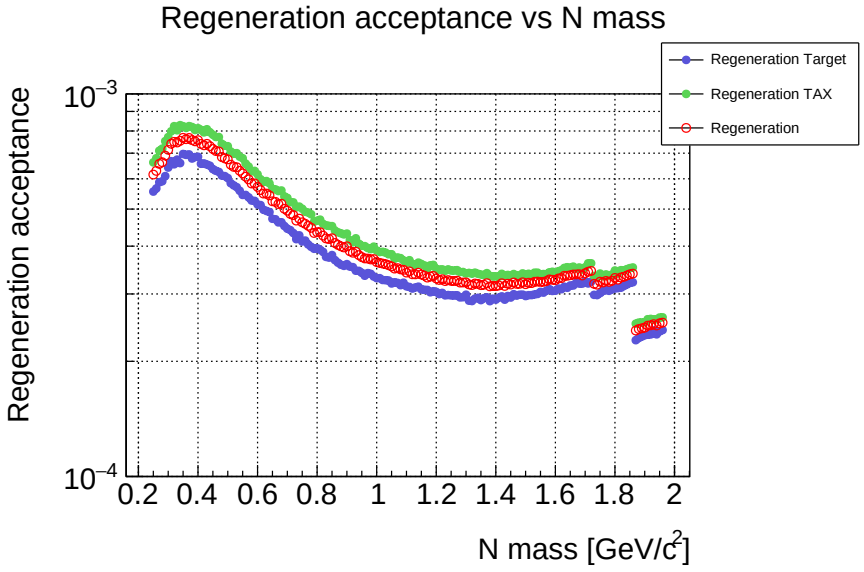

Figure 4.45: *Regeneration acceptance (second component in eq. 4.2) as a function of the HNL mass, for $U^2 = 10^{-6}$ and for the general model ($U_e^2 : U_\mu^2 : U_\tau^2$ = 1:1:1), for all events (red dots), events produced in the target (blue dots) and in the TAXes (green dots).*

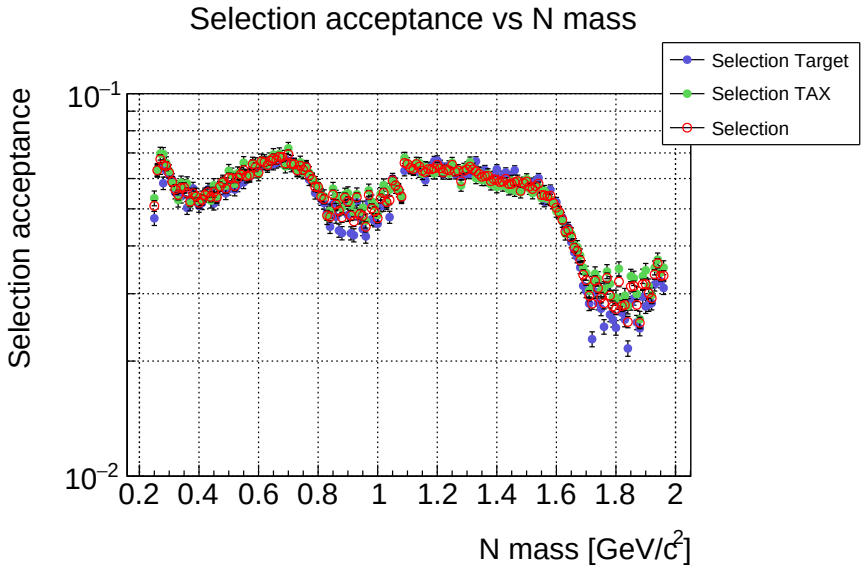

Figure 4.46: *Selection acceptance (third component in eq. 4.2) as a function of the HNL mass, for $U^2 = 10^{-6}$ and for the general model ($U_e^2 : U_\mu^2 : U_\tau^2 = 1{:}1{:}1$), for all events (red dots), events produced in the target (blue dots) and in the TAXes (green dots).*

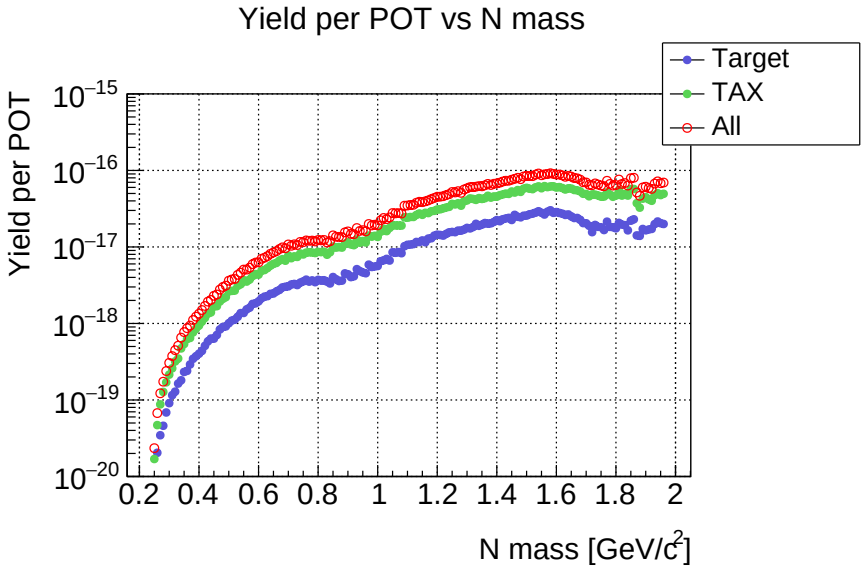

Figure 4.47: *Yield per POT as a function of the HNL mass, for $U^2 = 10^{-6}$ and for the general model ($U_e^2 : U_\mu^2 : U_\tau^2 = 1{:}1{:}1$), for all events (red dots), events produced in the target (blue dots) and in the TAXes (green dots).*

4.2.3 Expected yield as a function of the momentum

The three acceptances and the yield per POT as a function of the HNL momentum, for a fixed coupling and mass, are plotted in Fig. 4.48 to Fig. 4.51. The yield shown in Fig. 4.51 is computed for each momentum bin and is then normalised to the total number of HNLs in the sample. This means that effectively the quantity plotted in Fig. 4.51 is the fractional contribution to the yield for each momentum bin. Thus, the integrated yield of Fig. 4.51 is equal to the yield value shown in Fig. 4.43 for $Log(U^2) = -6$ and the yield value shown in Fig. 4.47 for $m_N = 1$ GeV/c^2. The same consideration applies to the three acceptances plotted in Fig. 4.48 to Fig. 4.50, which are normalised bin by bin to the total number of HNLs in the sample. Therefore they are fractional contributions to the acceptances for each momentum bin and are additive.

The FV acceptance (Fig. 4.48) decreases for large momenta since, for a fixed coupling and therefore lifetime, HNLs with greater momenta are more likely to travel beyond the end of the FV without decaying in it.

The regeneration acceptance (Fig. 4.49) first increases, due to the fact that decay products generated from low-momentum HNLs have large transverse momenta and are less likely to reach the CHOD geometric acceptance. The trend then decreases for larger HNL momenta. At $U^2 = 10^{-6}$, the HNLs that reach the FV decay at the beginning of it. This means that, despite their small transverse momenta, their decay products reach the CHOD plane at distances larger than 1.3 m and are therefore outside the detector acceptance.

The selection acceptance (Fig. 4.50) first increases, due to the fact that, at low momentum, losses are present when decay products hit the CHOD plane at distances from its center between 1.10 m and 1.3 m (the same considerations drawn in Section 4.2.1 concerning Fig. 4.42). The following decrease in the trend is due to the fact that high-momentum HNLs have their decay vertices too close to the Z axis to pass the full event selection (as described in Section 4.1.3).

The yield per POT (Fig. 4.51) is the multiplication of the three previous acceptances.

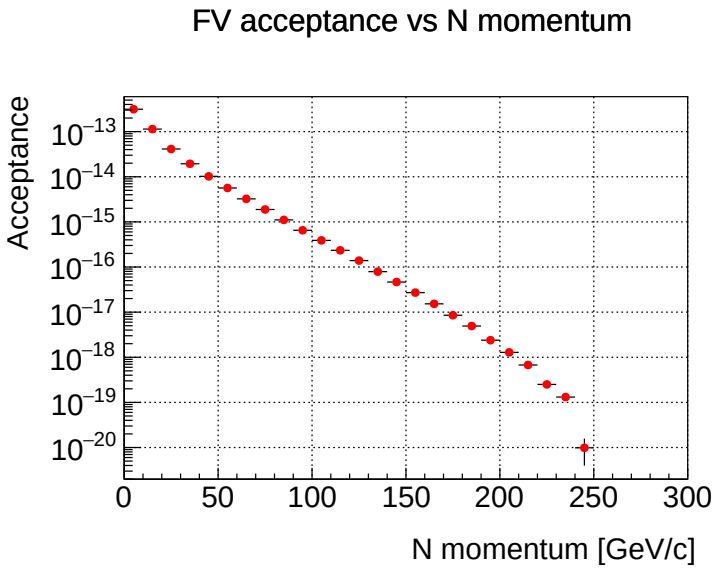

Figure 4.48: *FV acceptance (first component in eq. 4.2) as a function of the HNL momentum, for $m_N = 1$ GeV/c^2, $U^2 = 10^{-6}$ and for the general model ($U_e^2 : U_\mu^2 : U_\tau^2 =$ 1:1:1), for both target- and TAX-produced events.*

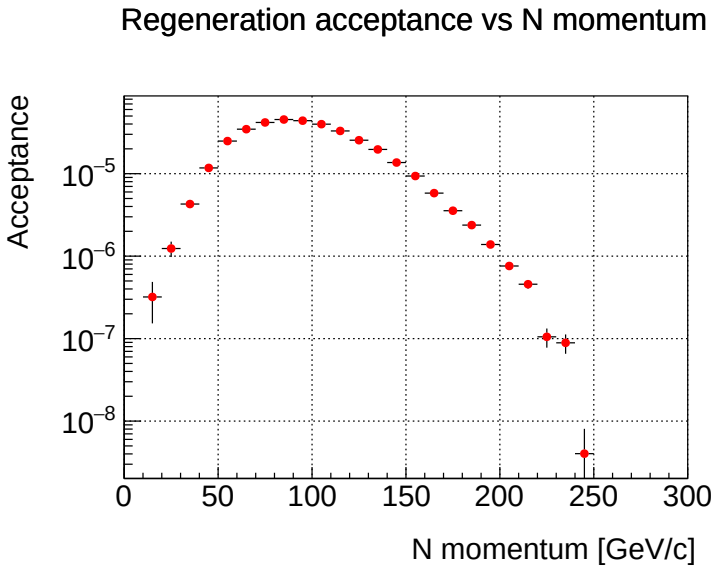

Figure 4.49: *Regeneration acceptance (second component in eq. 4.2) as a function of the HNL momentum, for $m_N = 1$ GeV/c^2, $U^2 = 10^{-6}$ and for the general model ($U_e^2 : U_\mu^2 : U_\tau^2 =$ 1:1:1), for both target- and TAX-produced events.*

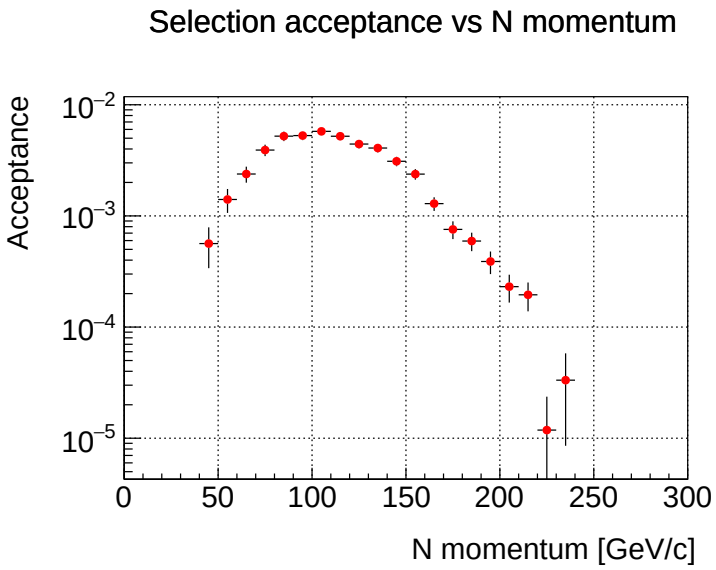

Figure 4.50: *Selection acceptance (third component in eq. 4.2) as a function of the HNL momentum, for $m_N = 1$ GeV/c^2, $U^2 = 10^{-6}$ and for the general model ($U_e^2 : U_\mu^2 : U_\tau^2 =$ 1:1:1), for both target- and TAX-produced events.*

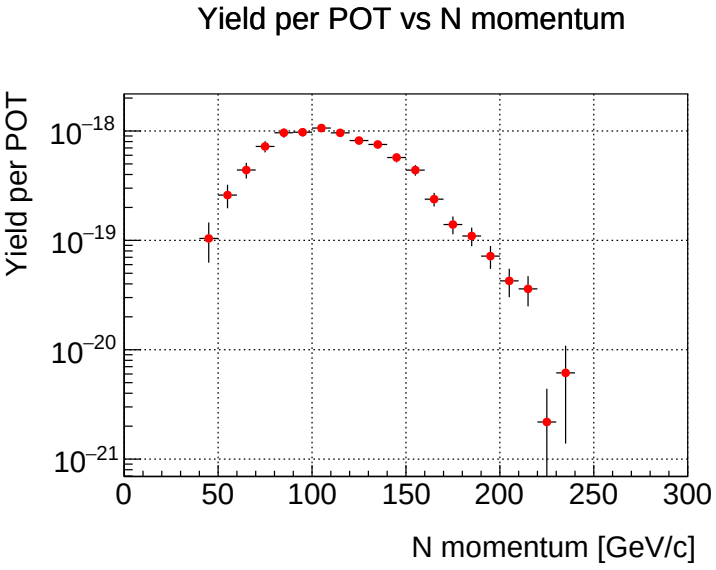

Figure 4.51: *Yield per POT as a function of the HNL momentum, for $m_N = 1$ GeV/c^2, $U^2 = 10^{-6}$ and for the general model ($U_e^2 : U_\mu^2 : U_\tau^2 =$ 1:1:1), for both target- and TAX-produced events.*

4.3 Sensitivity curves

The expected yield is studied as a function of both the coupling and the HNL mass. It is then multiplied by the number of POT to be collected to be competitive with previous experimental results. This is expected to be equal to 10^{18} POT during the beam-dump operation mode of 2021-2023. The expected sensitivity is then computed: the curve is made of all the HNL mass-coupling value pairs for which $Y_{POT} \cdot 10^{18} = 2.3$. This value corresponds to the 90% Confidence Level (CL) in the hypothesis of zero background, which has been assumed when designing the event selection described in Section 4.1. Background evaluation studies are presented in Chapter 5.

The 90% CL contour for the expected sensitivity is shown for the general and the tau-dominant models (Fig. 4.52 and Fig. 4.53). Expected sensitivity curves obtained within other relevant theoretical scenarios can be found in Appendix E.

The curves presented here cannot be directly compared or superimposed to the ones from the PBC report and displayed in Fig. 1.12, since in the latter case the HNL coupling to muons is removed. For the decay search discussed in this thesis, having a non-null U_μ^2 is mandatory to be sensitive to pion-muon final states. Moreover, if the coupling to muon were to be switched off and only U_τ^2 remained, the only enabled decay channels for HNLs with mass below the D meson one would be open channels involving SM neutrinos, which would not be fully reconstructible and whose phasespace would be limited. NA62 would not therefore be competitive in the $U_e^2 : U_\mu^2 : U_\tau^2 = 0{:}0{:}1$ scenario with $m_N < m_{D_i}$ ($D_i = D, D^0, D_S$).

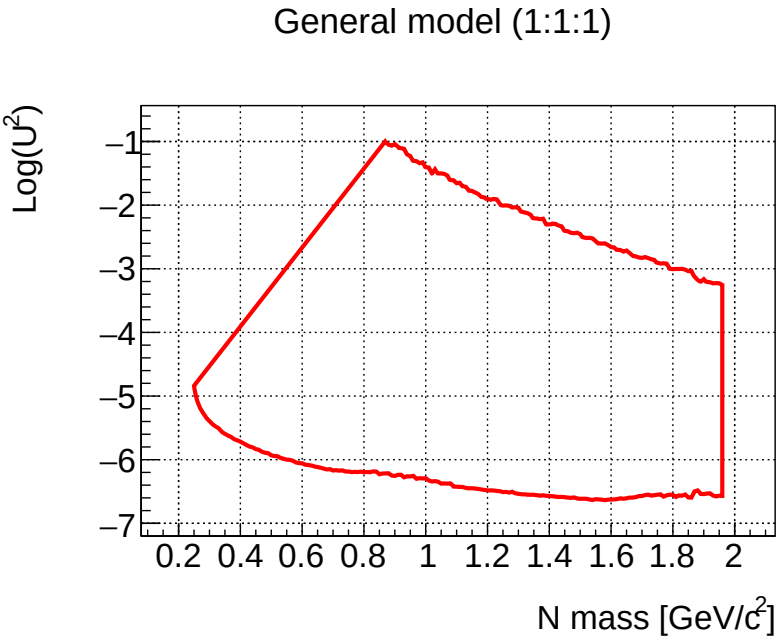

Figure 4.52: *NA62 expected sensitivity in the plane coupling vs HNL mass, at 90% CL, for the general model ($U_e^2 : U_\mu^2 : U_\tau^2 = 1{:}1{:}1$).*

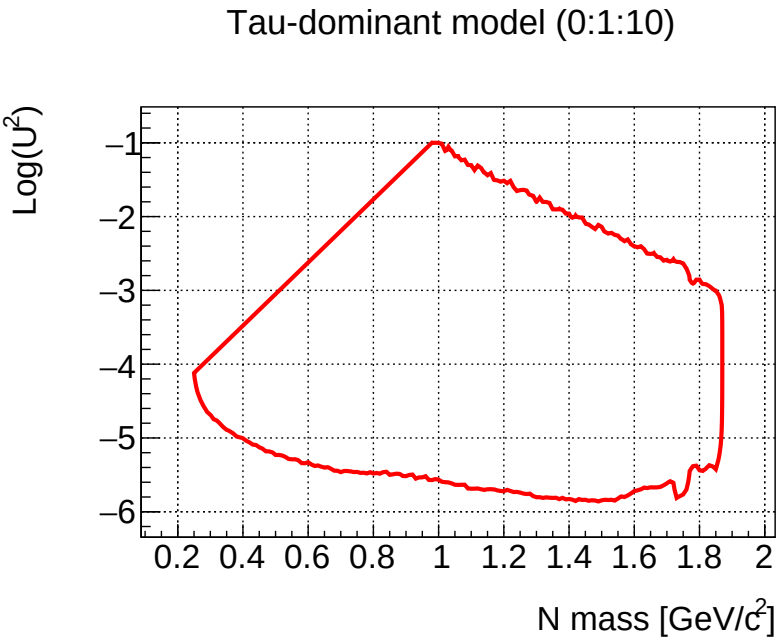

Figure 4.53: *NA62 expected sensitivity in the plane coupling vs HNL mass, at 90% CL, for the tau-dominant model ($U_e^2 : U_\mu^2 : U_\tau^2 = 0{:}1{:}10$).*

Chapter 5

Background evaluation

5.1 Data set collected in kaon mode

The data set collected during 2016-2018 for $N \to \pi\mu$ decay searches, with the "muon exotics" trigger described in Section 2.5.4, has been analysed to perform a data-driven evaluation of the main background sources present in kaon mode. The whole data set corresponds to $2.4 \cdot 10^{17}$ POT, whereas only a subsample already reconstructed by the offline NA62 framework was available for analysis at the time of these studies. The considered subset corresponds to $1 \cdot 10^{17}$ POT. The number of POT is computed as following:

$$N_{POT} = \frac{F_{POT-K} \cdot N_{K3\pi}}{BR(K^+ \to \pi^+\pi^+\pi^-) \cdot A_{K3\pi} \cdot \epsilon^K_{dec} \cdot d}. \tag{5.1}$$

Here, $F_{POT-K} = \frac{1.1 \cdot 10^{12}}{45.0 \cdot 10^6} = 2.44 \cdot 10^4$ is the conversion factor determined by instantaneous POT rate per spill divided by number of positive kaons entering the decay volume; $N_{K3\pi}$ is the number of fully-reconstructed $K^+ \to \pi^+\pi^+\pi^-$ decays occurred in the FV in the analysed data sample, computed within the NA62 offline framework and used as normalisation channel, and $BR(K^+ \to \pi^+\pi^+\pi^-) = 0.05583$ [28] is the Branching Ratio of the $K^+ \to \pi^+\pi^+\pi^-$ decay. The quantity $A_{K3\pi} \approx 0.15$ is the acceptance of the $K^+ \to \pi^+\pi^+\pi^-$ event selection (estimated from MC simulations within the collaboration), while $\epsilon^K_{dec} = 0.125$ is the probability for a kaon to decay in the FV. The last factor, d, is the downscaling factor with which the "muon exotics" trigger has been collected, due to limited bandwidth for data-taking: for example, a downscaling of 10 means that only one triggered event out of 10 has been written on disk. The downscaling for the "muon exotics" trigger has varied throughout the data-taking, from a minimum of 1 to a maximum of 20. Therefore, the POT computation of eq. 5.1 has been performed run by run (a run being a data subsample collected in uniform data-taking conditions and downscaling) and

the results have been added to calculate the total number of POT to which the analysed subsample for HNL decay searches corresponds to.

5.2 Data-driven method for background evaluation

A data-driven method for background evaluation is a procedure performed to compute the expected number of background events to a certain process, without the use of MC simulations, by studying the background source present in the collected data sample. This procedure consists of defining a region in one or more variables, such that the distribution of signal events in that region is maximised. This region is then "blinded" when analysing the collected data sample, and no information can be retrieved on the background distribution in that region. Each source can be studied using variables that discriminate the signal against the background, and defining subregions in the variable distributions, the so-called "sidebands", which are dominated by the latter. By studying these distributions, one can extrapolate the number of expected background events in the blinded region. In searches that aim at discovering new particles, a hypothesis on the mass of the new particle is made and the number of expected background events in the blinded region is computed for each mass hypothesis. The blinded region can then be "unblinded" at the completion of the analysis, to count the effective number of events inside it, as a function of the particle mass hypothesis, and set upper limits for this search. The last two steps are not part of the work discussed in this thesis. In fact, although the signal selection is considered optimised and frozen, few actions are missing before completing this search:

- computing the corresponding expected upper limit in no-signal hypothesis as a function of the HNL mass and coupling;
- computing the trigger and selection efficiencies for this study;
- unblinding the blinded region and counting the number of events present in it;
- setting upper limits to the NA62 sensitivity to $N \to \pi\mu$ events.

5.3 Blinded region for background evaluation

The variables chosen to study the distribution of signal events for $N \to \pi\mu$ searches have been defined in Section 4.1.4 and shown in Fig. 4.39. The region to

be blinded during the presented data-driven background studies is defined within 0 mm $\leq CDA \leq$ 60 mm and -15 m $\leq Z_{CDA} \leq$ 40 m. Here, CDA is the Closest Distance of Approach (CDA) between the HNL trajectory (computed from the two downstream tracks measured by the Straw spectrometer) and the proton trajectory, assumed as the line connecting the average of the HNL production point in the target to the one in the TAXes (computed through the MC simulation); whereas Z_{CDA} is the Z coordinate of the same quantity. The choice of defining a wide blinded region is motivated by the fact that, at a later stage of the analysis that is not included in this thesis, multiple signal regions and control regions could be selected within the broad blinded region used for the studies detailed in this Chapter. At that stage, one could decide to keep a wide signal region, unique for both target and TAX production, or choose to separately study the two by selecting smaller signal regions around the two production points, while exploiting the areas around them for control purposes. Several signal regions could also be studied and defined according to different HNL mass hypotheses, with negligible losses in signal acceptance.

It needs to be noted that the data-driven background evaluation for this decay search is performed separately for $N \to \pi^+\mu^-$ and $N \to \pi^-\mu^+$ samples, since the two receive different background contributions. This is due to the fact that the great majority of particles decaying in the NA62 fiducial volume are positive, and the experiment is not optimised to detect negative particles.

Fig. 5.1 shows the distribution of $N \to \pi^+\mu^-$ MC signal events in terms of CDA and Z coordinate of the CDA between the HNL trajectory and the proton line, while in Fig. 5.2 the same quantities are plotted in the $N \to \pi^-\mu^+$ case.

5.4 Invariant mass resolution for Monte Carlo signals

The evaluation of the expected number of background events as a function of the HNL mass hypothesis makes use of the two-track reconstructed invariant mass, so the mass resolution for MC signal events is studied as a function of the true HNL mass, in the range from 0.25 GeV/c^2 to 1.96 GeV/c^2 and in steps of 10 MeV/c^2. The chosen step value is small enough to ensure good granularity when producing the acceptance and yield plots as a function of the HNL mass (Section 4.2.2), and the expected sensitivity curves (Section 4.3).

The plot in Fig. 5.3 shows the distribution of the two-track reconstructed invariant mass as a function of the true HNL mass, for all MC signal events. As seen in this plot, the mass resolution increases at larger masses.

To study the HNL mass resolution, a distribution of the reconstructed invariant

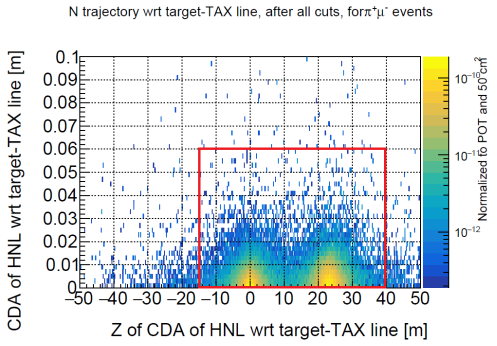

Figure 5.1: *Signal region for $N \to \pi^+\mu^-$ events: CDA vs Z coordinate of the CDA of the HNL trajectory with respect to the proton line. This plot refers to two-track reconstructed MC events produced both in the target and the TAXes, after all selection cuts, generated from all HNL masses, $U^2 = 10^{-6}$ and for the general model (U_e^2 : U_μ^2 : U_τ^2 = 1:1:1). The blinded region is visible in red.*

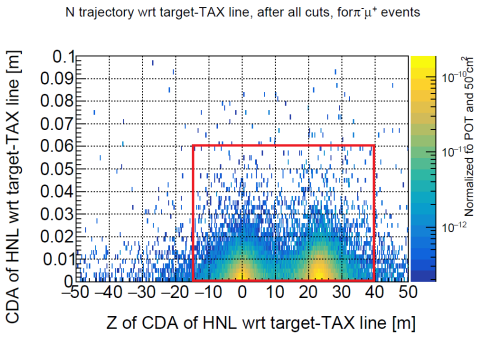

Figure 5.2: *Signal region for $N \to \pi^-\mu^+$ events: CDA vs Z coordinate of the CDA of the HNL trajectory with respect to the proton line. This plot refers to two-track reconstructed MC events produced both in the target and the TAXes, after all selection cuts, generated from all HNL masses, $U^2 = 10^{-6}$ and for the general model (U_e^2 : U_μ^2 : U_τ^2 = 1:1:1). The blinded region is visible in red.*

mass of all events corresponding to a certain value of the true MC mass is plotted and fitted with a Gaussian function. This is repeated for all MC true mass values; the RMS of each fitted subsample is then plotted as a function of the corresponding HNL true mass (Fig. 5.4). The distribution shown in Fig. 5.4 is fitted with a linear function, and the parameters of the fit are used to compute the mass resolution of each HNL mass hypothesis considered to evaluate the expected number of background events. As seen in Fig. 5.4, the larger the reconstructed invariant mass, the more the mass resolution is distant from the fit. This is due to lower statistics, caused by the fact that fewer events pass the full selection. This could be solved by producing more MC events at larger masses, which could not be done due to time constraints. The goodness of the fit has been crosschecked by studying the distribution of residuals as a function of the fitted values, and confirming that there is no correlation between the two.

The reason why the mass values shown in Fig. 5.3 and Fig. 5.4 start from 0.5 GeV/c^2 is related to the background evaluation procedure and it is explained in Section 5.5.1.

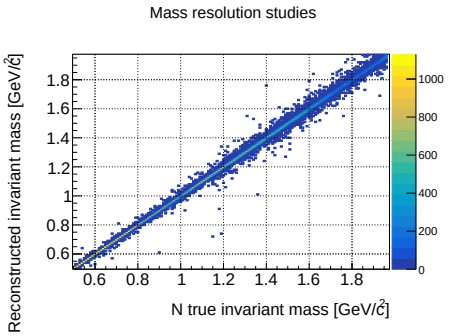

Figure 5.3: *Two-track reconstructed invariant mass as a function of the true HNL mass, for all MC signal events.*

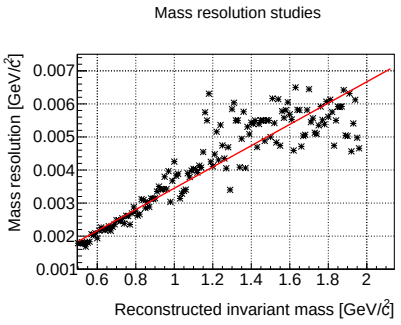

Figure 5.4: *Mass resolution as a function of the true HNL mass (from the MC simulation), for all MC signal events, fitted with a linear function.*

5.5 Main background sources

Three processes give the most relevant background contributions to the HNL decay searches detailed in this thesis, mimicking the $N \to \pi\mu$ signal. A detailed description of all three, together with their evaluation procedures, is given in the following, for the $N \to \pi^+\mu^-$ data sample. The $N \to \pi^-\mu^+$ sample has not been treated within this thesis.

5.5.1 Kaon-induced background

One of the main background sources to $N \to \pi\mu$ searches is the one originating from beam $K^+ \to \pi^+\pi^+\pi^-$ decays. For the $N \to \pi^+\mu^-$ sample, this occurs when one negative pion decays in flight via $\pi^- \to \mu^-\nu_\mu$ and one positive pion goes undetected, whereas, in the $N \to \pi^-\mu^+$ case, the background sources is due to one positive pion decaying via $\pi^+ \to \mu^+\bar{\nu_\mu}$ and one positive pion going undetected. The result, in both cases, is that $\pi\mu$ pairs are present in the final state, with the two tracks being in time because they come from the same decay.

The kaon-induced background becomes negligible when the HNL masses considered are larger than the kaon mass, about 0.5 GeV/c^2. Restricting the HNL mass range above this value has the advantage to eliminate this background source without impacting the NA62 sensitivity to this decay search, as shown in Fig. 4.52 and Fig. 4.53. The expected sensitivity curves presented in Chapter 4 show the HNL mass region below the kaon mass as well, for completeness.

5.5.2 Combinatorial background

The combinatorial background to $N \to \pi\mu$ searches consists of two opposite-charged tracks, identified as a pion and a muon, uncorrelated in time. In the case of the $N \to \pi^+\mu^-$ sample, the positive pions either come from the beam itself or originate from beam $K^+ \to \pi^+\pi^0$ decays, while the negative muons come from the so-called "beam muon halo". This is a halo of particles that contains positive muons, either present in the beam itself or generated in beam kaon and pion decays, and negative muons originating in the showers produced by the interaction between the SPS primary proton beam and the T10 target.

The combinatorial background to $N \to \pi^-\mu^+$ events originates from beam $K^+ \to \pi^+\pi^+\pi^-$ decays (negative pions), while positive muons are generated in beam kaon and pion decays.

Sideband definition

To evaluate the combinatorial background, where the two tracks are uncorrelated in time, two sidebands have been chosen in the time difference distribution of the two tracks, where the track time measurement is provided by the CHOD.

Due to the nature of the background source, the time distribution of the two-track difference is expected to be uniform, since the beam intensity is stable throughout a single spill.

Fig. 5.5 shows the two-track time-difference distribution for all MC signal events outside the blinded region defined in Section 5.3, for the $N \to \pi^+\mu^-$ sample. In Fig. 5.6, the same quantity is plotted for all data events outside the blinded region.

As seen in Fig. 5.6, a peak is present between -2 ns and 2 ns: these are time-correlated tracks and, therefore, they do not constitute the combinatorial background. The distribution in the range [-4, -2] ns and [2, 4] ns is uniform, thus it is expected to be populated by this background, with the signal being negligible. The two peaks around -6 ns and 6 ns are due to time cuts at the trigger level. The fact that no events are present below -7 ns and above 7 ns is due to the presence of time cuts in the full event selection.

The sidebands are defined between -4 ns and -2 ns, and between 2 ns and 4 ns. The data distribution in the sidebands is assumed flat and is propagated as such in the blinded region. The total width of the two sidebands combined is equal to the width of the region where the MC signal peaks. Since the distribution difference between the peaks around ± 6 ns and the sidebands is approximately 50% (as seen in Fig. 5.6), a conservative systematic error will be associated with the expected number of combinatorial background events computed in the following paragraphs.

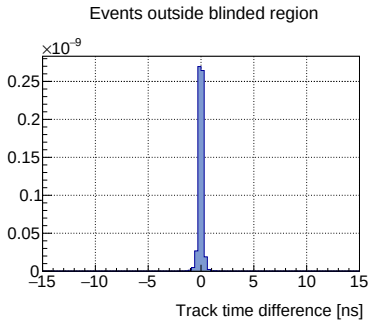

Figure 5.5: *Distribution of the time difference of the two tracks, as given by the CHOD, for MC signal events outside the blinded region, at different masses, $U^2 = 10^{-6}$ and for the general model ($U_e^2 : U_\mu^2 : U_\tau^2 = 1{:}1{:}1$), in the $N \to \pi^+\mu^-$ case. Each event is weighted for the quantity defined in Section 3.8.*

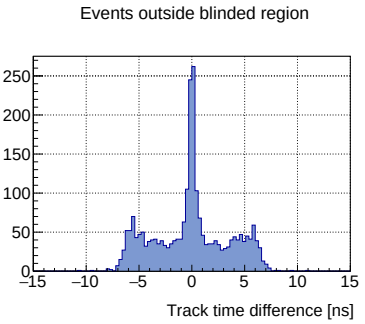

Figure 5.6: *Distribution of the time difference of the two tracks, as given by the CHOD, for data outside the blinded region, in the $N \to \pi^+\mu^-$ case.*

Contribution from positive beam pions

The combinatorial background component to $N \to \pi^+\mu^-$ events produced by positive beam pions and negative halo muons can be eliminated by studying the momentum distribution of the downstream tracks, for all events in the combinatorial sidebands. The particle identification for both tracks is provided by the MUV3, while the electric charge is measured by the Straw spectrometer. The momentum distribution for positive pions is shown in Fig. 5.7 for the MC signal sample, and in Fig. 5.8 for the data. The negative muon momentum distribution is plotted in Fig. 5.9 for the MC signal sample and in Fig. 5.10 for the data.

Moreover, the transverse position at the GTK3 station ($Z = 102.4$ m) is plotted in Fig. 5.11 (Fig. 5.12) for all positive pions with momentum between 70 GeV/c and 80 GeV/c, for all MC signal (data) events within the combinatorial sidebands. The shape of the distribution shown in Fig. 5.12 indicates that all these tracks cross the GTK3 station and, therefore, suggests that they belong to the beam. This does not happen in the case of MC signal events (Fig. 5.11), since the HNLs for these decay searches are produced at the target or at the TAXes and do not cross the GTK3 station.

The combinatorial background component induced from positive beam pions to the $N \to \pi^+\mu^-$ events is then eliminated from the sample, by adding a cut that rejects all events with positive pions in the [70, 80] GeV/c momentum range and whose X, Y coordinates at the GTK3 plane lay within a rectangle of 80×60 mm^2 centred at $(X, Y) = (0, 0)$. This cut is performed at an affordable cost in terms of signal acceptance.

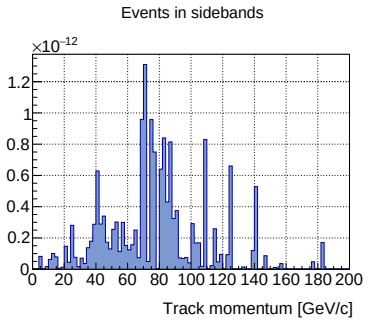

Figure 5.7: *Momentum distribution for positive downstream tracks not associated with the MUV3, in the combinatorial sidebands, for MC signal events at different masses, $U^2 = 10^{-6}$ and for the general model ($U_e^2 : U_\mu^2 : U_\tau^2 = 1:1:1$), in the $N \to \pi^+\mu^-$ case. Each event is weighted for the quantity defined in Section 3.8. No peak at 75 GeV/c is observed.*

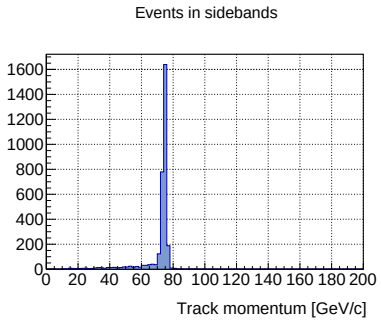

Figure 5.8: *Momentum distribution for positive downstream tracks not associated with the MUV3, for data events in the combinatorial sidebands, in the $N \to \pi^+\mu^-$ case. The peak at 75 GeV/c indicates the beam pion component to this background source.*

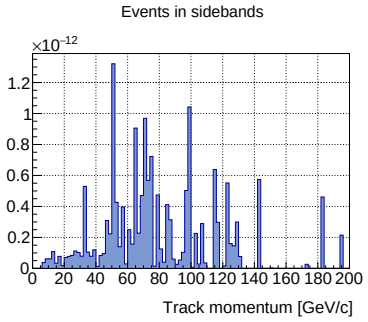

Figure 5.9: *Momentum distribution for negative downstream tracks associated with the MUV3, in the combinatorial sidebands, for MC signal events at different masses, $U^2 = 10^{-6}$ and for the general model ($U_e^2 : U_\mu^2 : U_\tau^2 = 1:1:1$), in the $N \to \pi^+\mu^-$ case. Each event is weighted for the quantity defined in Section 3.8.*

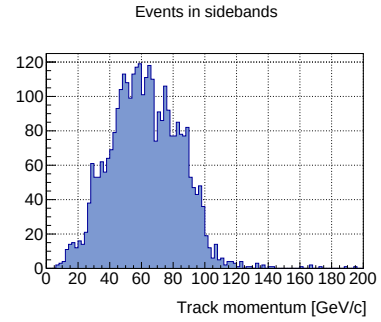

Figure 5.10: *Momentum distribution for negative downstream tracks associated with the MUV3, for data events in the combinatorial sidebands, in the $N \to \pi^+\mu^-$ case.*

From this point on, the plots shown and the studies detailed in the following assume that all data events contributing to this component are rejected.

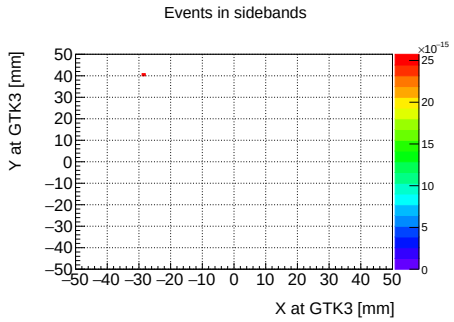

Figure 5.11: *Tranverse position at the GTK3 station for positive downstream tracks not associated with the MUV3 and with momentum between 70 GeV/c and 80 GeV/c, in the combinatorial sidebands, for MC signal events at different masses, U^2 =10^{-6} and for the general model (U_e^2 : $U_\mu^2 : U_\tau^2$ = 1:1:1), in the $N \to \pi^+\mu^-$ case. Each event is weighted for the quantity defined in Section 3.8. The MC signal events do not come from the beam and, therefore, do not cross the GTK3 station.*

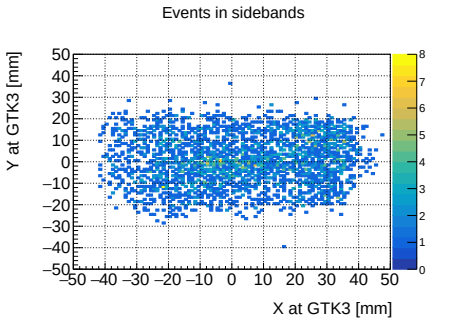

Figure 5.12: *Tranverse position at the GTK3 station for positive downstream tracks not associated with the MUV3 and with momentum between 70 GeV/c and 80 GeV/c, for data events in the combinatorial sidebands, in the $N \to \pi^+\mu^-$ case. The distribution shape suggests that these tracks are positive beam pions that cross the GTK3 station.*

Reconstructed invariant mass distribution

After rejecting all events presenting the combinatorial background component induced from positive beam pions, the distribution of the two-track reconstructed invariant mass can be studied for all events inside the combinatorial sidebands and the blinded region. This is done in order to evaluate the expected number of combinatorial background events for each HNL mass hypothesis.

Fig. 5.13 shows the two-track reconstructed invariant mass distribution for all data events inside the combinatorial sidebands and the blinded region, for the $N \to \pi^+\mu^-$ sample, while the same distribution is plotted in Fig. 5.14 for all events inside the sidebands.

The comparison of the two plots suggests that the distribution shown in Fig. 5.13 is likely to have been drawn from the one plotted in Fig. 5.14.

The number of events in the sidebands and the blinded region is computed from

$$N_{SB} : N_S = N_{SB+BR} : N_{S+BR}, \tag{5.2}$$

where N_{SB} is the number of events in the sidebands (in the ranges [-4, -2] ns and [2, 4] ns), N_S is the number of events in the signal region (between -2 ns and 2 ns), N_{SB+BR} is the number of events in the sidebands and inside the blinded region (as shown in Fig. 5.13), and N_{S+BR} is the number of events in the signal region and

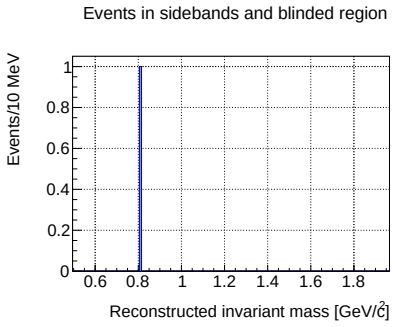

Figure 5.13: *Two-track reconstructed invariant mass distribution for data events in the combinatorial sidebands and in the blinded region, in the $N \to \pi^+\mu^-$ case.*

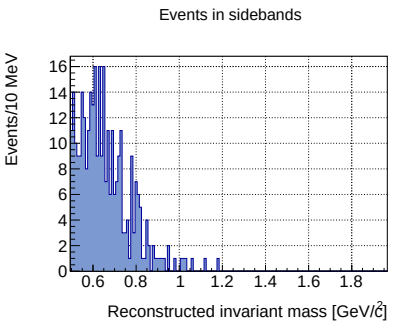

Figure 5.14: *Two-track reconstructed invariant mass distribution for data events in the combinatorial sidebands, in the $N \to \pi^+\mu^-$ case.*

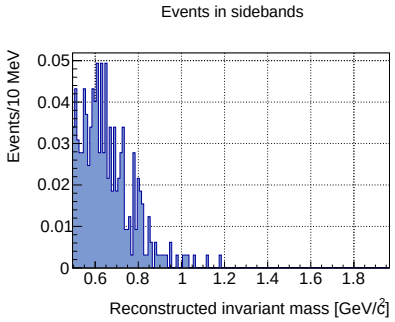

Figure 5.15: *Two-track reconstructed invariant mass distribution for data events in the combinatorial sidebands, rescaled to the number of events in Fig. 5.13, in the $N \to \pi^+\mu^-$ case.*

inside the blinded region.

Since the sideband width is equal to the signal region width, and the data distribution can be assumed flat at first order in the sidebands (as plotted in Fig. 5.6), it follows that

$$N_{S+BR} = \frac{N_{SB+BR} \cdot N_S}{N_{SB}} = N_{SB+BR}. \tag{5.3}$$

The distribution in Fig. 5.14 is therefore rescaled to N_{SB+BR} (since $\frac{N_S}{N_{SB}} = 1$), in such a way that its integral in equal to the one in Fig. 5.13. Fig. 5.15 shows the reconstructed invariant mass distribution for data events in the combinatorial sidebands, after rescaling it to the number of events in Fig. 5.13.

Evaluation of the expected number of background events

A scan on the HNL mass hypothesis is performed on the distribution plotted in Fig. 5.15, starting from $m_N = 0.5$ GeV/c^2, in steps equal to the smallest value of the true mass resolution found in the plot in Fig. 5.4. For each HNL mass hypothesis, its corresponding mass resolution (σ) is then computed via the fit described in Section 5.4. A 1σ- or 2σ-wide window is then opened, centred on the considered HNL mass hypothesis, and the expected number of background events for each mass hypothesis is calculated by computing the integral of the bins included in the mass window, and considering that the bins on its boundaries are counted accordingly to the bin fraction included in the window.

Background evaluations with both a 1σ- or 2σ-wide mass window are provided, since the limits that are put on the HNL coupling as a function of the HNL mass may be more or less stringent, according to the mass window width and the method used for estimating the background (either data driven or from MC simulations). Results of background evaluation for both widths are presented in this thesis, to allow for future comparisons when upper limits are set for this search (which is not part of the work discussed in this thesis).

The expected number of combinatorial background events for each HNL mass hypothesis, for the $N \to \pi^+\mu^-$ sample, is plotted in Fig. 5.16 (Fig. 5.17) for a 1σ-wide (2σ-wide) mass window.

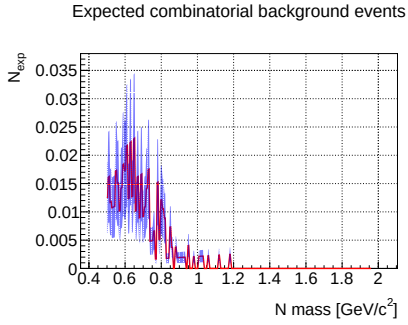

Figure 5.16: *Number of expected combinatorial background events for each HNL mass hypothesis, for a 1σ-wide mass window, in the $N \to \pi^+\mu^-$ case. The blue area indicates a 50% conservative systematic error assigned to the background evaluation and due to the assumption of uniformity for the event distribution in the combinatorial sidebands.*

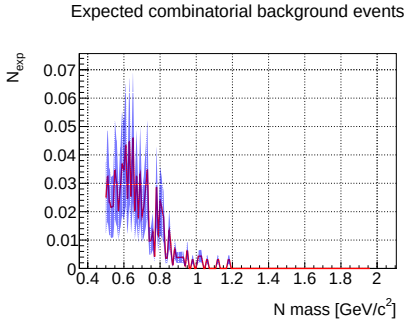

Figure 5.17: *Number of expected combinatorial background events for each HNL mass hypothesis, for a 2σ-wide mass window, in the $N \to \pi^+\mu^-$ case. The blue area indicates a 50% conservative systematic error assigned to the background evaluation and due to the assumption of uniformity for the event distribution in the combinatorial sidebands.*

5.5.3 Muon-induced background

The muon-induced background comes from beam and halo muons interacting with the collimators and magnets along the beamline, upstream the fiducial volume, and generating showers of particles. Pairs of in-time ee, $e\mu$ and $\mu\mu$ of zero total charge are produced in these showers and can be misidentified as signal pion-muon pairs.

Sideband definition

To evaluate the muon-induced background, a sideband has been chosen in the distribution of the Z coordinate of the two-track vertex, for those events whose two-track time difference (as measured by the CHOD) is between -2 ns and 2 ns. The choice of this time constraint comes from the fact that events outside this time window are of combinatorial origin, and including them in the muon-induced background evaluation would produce a double counting in the estimate. The combinatorial background source is studied in Section 5.5.2.

The sideband is defined between 102.4 m and 120 m. This choice is motivated by the fact that the number of MC signal events in it is negligible with respect to the one in the complementary region, namely the FV (between 120 m and 180 m), as seen in Fig. 5.18, whereas the number of data events in this region is non negligible and the muon-induce background is expected to populate it (Fig. 5.19).

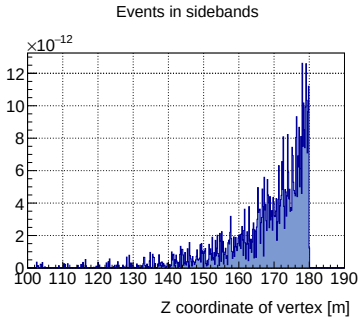

Figure 5.18: *Distribution of the Z coordinate of the two-track vertex, for data outside the blinded region and with two-track time difference (as given by the CHOD) between -2 ns and 2 ns, for all MC signal events outside the blinded region, at different masses, U^2 =10^{-6} and for the general model ($U_e^2 : U_\mu^2 : U_\tau^2$ = 1:1:1), in the $N \to \pi^+\mu^-$ case. Each event is weighted for the quantity defined in Section 3.8.*

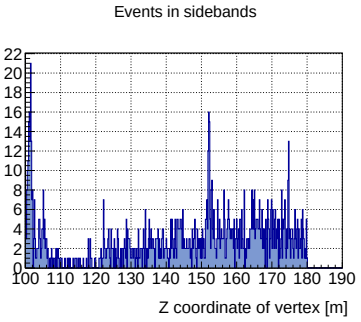

Figure 5.19: *Distribution of the Z coordinate of the two-track vertex, for data outside the blinded region and with two-track time difference (as given by the CHOD) between -2 ns and 2 ns, in the $N \to \pi^+\mu^-$ case.*

Background components

The radial position of the two-track vertex with respect to the Z axis is plotted as a function of its Z coordinate, both for MC signal events (Fig. 5.20) and for data (Fig. 5.21). From the comparison between Fig. 5.20 and Fig. 5.21, several background components are visible in the data distribution, which are not present in the MC signal distribution.

A component is visible in Fig. 5.21, at low Z coordinate and with vertex radial position spread between $\approx$ 10 cm and $\approx$ 60 cm. This component originates from muon interactions upstream of the FV, at the final collimator ($Z \approx 103$ m) and at the CHANTI ($Z \approx 105$ m), which produce in-time pairs of final state particles, and it is not expected to populate the blind region (as defined in Section 5.3).

Another contribution can be seen in Fig. 5.21, at $Z \approx 150$ m and vertex radial position greater than 50 cm. Since this value of Z corresponds to the position of LAV5, this background component is likely to come from beam pions and halo muons that interact with the LAV5 material, producing particle showers. In these showers, $ee/\mu e$ in-time pairs of opposite charge are produced and misidentified as $\pi\mu$ pairs (due to the presence of an in-time signal in the MUV3). This background component only occurs in the LAV5, which has a greater radius than all the following LAV stations, therefore leaving part of its geometric acceptance "uncovered".

This component ca be identified and removed at no extra cost for the signal acceptance (Fig. 5.20) by rejecting all events with vertex radial position greater than 50 cm.

From this point on, the plots shown and the studies detailed in the following assume that all data events contributing to these two components are not considered.

Fit to the sideband distribution

After excluding the combinatorial and the LAV5-produced components in the muon-induced background, the plot shown in Fig. 5.22 is obtained. The slope of the distribution for Z in the range [110, 120] m is the one expected to propagate in the blinded region, therefore the distribution of the number of events per bin which lay in the [110, 120] m region is fitted with a Poissonian function. The mean number of events in the sideband (between 102.4 m and 120 m) and in the FV (between 120 m and 180 m) can be computed as

$$N_{SB,FV} = \mu_P \cdot C \cdot L_{SB,FV}, \tag{5.4}$$

where $\mu_P \cdot C$ is the mean number of events per meter in Fig. 5.19; in fact, μ_P is the mean number of events per bin (from the Poissonian fit), $C = \frac{1}{B} = 5.55$ m^{-1} is

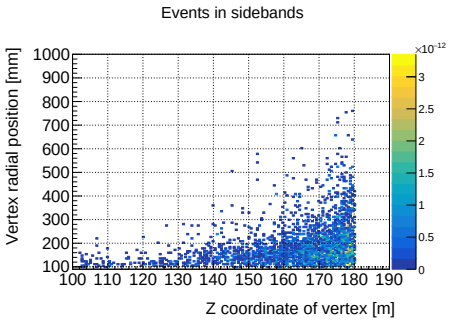

Figure 5.20: *Distribution of the two-track vertex radial position as a function of its Z coordinate, for all MC signal events outside the blinded region (no check on the CHOD two-track difference is performed, since MC events are time aligned), at different masses, $U^2 = 10^{-6}$ and for the general model ($U_e^2 : U_\mu^2 : U_\tau^2 = 1:1:1$), in the $N \to \pi^+\mu^-$ case. Each event is weighted for the quantity defined in Section 3.8.*

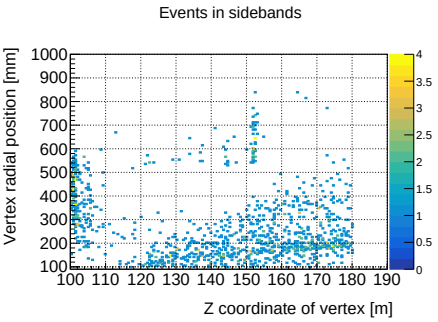

Figure 5.21: *Distribution of the two-track vertex radial position as a function of its Z coordinate, for all data events outside the blinded region and with a CHOD two-track difference in the range [-2, 2] ns, in the $N \to \pi^+\mu^-$ case.*

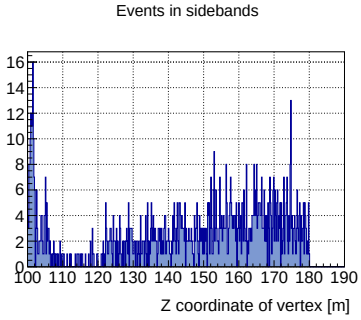

Figure 5.22: *Distribution of the Z coordinate of the two-track vertex, for data outside the blinded region and with two-track time difference (as given by the CHOD) between -2 ns and 2 ns, after the LAV5-produced component has been excluded, in the $N \to \pi^+\mu^-$ case.*

the conversion factor between the bin width (B) of the plot in Fig. 5.19 and meters, and $L_{SB,FV}$ is the length of the region considered for the computation ($L_{SB} = 17.6$ m for the sideband, and $L_{FV} = 60$ m in the FV case). These two quantities are used to compute the number of events in the FV and inside the blinded region, as described in the following paragraph.

Reconstructed invariant mass distribution

The distribution of the two-track reconstructed invariant mass can be studied for all events inside the sideband, for the $N \to \pi^+\mu^-$ sample (Fig. 5.23). This is done in order to evaluate the expected number of muon-induced background events for each HNL mass hypothesis.

The number of events inside the FV and blinded region is computed from the proportion

$$N_{SB} : N_{FV} = N_{SB+BR} : N_{FV+BR}, \tag{5.5}$$

where N_{SB} and N_{FV} have been computed in the previous paragraph, N_{SB+BR} is the number of events in the sideband, inside the blinded region and whose two-track time difference is in the range [-2, 2] ns, and N_{FV+BR} is the number of the same events expected inside the FV and blinded region. Since N_{SB+BR} is found to be 0, an upper limit of 2.3 events at 90% Confidence Level (CL) is assumed.

The distribution in Fig. 5.23 is rescaled in such way that its integral is equal to $N_{FV+BR} = \frac{N_{SB+BR} \cdot N_{FV}}{N_{SB}} = 6.9$, as shown in Fig. 5.24.

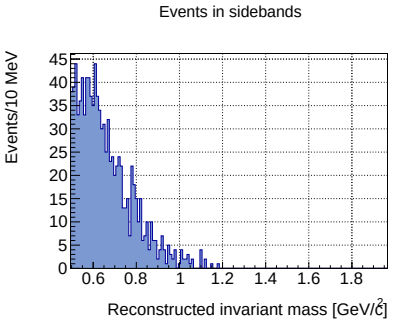

Figure 5.23: *Two-track reconstructed invariant mass distribution for data events in the sideband, with CHOD two-track difference in the range [-2, 2] ns and vertex radial position smaller than 50 cm, in the $N \to \pi^+\mu^-$ case.*

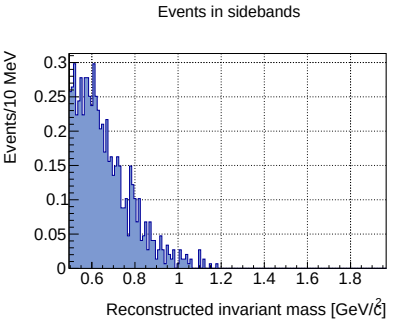

Figure 5.24: *Two-track reconstructed invariant mass distribution for data events in the sideband, with CHOD two-track difference in the range [-2, 2] ns and vertex radial position smaller than 50 cm, rescaled to the mean number of events in the FV and the blinded region, N_{FV+BR} (as computed in paragraph 5.5.3), in the $N \to \pi^+\mu^-$ case.*

Evaluation of the expected number of background events

With a procedure analogous to the one described in Section 5.5.2, a scan on the HNL mass hypothesis is performed on the distribution plotted in Fig. 5.24.

The expected number of muon-induced background events for each HNL mass hypothesis, for the $N \to \pi^+\mu^-$ sample, is plotted in Fig. 5.25 (Fig. 5.26) for a

1σ-wide (2σ-wide) mass window.

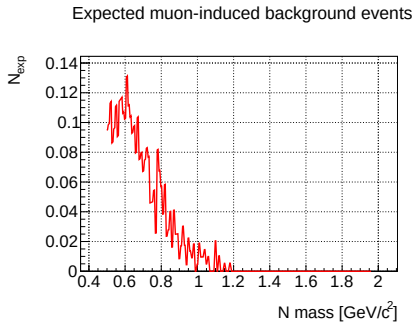

Figure 5.25: *Number of expected muon-induced background events for each HNL mass hypothesis, for a 1σ-wide mass window, in the $N \to \pi^+\mu^-$ case.*

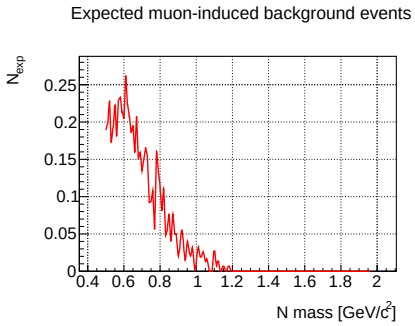

Figure 5.26: *Number of expected muon-induced background events for each HNL mass hypothesis, for a 2σ-wide mass window, in the $N \to \pi^+\mu^-$ case.*

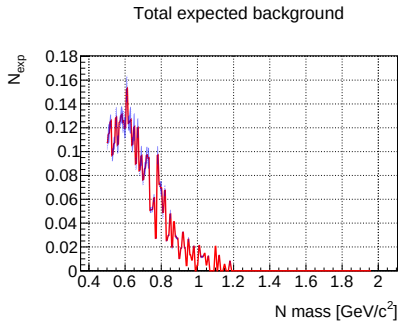

Figure 5.27: *Total number of expected background events for each HNL mass hypothesis, for a 1σ-wide mass window, in the $N \to \pi^+\mu^-$ case. The blue area indicates a 50% conservative systematic error assigned to the combinatorial background evaluation and due to the assumption of uniformity for the event distribution in the combinatorial sidebands.*

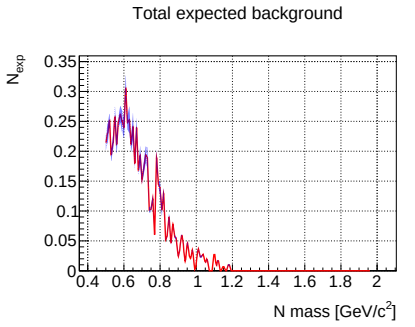

Figure 5.28: *Total number of expected background events for each HNL mass hypothesis, for a 2σ-wide mass window, in the $N \to \pi^+\mu^-$ case. The blue area indicates a 50% conservative systematic error assigned to the combinatorial background evaluation and due to the assumption of uniformity for the event distribution in the combinatorial sidebands.*

5.5.4 Total number of expected background events

The total number of expected background events for each HNL mass hypothesis is then computed by adding the contributions from all the background sources described in Section 5.5. The results are plotted in Fig. 5.27 (Fig. 5.28) for a 1σ (2σ) mass window, in the $N \to \pi^+\mu^-$ case.

5.6 Summary on background evaluation

Estimates on the total number of expected background events for each HNL mass hypothesis (in a 1σ and 2σ mass window) have been detailed for a reconstructed data sample collected in kaon mode for the HNL decay searches presented in this thesis and corresponding to $1 \cdot 10^{17}$ POT.

Three main sources of background have been considered: kaon-induced, combinatorial and muon-induced. The estimates discussed in this Chapter are restricted to HNL mass hypotheses above the kaon mass, to eliminate the kaon-induced background source.

Due to time constraints, the results presented here are not final. The evaluation discussed in this thesis shows that the level of background is negligible with a statistics of 10^{17} POT. Therefore, the zero-background hypothesis is achieved over an HNL mass range of about 2 GeV/c^2.

Additional studies could be performed to make a more robust background evaluation to $N \to \pi\mu$ decays. MC simulations of several processes could help in understanding the origin of backgrounds in more detail. Different distributions could be studied, to verify the assumptions made in the background evaluation procedure detailed in this Chapter. Cuts could be optimised to further help discriminating the MC signal sample against the main background sources and to gain more handles against background processes that could become significant at higher statistics.

Chapter 6

Conclusions and outlook

6.1 Conclusions

The studies detailed in this thesis discuss the sensitivity to HNL decays to pion-muon final states at the NA62 experiment at CERN. The work presented here has been performed in the theoretical framework of the νMSM, in a specific scenario where the HNL coupling to electrons is neglected and the one to τ leptons is enhanced with respect to the muon one. By analyzing the data sample collected in 2016-2018 in kaon operation mode, NA62 can set more restrictive limits on U_τ^2 as a function of the HNL mass, within the tau-dominant scenario.

In this thesis, the NA62 full Monte Carlo simulation implemented to produce HNL decays to pion-muon final states, where the HNLs are generated in D meson decays, has been detailed. It is available as an official tool in the NA62 framework and it will be used for future HNL production searches and decay searches to two-body, fully-reconstructible final states.

A thorough event selection optimised for these searches has been discussed as well. The expected sensitivity curve to $N \to \pi\mu$ decays at NA62 has been produced, for the chosen theoretical scenarios.

In addition to the full MC simulation and expected sensitivity studies, a data-driven background evaluation has been performed on a partial data set (corresponding to $1 \cdot 10^{17}$ POT) collected in 2016-2018 for the searches presented in this work. It is shown that the zero-background hypothesis is achieved for such statistics over a wide range of HNL masses, from about 0.2 GeV/c^2 to 2 GeV/c^2.

It is shown that the zero-background hypothesis is achieved for such statistics over a wide range of HNL masses, from about 0.2 GeV/c2 to 2 GeV/c2.

6.2 Outlook

The MC simulation implemented for this work simulates HNL production from D mesons and decay to two-body, fully-reconstructible final states at NA62. It could be extended to also account for HNL production from K and B mesons, and to simulate HNL decays to three-body final states.

The libraries developed within the official analysis framework allow to produce expected sensitivity curves for any theoretical scenario within the Neutrino Minimal Standard Model.

If the analysis framework were to be expanded with optimised event selections, expected sensitivity curves in any theoretical scenario could also be studied for several other two-body, fully-reconstructible HNL decay modes, which are already implemented in the full MC simulation. These could be used to analyse the 10^{18} POT data sample that will be collected by NA62 in 2021-2023 in dedicated beam-dump operation runs, to set upper limits for different HNL decay searches.

A project called MadDump currently exists and is being developed to simulate MC events for beam-dump experiments and to allow for the study of several long-lived, feebly-interacting particles. This includes the simulation of their production via different processes, their decay to selected final states and their propagation through the detector of the beam-dump experiment chosen for the event generation [66].

The results produced with the MC simulation coded for the study discussed in this thesis could be compared to the ones produced by the MadDump software, in the case of HNLs generated from D mesons and decaying to pion-muon final states, to test for the validity of both tools.

This could eventually result in the migration to the MadDump software by the NA62 collaboration, to perform broader HSM and DF searches during the beam-dump operation in 2021-2023.

Appendices

Appendix A

Heavy Neutral Lepton production modes

For convenience, the formulae used to compute the BRs of all HNL production modes listed in Section 1.3.1 are detailed here. Further information can be found in [12]. The used system of units is natural.

It must be noted that the HNL is a Majorana particle within these theoretical models. This means that charge-conjugated processes contribute to the HNL production as well. Each BR detailed in the following should be divided by two if the HNLs were Dirac particles.

Two-body, leptonic decays of D mesons:

$$BR(H \to N l_\alpha) = \frac{2\tau_H G_F^2 f_H^2 M_H M_N^2 |V_H|^2 |U_\alpha|^2}{8\pi} \times \left(1 - \frac{M_N^2}{M_H^2} + \frac{2M_l^2}{M_H^2} + \frac{M_l^2}{M_N^2}\left(1 - \frac{M_l^2}{M_H^2}\right)\right) \times \sqrt{\left(1 + \frac{M_N^2}{M_H^2} - \frac{M_l^2}{M_H^2}\right)^2 - \frac{4M_N^2}{M_H^2}}, \tag{A.1}$$

where H refers either to the D or D_S meson, τ_H is the meson lifetime, G_F is the Fermi coupling constant, f_H is the relevant hadronic decay constant and V_H is the corresponding CKM matrix element, both shown in Table A.1; $|U_\alpha|^2$ is the HNL coupling to the specific lepton it is produced in pair with ($\alpha = e, \mu, \tau$), and M_H, M_N and M_l are the meson, HNL and lepton masses.

H	π	K	D	D_S	η	η'
$f_H[MeV]$	130.0	159.8	222.6	280.1	156.0	-58.5
V_H	V_{ud}	V_{us}	V_{cd}	V_{cs}	None	None

Table A.1: *Hadronic decay constants and CKM matrix elements for several HNL production modes [28, 67].*

$f_+^{D\to K^0}$	$f_+^{D\to \pi^0}$	$f_+^{D^0\to K}$	$f_+^{D^0\to \pi}$	$f_-^{D\to K^0}$	$f_-^{D\to \pi^0}$	$f_-^{D^0\to K}$	$f_-^{D^0\to \pi}$
0.745	0.648	0.736	0.637	-0.495	-0.435	-0.495	-0.435

Table A.2: *Hadronic form factors for several HNL production modes involving pseudo-scalar mesons [28, 67].*

Three-body, semi-leptonic decays of D mesons into pseudo-scalar mesons:

$$\begin{aligned} BR(H \to H' l_\alpha N) = \frac{2\tau_H |U_\alpha|^2 |V_{HH'}|^2 G_F^2}{64\pi^3 M_H^2} \times \\ \int_{q^2_{min}}^{q^2_{max}} dq^2 (f_-^2 (q^2(M_N^2 + M_l^2) - (M_N^2 - M_l^2)^2) + \\ 2 f_+ f_- (M_N^2 (2M_H^2 - 2M_{H'}^2 - 4E_N M_H - M_l^2 + M_N^2 + q^2) + \\ M_L^2 (4E_N M_H + M_l^2 - M_N^2 - q^2)) + \\ f_+^2 ((4E_N M_{H'} + M_l^2 - M_N^2 - q^2)(2M_H^2 - 2M_{H'}^2 - 4E_N M_H - M_l^2 + M_N^2 + q^2) - \\ (2M_H^2 + 2M_{H'}^2 - q^2)(q^2 - M_N^2 - M_l^2))), \end{aligned} \tag{A.2}$$

where H refers either to the D, D^0 or $\bar{D}^0$ meson, H' refers to either π, π^0, K or K^0, $M_{H'}$ is the pseudo-scalar meson mass, E_N is the HNL energy in the mother rest frame and $V_{HH'}$ is the corresponding element of the CKM matrix, as shown in Table A.1; q^2 is the squared invariant mass of the leptonic pair Nl; $q^2_{min} = (M_N + M_l)^2$ is the minimum invariant mass of the $H'l$ pair, corresponding to the case where $H'l$ is produced back to back with respect to N (in the mother rest frame); $q^2_{max} = (M_H - M_{H'})^2$ occurs when H' and l are produced back to back and N is generated at rest (in the mother rest frame); $f_-(q^2)$ and $f_+(q^2)$ are the relevant hadronic form factors whose values are shown in Table A.2, where their kinematic dependence has been neglected.

Three-body, semi-leptonic decays of D mesons into vector mesons:

$$\begin{aligned} BR(H \to V l_\alpha N) = \frac{2\tau_H |U_\alpha|^2 |V_{HV}|^2 G_F^2}{32\pi^3 M_H^2} \times \\ \int_{q_{min}}^{q_{max}} dq^2 (\frac{f_2^2}{2} \left(q^2 - M_N^2 - M_l^2 + \omega^2 \frac{\Omega^2 - \omega^2}{M_V^2} \right) + \\ \frac{f_5^2}{2} (M_N^2 + M_l^2)(q^2 - M_N^2 + M_l^2) \left(\frac{\Omega^4}{4M_V^2} - q^2 \right) + \\ 2 f_3^2 M_V^2 \left(\frac{\Omega^4}{4M_V^2} - q^2 \right) \left(M_N^2 + M_l^2 - q^2 + \omega^2 \frac{\Omega^2 - \omega^2}{M_V^2} \right) + \\ 2 f_3 f_5 (M_N^2 \omega^2 + (\Omega^2 - \omega^2) M_l^2) \left(\frac{\Omega^4}{4M_V^2} - q^2 \right) + \\ 2 f_1 f_2 (q^2 (2\omega^2 - \Omega^2) + \Omega^2 (M_N^2 - M_l^2)) + \\ \frac{f_2 f_5}{2} \left(\frac{\omega^2 \Omega^2}{M_V^2} (M_N^2 - M_l^2) + \frac{\Omega^4 M_l^2}{M_V^2} + 2(M_N^2 - M_l^2)^2 - 2q^2 (M_N^2 + M_l^2) \right) + \\ f_2 f_3 \left(\Omega^2 \omega^2 \frac{\Omega^2 - \omega^2}{M_V^2} + 2\omega^2 (M_l^2 - M_N^2) + \Omega^2 (M_N^2 - M_l^2 - q^2) \right) + \\ f_1^2 (\Omega^4 (q^2 - M_N^2 + M_l^2) - 2M_V^2 (q^4 - (M_N^2 - M_l^2)^2) + \\ 2\omega^2 \Omega^2 (M_N^2 - q^2 - M_l^2) + 2\omega^4 q^2)), \end{aligned} \tag{A.3}$$

where H refers either to the D, D^0 or $\bar{D}^0$ meson, V refers to either $\mathrm{K}^{0*}(895)$ or $\mathrm{K}^*(891)$, M_V is the vector meson mass, V_{HV} is the corresponding CKM matrix element (Table A.1), and

$$\omega^2 = M_H^2 - M_V^2 + M_N^2 - M_l^2 - 2M_H E_N, \tag{A.4}$$

$$\Omega^2 = M_H^2 - M_V^2 - q^2; \tag{A.5}$$

form factors f_i can be expressed through the axial and vector form factors shown in Table A.3 as

$$f_1 = \frac{f_4^H}{M_H + M_V}, \tag{A.6}$$

$$f_2 = (M_H + M_V) f_2^H, \tag{A.7}$$

$$f_3 = -\frac{f_3^H}{M_H + M_V}, \tag{A.8}$$

$$f_4 = (M_V (2f_1^H - f_2^H - f_3^H) + M_H (f_3^H - f_2^H)) \frac{1}{q^2} \tag{A.9}$$

and

$$f_5 = f_3 + f_4. \tag{A.10}$$

f_1^D	f_2^D	f_3^D	f_4^D	$f_1^{D^0}$	$f_2^{D^0}$	$f_3^{D^0}$	$f_4^{D^0}$
0.398	0.470	-1.240	0.660	0.400	0.470	-1.240	0.660

Table A.3: *Hadronic form factors for several HNL production modes involving vector mesons [28].*

Two-body, semi-leptonic decays of τ leptons into pion or kaon:

$$BR(\tau \to HN) = \frac{2\tau_\tau |U_\tau|^2 G_F^2 |V_H|^2 f_H^2 M_\tau^3}{16\pi} \times \left(\left(1 - \frac{M_N^2}{M_\tau^2}\right)^2 - \frac{M_H^2}{M_\tau^2}\left(1 + \frac{M_N^2}{M_\tau^2}\right)\right) \times \sqrt{\left(1 - \frac{(M_H - M_N)^2}{M_\tau^2}\right)\left(1 - \frac{(M_H + M_N)^2}{M_\tau^2}\right)}, \tag{A.11}$$

where H refers either to π or K, M_τ is the τ lepton mass and U_τ^2 is the HNL coupling to the τ leptons.

Two-body, semi-leptonic decays of τ leptons into ρ mesons:

$$BR(\tau \to \rho N) = \frac{2\tau_\tau |U_\tau|^2 G_F^2 |V_{ud}|^2 g_\rho^2 M_\tau^3}{8\pi M_\rho^2} \times \left(\left(1 - \frac{M_N^2}{M_\tau^2}\right)^2 + \frac{M_\rho^2}{M_\tau^2}\left(1 + \frac{M_N^2 - 2M_\rho^2}{M_\tau^2}\right)\right) \times \sqrt{\left(1 - \frac{(M_\rho - M_N)^2}{M_\tau^2}\right)\left(1 - \frac{(M_\rho + M_N)^2}{M_\tau^2}\right)}, \tag{A.12}$$

where M_ρ is the ρ meson mass, V_{ud} can be found in Table A.1 and $g_\rho = 0.102$ GeV^2.

Three-body decays of τ leptons:

$$BR(\tau \to \nu_\tau l_\alpha N) = \frac{2\tau_\tau |U_\alpha|^2 G_F^2 M_\tau^2 E_N}{2\pi^3}\left(1 + \frac{M_N^2 - M_l^2}{M_\tau^2} - 2\frac{E_N}{M_\tau}\right) \times \left(1 - \frac{M_l^2}{M_\tau^2 + M_N^2 - 2E_N M_\tau}\right)\sqrt{E_N^2 - M_N^2}, \tag{A.13}$$

$$BR(\tau \to \bar{\nu_\alpha} l_\alpha N) = \frac{2\tau_\tau |U_\tau|^2 G_F^2 M_\tau^2}{4\pi^3}\left(1 - \frac{M_l^2}{M_\tau^2 + M_N^2 - 2E_N M_\tau}\right) \times \sqrt{E_N^2 - M_N^2}\left((M_\tau - E_N)\left(1 - \frac{M_N^2 + M_l^2}{M_\tau^2}\right) - \left(\frac{M_\tau^2 + M_N^2 - M_l^2 - 2E_N M_\tau}{M_\tau^2 + M_N^2 - 2E_N M_\tau}\right)\left(\frac{3(M_\tau - E_N)^2 + E_N^2 - M_N^2}{3M_\tau}\right)\right). \tag{A.14}$$

Appendix B

Heavy Neutral Lepton decay modes

For convenience, the formulae used for computing the partial decay widths of all HNL decay modes listed in Section 1.3.2 are detailed here (the BR of each mode can be computed by normalizing each partial decay width to the total decay width). Further information can be found in [12]. The used system of units is natural.

It must be noted that the HNL is a Majorana particle within these theoretical models. This means that charge-conjugated processes contribute to the HNL production as well. Each partial decay width should be divided by two if the HNLs were Dirac particles.

Two-body decays of HNLs:

$$\Gamma(N \to \pi^0 \nu_\alpha) = \frac{2|U_\alpha|^2 G_F^2 f_\pi^2 M_N^3}{32\pi} \left(1 - \frac{M_\pi^2}{M_N^2}\right)^2, \tag{B.1}$$

where M_π is the pion mass and f_π can be found in Table A.1;

$$\Gamma(N \to H l_\alpha) = \frac{2|U_\alpha|^2 G_F^2 f_H^2 M_N^3 |V_H|^2}{16\pi} \left(\left(1 - \frac{M_l^2}{M_N^2}\right)^2 - \frac{M_H^2}{M_N^2}\left(1 + \frac{M_l^2}{M_N^2}\right)\right), \tag{B.2}$$

where H refers to either K or π and $\alpha = e, \mu, \tau$;

$$\Gamma(N \to H' \nu_\alpha) = \frac{2|U_\alpha|^2 G_F^2 f_{H'}^2 M_N^3}{32\pi} \left(1 - \frac{M_{H'}^2}{M_N^2}\right)^2, \tag{B.3}$$

where H' refers either to the η or the η' meson and $f_{H'}$ is found in Table A.1;

$$\Gamma(N \to \rho l_\alpha) = \frac{2|U_\alpha|^2 G_F^2 g_\rho^2 M_N^3 |V_{ud}|^2}{8\pi M_\rho^2} \times \left(\left(1 - \frac{M_l^2}{M_N^2}\right)^2 + \frac{M_\rho^2}{M_N^2}\left(1 + \frac{M_l^2 - 2M_\rho^2}{M_N^2}\right)\right) \times \sqrt{\left(1 - \frac{(M_\rho - M_l)^2}{M_N^2}\right)\left(1 - \frac{(M_\rho + M_l)^2}{M_N^2}\right)}, \tag{B.4}$$

where M_ρ is the mass of the ρ meson;

$$\Gamma(N \to \rho^0 l_\alpha) = \frac{2|U_\alpha|^2 G_F^2 g_\rho^2 M_N^3 |V_{ud}|^2}{16\pi M_{\rho^0}^2}\left(1 + \frac{2M_{\rho^0}^2}{M_N^2}\right)\left(1 - \frac{M_{\rho^0}^2}{M_N^2}\right)^2, \tag{B.5}$$

where M_{ρ^0} is the mass of the ρ^0 meson.

HNL three-body decay modes:

$$\Gamma\left(N \to \sum_{\alpha,\beta} \nu_\alpha \bar{\nu}_\beta \nu_\beta\right) = \frac{G_F^2 M_N^5}{192\pi^3} \sum_\alpha |U_\alpha|^2; \tag{B.6}$$

$$\Gamma(N \to l_{\alpha\neq\beta} \bar{l_\beta} \nu_\beta) = \frac{G_F^2 M_N^5 |U_\alpha|^2}{192\pi^3}(1 - 8x^2 + 8x^6 - x^8 - 12x^4 \log x^2), \tag{B.7}$$

where $x = \frac{max[M_{l_\alpha}, M_{l_\beta}]}{M_N}$, and $M_{l_{\alpha,\beta}}$ are the masses of the $l_{\alpha,\beta}$ leptons, respectively;

$$\Gamma(N \to \nu_\alpha l_\beta \bar{l_\beta}) = \frac{G_F^2 M_N^5 |U_\alpha|^2}{192\pi^3}\left((C_1(1 - \delta_{\alpha\beta}) + C_3\delta_{\alpha\beta})((1 - 14x^2 - 2x^4 - 12x^6) \times \sqrt{1 - 4x^2} + 12x^4(x^4 - 1)L) + 4(C_2(1 - \delta_{\alpha\beta}) + C_4\delta_{\alpha\beta}) \times (x^2(2 + 10x^2 - 12x^4)\sqrt{1 - 4x^2} + 6x^4(1 - 2x^2 + 2x^4)L)\right), \tag{B.8}$$

where $x = \frac{M_l}{M_N}$,

$$L = \log\left(\frac{1 - 3x^2 - (1 - x^2)\sqrt{1 - 4x^2}}{x^2(1 + \sqrt{1 - 4x^2}}\right), \tag{B.9}$$

$$C_1 = \frac{1}{4}(1 - 4\sin\theta_w{}^2 + 8\sin\theta_w{}^4), \tag{B.10}$$

$$C_2 = \frac{1}{2}\sin\theta_w{}^2(2\sin\theta_w{}^2 - 1), \tag{B.11}$$

$$C_3 = \frac{1}{4}(1 + 4\sin\theta_w{}^2 + 8\sin\theta_w{}^4), \tag{B.12}$$

$$C_4 = \frac{1}{2}\sin\theta_w{}^2(2\sin\theta_w{}^2 + 1). \tag{B.13}$$

Here, θ_w is the Weinberg angle.

Appendix C

Heavy Neutral Lepton phenomenology within additional scenarios

Two extra scenarios that can be interesting to study are an "electron-dominant" one and a "muon-only" one. The former is described by

$$U_e^2 : U_\mu^2 : U_\tau^2 = 10 : 1 : 0 \tag{C.1}$$

and it is complementary to the tau-dominant scenario. In this case, the electron coupling is enhanced with respect to the muon one, while the coupling to third generation leptons is neglected.

In the muon-only scenario, only the mixing to second generation leptons is present, while the other two are suppressed:

$$U_e^2 : U_\mu^2 : U_\tau^2 = 0 : 1 : 0. \tag{C.2}$$

Fig. C.1 and Fig. C.2 display the BRs of all HNL production modes detailed in Section 1.3.1, whereas Fig. C.3 and Fig. C.4 show all HNL decay modes described in Section 1.3.2, for the electron-dominant and the muon-only scenarios. Here, the choice of setting $U^2 = 1$ is arbitrary and it is only used when plotting the BRs.

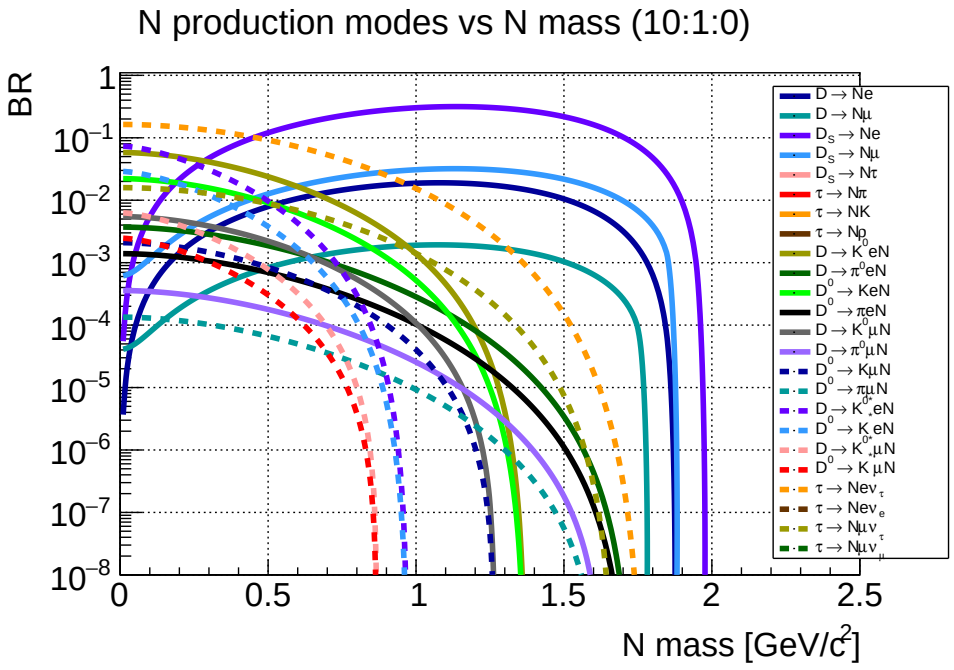

Figure C.1: *BRs for HNL production modes as a function of the HNL mass, for normal hierarchy of the active neutrino masses and for the electron-dominant model ($U^2 = 1$ and $U_e^2 : U_\mu^2 : U_\tau^2$ =10:1:0).*

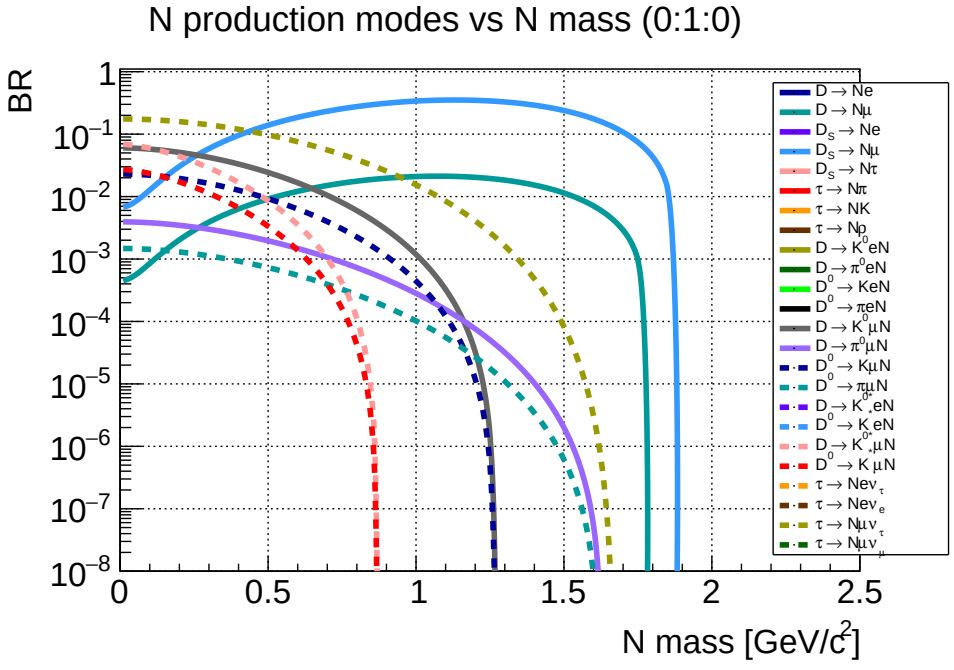

Figure C.2: *BRs for HNL production modes as a function of the HNL mass, for normal hierarchy of the active neutrino masses and for the muon-only model ($U^2 = 1$ and $U_e^2 : U_\mu^2 : U_\tau^2$ =0:1:0).*

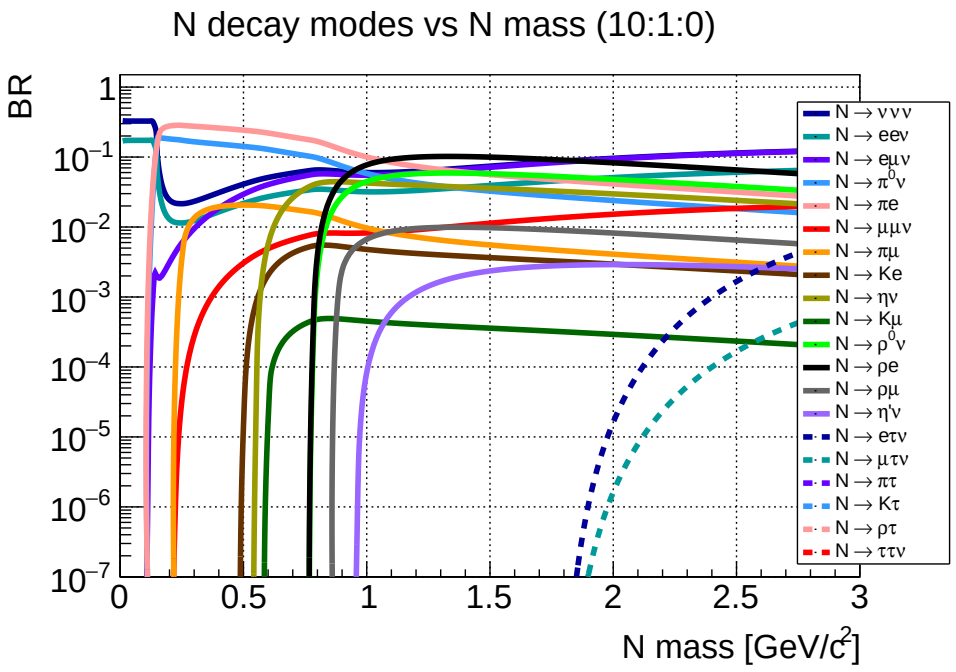

Figure C.3: *BRs for HNL decay modes as a function of the HNL mass, for normal hierarchy of the active neutrino masses and for the electron-dominant model ($U^2 = 1$ and $U_e^2 : U_\mu^2 : U_\tau^2$ =10:1:0).*

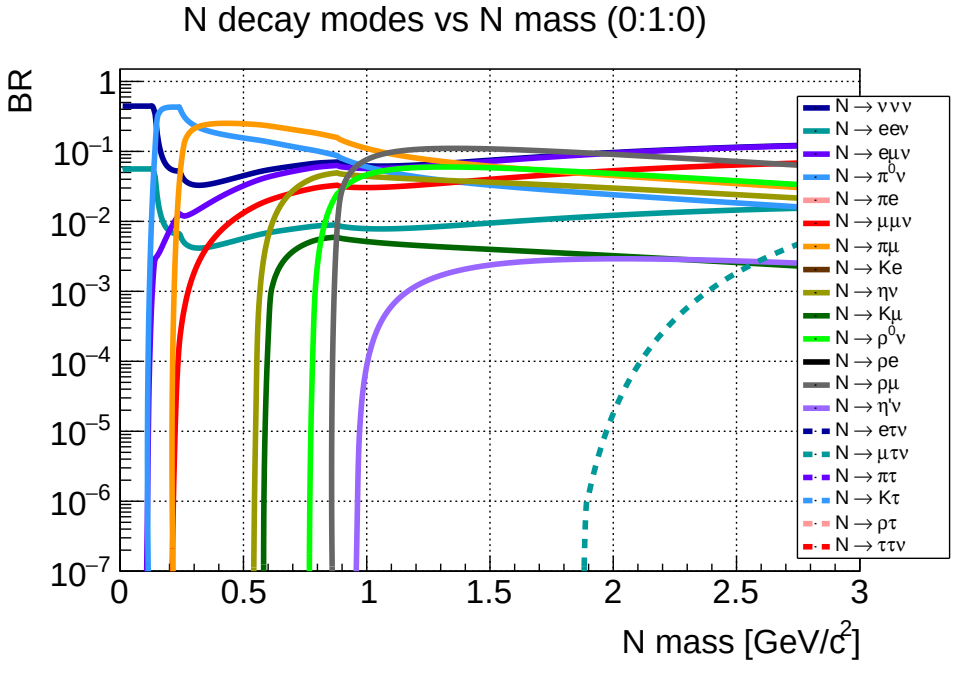

Figure C.4: *BRs for HNL decay modes as a function of the HNL mass, for normal hierarchy of the active neutrino masses and for the muon-only model ($U^2 = 1$ and $U_e^2 : U_\mu^2 : U_\tau^2$ =0:1:0).*

As described in [12], three additional benchmark scenarios can be interesting, where one of the three specific-flavour couplings is enhanced with respect to the other two. A detailed explanation on how the coupling ratios were obtained can be found in [12].

The three scenarios, called "model I", "model II" and "model III", are described by the following ratios:

$$U_e^2 : U_\mu^2 : U_\tau^2 = 52 : 1 : 1, \tag{C.3}$$

$$U_e^2 : U_\mu^2 : U_\tau^2 = 1 : 16 : 3.8, \tag{C.4}$$

$$U_e^2 : U_\mu^2 : U_\tau^2 = 0.061 : 1 : 4.3. \tag{C.5}$$

Fig. C.5 to Fig. C.7 show the BRs of all HNL production modes detailed in Section 1.3.1, while all HNL decay modes described in Section 1.3.2 are plotted in Fig. C.8 to Fig. C.10, for the three described benchmark scenarios. Here, the choice of setting $U^2 = 1$ is arbitrary and it is only used when plotting the BRs.

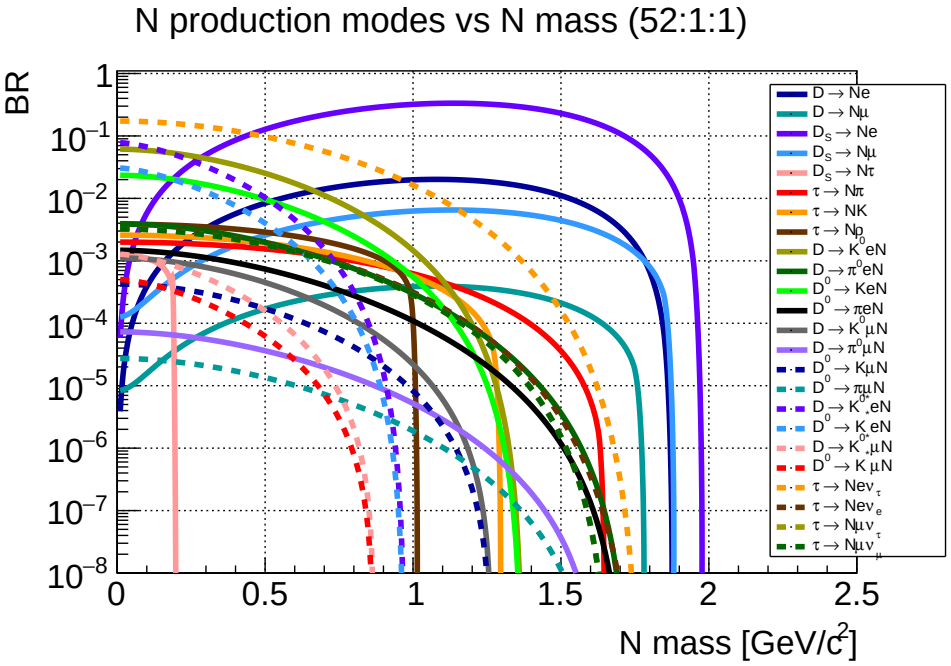

Figure C.5: *BRs for HNL production modes as a function of the HNL mass, for normal hierarchy of the active neutrino masses and for model I ($U^2 = 1$ and $U_e^2 : U_\mu^2 : U_\tau^2$ =52:1:1).*

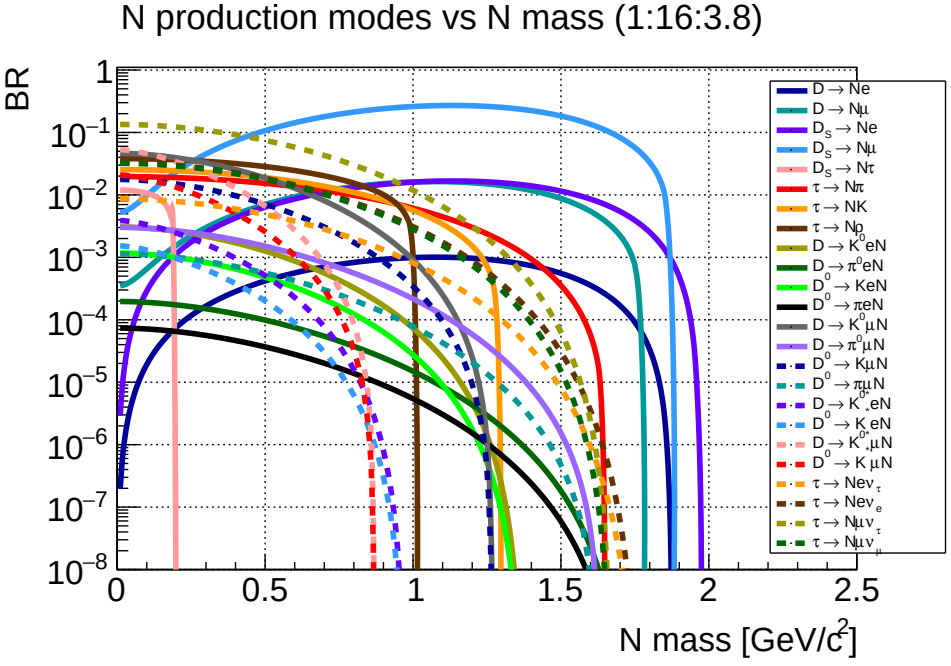

Figure C.6: *BRs for HNL production modes as a function of the HNL mass, for normal hierarchy of the active neutrino masses and for model II ($U^2 = 1$ and $U_e^2 : U_\mu^2 : U_\tau^2$ =1:16:3.8).*

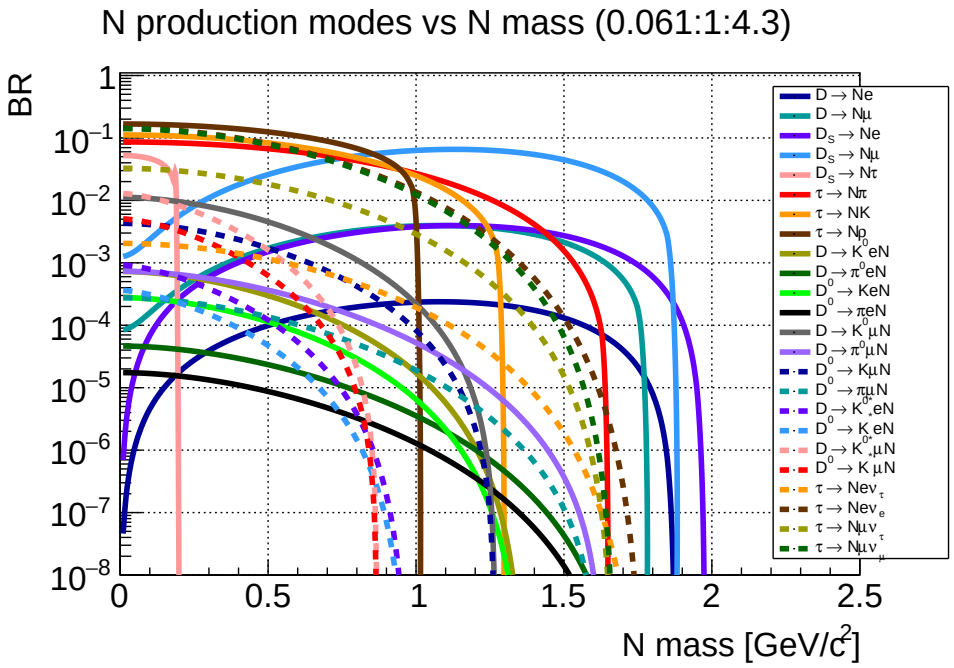

Figure C.7: *BRs for HNL production modes as a function of the HNL mass, for normal hierarchy of the active neutrino masses and for model III ($U^2 = 1$ and $U_e^2 : U_\mu^2 : U_\tau^2$ =0.061:1:4.3).*

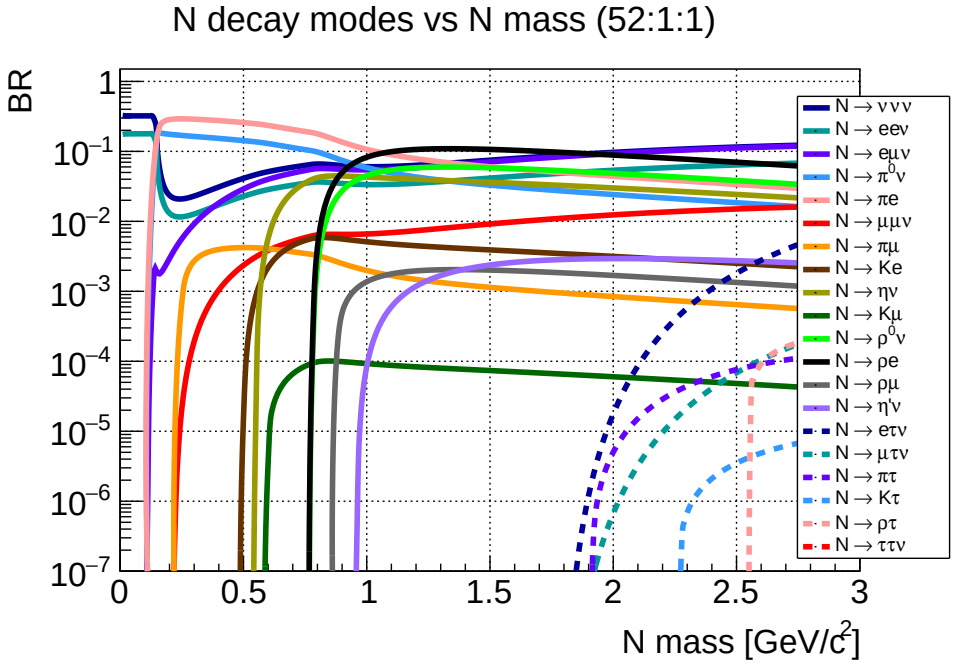

Figure C.8: *BRs for HNL decay modes as a function of the HNL mass, for normal hierarchy of the active neutrino masses and for model I ($U^2 = 1$ and $U_e^2 : U_\mu^2 : U_\tau^2$ =52:1:1).*

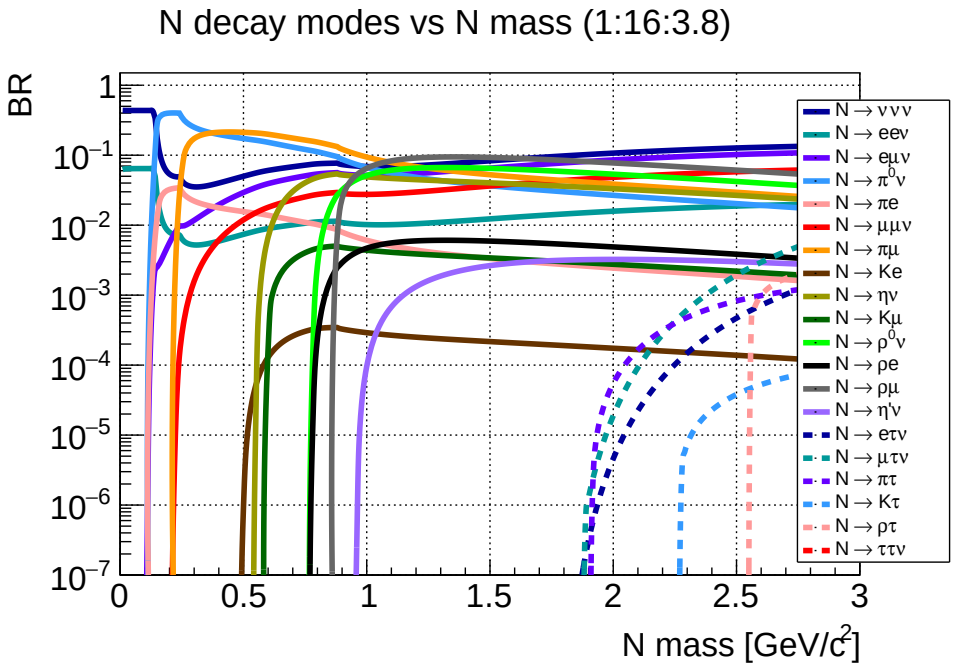

Figure C.9: *BRs for HNL decay modes as a function of the HNL mass, for normal hierarchy of the active neutrino masses and for model II ($U^2 = 1$ and $U_e^2 : U_\mu^2 : U_\tau^2$ =1:16:3.8).*

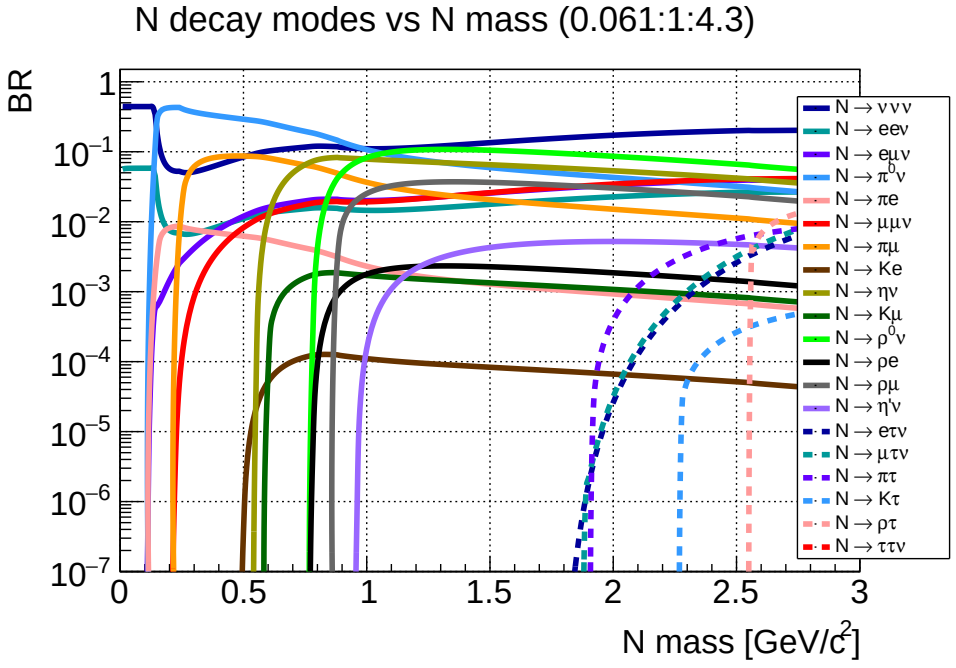

Figure C.10: *BRs for HNL decay modes as a function of the HNL mass, for normal hierarchy of the active neutrino masses and for model III ($U^2 = 1$ and $U_e^2 : U_\mu^2 : U_\tau^2$ =0.061:1:4.3).*

Appendix D

Status of searches and future prospects for additional benchmark scenarios

D.1 Electron-dominant scenario

A status of decay searches with HNLs coupling only to first generation leptons is discussed in the following. Further details can be found in the Beyond the Standard Model (BSM) working group of the Physics Beyond Collider (PBC) project [40].

Existing bounds within this scenario (Fig. D.1), for masses below the D meson mass, arise mostly from beam dump experiments (PS191 [68] and CHARM [30]), while those above the D meson mass are dominated by DELPHI [69], BELLE [70] and CMS [71]. The allowed range of couplings is bounded from below by the BBN constraint [47] and the see-saw limits [40].

The PS191 CERN experiment was specifically designed to search for neutrino decays in a low-energy neutrino beam, while CHARM performed a search for heavy neutrinos by dumping 400 GeV/c protons from the CERN SPS on a thick beam dump and looking for visible decays with electrons in the final state.

The Belle experiment searched for heavy neutrinos in leptonic and semileptonic B mesons decays, in a range of masses between the kaon and the B meson mass.

The most stringent limits above the B meson mass have been put by DELPHI in hadronic Z^0 decays.

CMS searched for HNLs in three prompt, charged-lepton samples in any combination of electrons and muons, collected at a centre-of-mass energy of 13 TeV.

On a 10-15 year timescale, many PBC projects can contribute to the electron-dominant benchmark case, as shown in Fig. D.1: MATHUSLA200, FASER, CODEX-b and SHiP. Fig. D.1 shows also projections from the Long Baseline Neut-

rino Experiment (LBNE) near detector as a 5-year sensitivity and from FCC-ee.

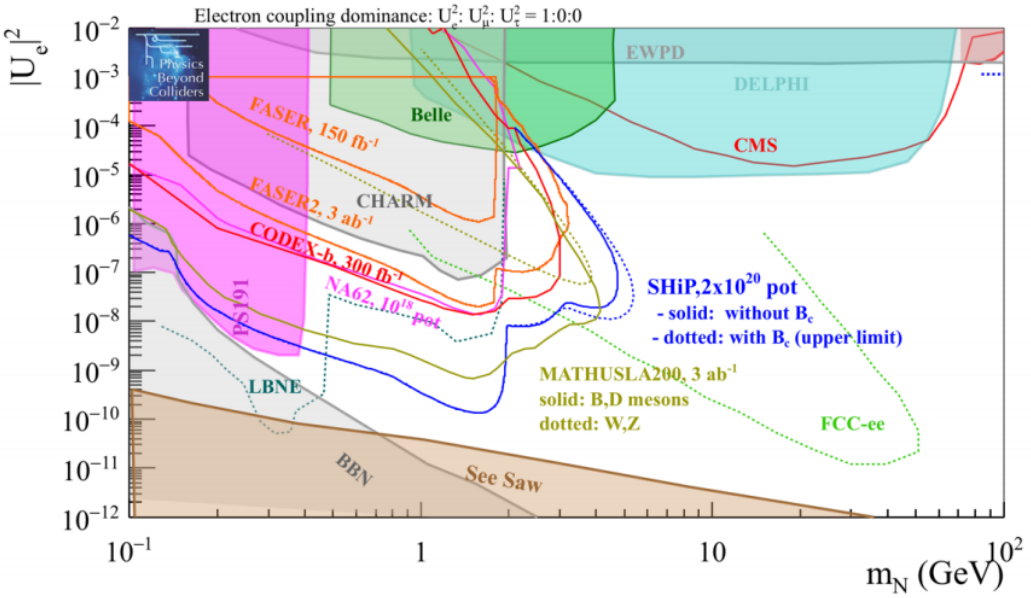

Figure D.1: *Sensitivity at 90% CL to HNLs with coupling to the first generation lepton only, for a scenario in which $U_e^2 : U_\mu^2 : U_\tau^2 = 1{:}0{:}0$. Current bounds (filled areas), 2021-2023 projections for NA62, and 10-15 years prospects (solid and dotted curves) for PBC projects (SHiP, MATHUSLA200, CODEX-b and FASER). Projections from FCC-ee and LBNE are also shown. BBN and see-saw model constraints are visible [40].*

D.2 Muon-dominant scenario

Current bounds for the case of HNL with coupling only to the second lepton generation and masses in the MeV-GeV range are shown in Fig. D.2. Also in this case the allowed range of couplings is bounded from below by the BBN constraint [47] and the see-saw limit [40]. For masses below the D meson mass, the existing limits arise mostly from the same beam dump experiments contributing to the sensitivity for electron-flavor dominance described in Section E.1 (PS191 [68] and CHARM [30]). Moreover, NuTeV [32] and E949 [38] also contributed to set existing bounds. Above the D meson mass, current bounds are set by DELPHI [69], Belle [70], CMS [71] with the same analysis used to set bounds for the electron-dominance scenario, and by LHCb [72].

The NuTeV experiment at Fermilab searched for HNLs decaying into muonic final states, using 800 GeV/c protons interacting with a berillium target and a proton dump, while the E949 collaboration performed HNL production searches in $K^+ \to \mu^+ N$ decays.

Fig. D.2 also shows the 90% CL exclusion limits from MATHUSLA200, FASER,

CODEXb and SHiP in a 10-15 years time scale.

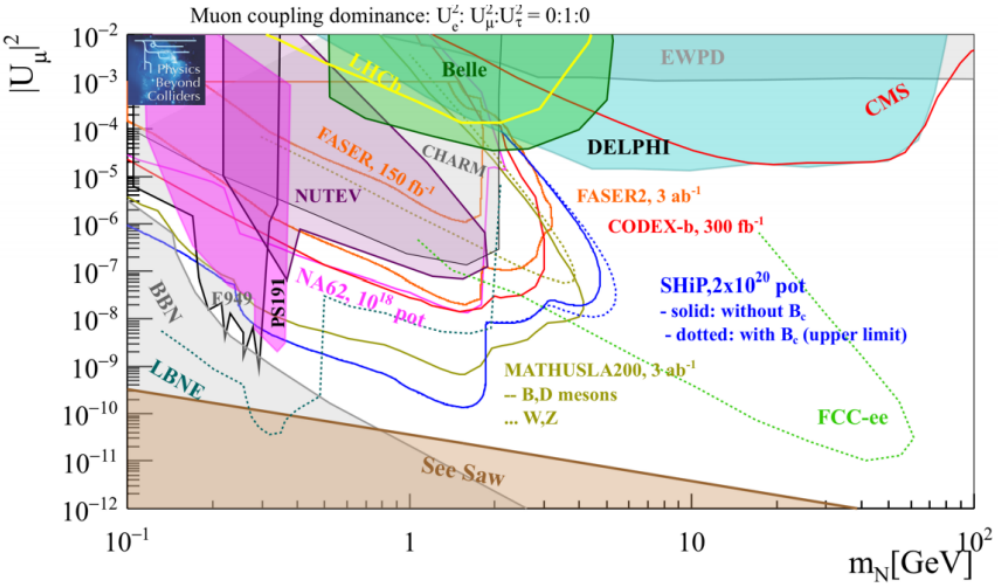

Figure D.2: *Sensitivity at 90% CL to HNLs with coupling to the second generation lepton only, for a scenario in which $U_e^2 : U_\mu^2 : U_\tau^2 = 0{:}1{:}0$. Current bounds (filled areas), 2021-2023 projections for NA62, and 10-15 years prospects (solid and dotted curves) for PBC projects (SHiP, MATHUSLA200, CODEX-b and FASER). Projections from FCC-ee and LBNE are also shown. BBN and see-saw model constraints are visible [40].*

Appendix E

Expected sensitivity curves within additional scenarios

Expected sensitivity curves can also be produced for the additional theoretical scenarios described in Appendix C, namely the electron-dominant and muon-only ones (Fig. E.1 and Fig. E.2), and model I, II and III (Fig. E.3, Fig. E.4 and Fig. E.5).

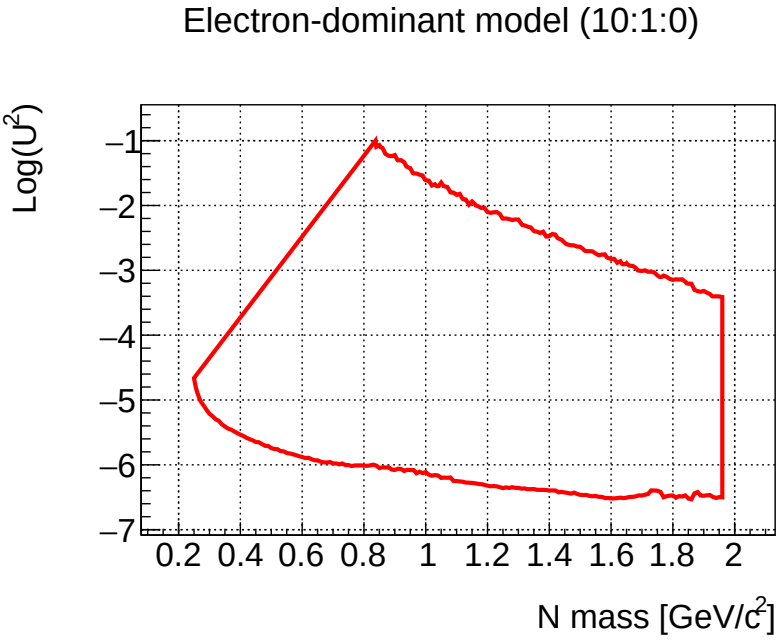

Figure E.1: *NA62 expected sensitivity in the plane coupling vs HNL mass, at 90% CL, for the electron-dominant model ($U_e^2 : U_\mu^2 : U_\tau^2 = 10{:}1{:}0$).*

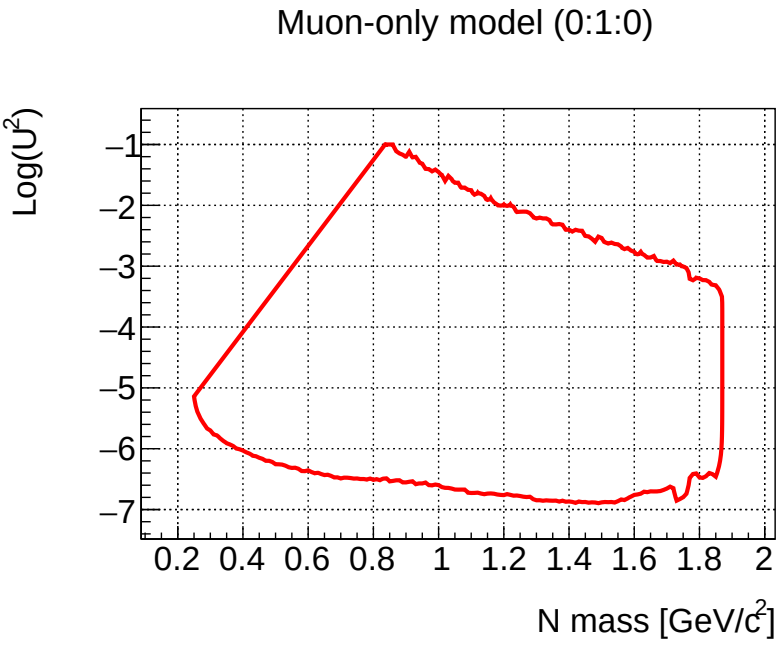

Figure E.2: *NA62 expected sensitivity in the plane coupling vs HNL mass, at 90% CL, for the muon-only model ($U_e^2 : U_\mu^2 : U_\tau^2 = 0{:}1{:}0$).*

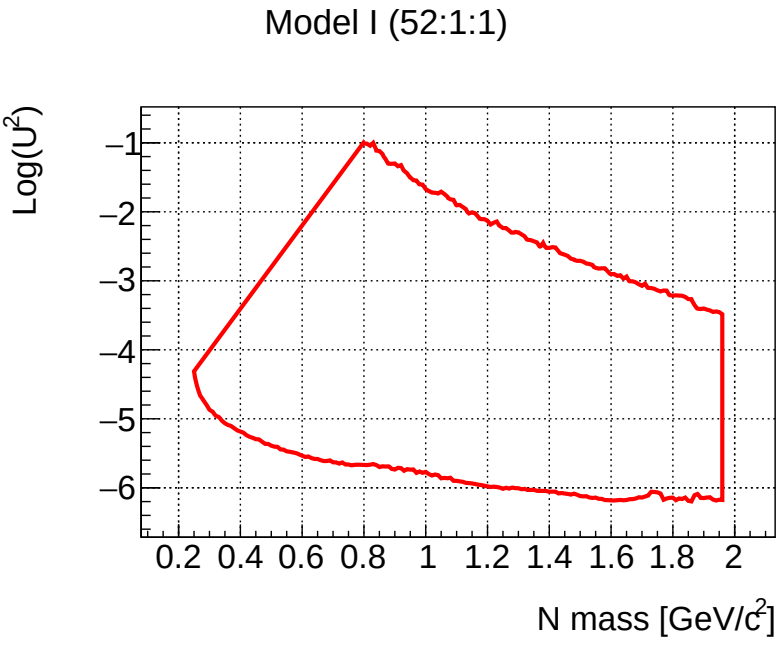

Figure E.3: *NA62 expected sensitivity in the plane coupling vs HNL mass, at 90% CL, for model I ($U_e^2 : U_\mu^2 : U_\tau^2 = 52{:}1{:}1$).*

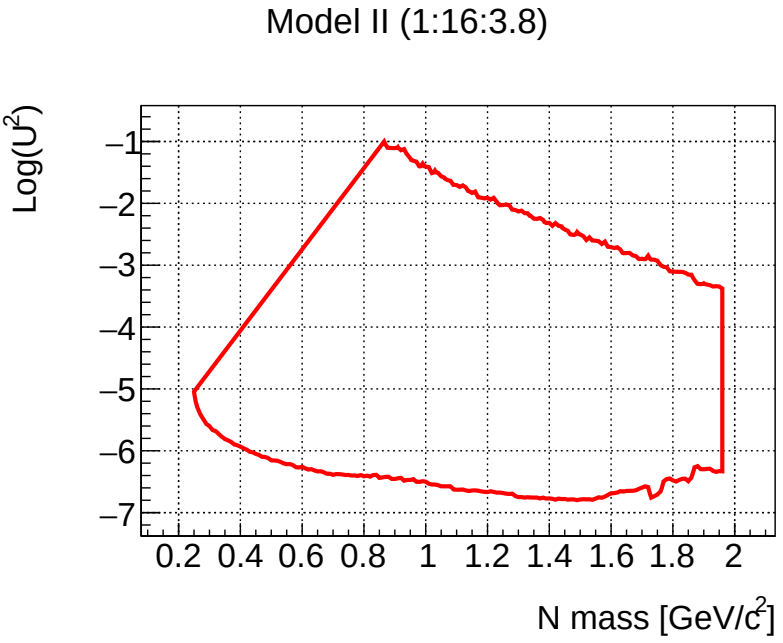

Figure E.4: *NA62 expected sensitivity in the plane coupling vs HNL mass, at 90% CL, for model II ($U_e^2 : U_\mu^2 : U_\tau^2 = 1{:}16{:}3.8$).*

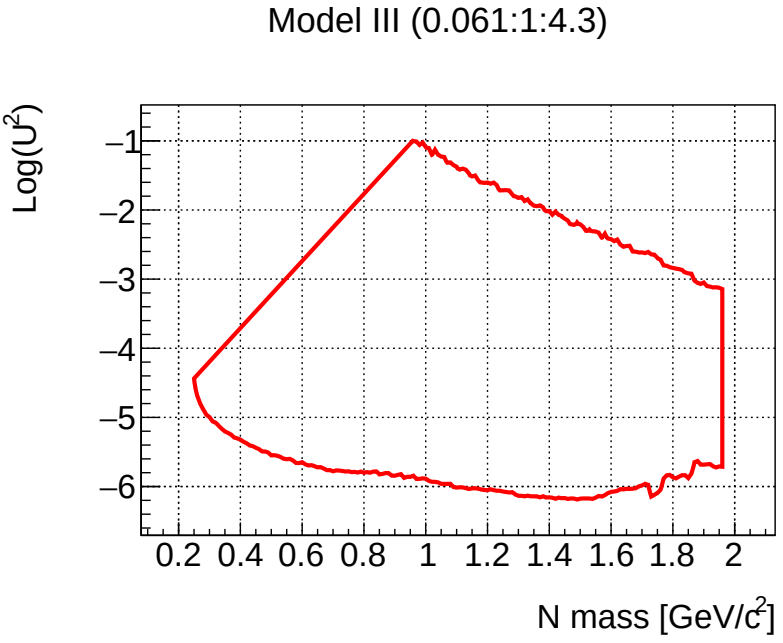

Figure E.5: *NA62 expected sensitivity in the plane coupling vs HNL mass, at 90% CL, for model III ($U_e^2 : U_\mu^2 : U_\tau^2 = 0.061{:}1{:}4.3$).*

Acknowledgements

A PhD is like a pregnancy, only five times longer. And, as with pregnancies, I believe the first acknowledgment is fairly due to the mother. So, here it is: from me, to me - and I think I deserve it.

Nonetheless, there are people that can help making the whole experience less painful: doctors and obstetricians in one case, family and friends in the other. And so, thanks...

...To Elena, for being by my side for the last 17 years. For being there when I needed to borrow her dresses during high school, 15 years ago, and for being there when I needed to borrow her dresses during nights out in Copenhagen, few weeks ago (certain things never change). For laughing together with those silent laughters that make your belly hurt, for chatting until late at night, for asking me how I am and meaning it, for doing my makeup, for her "Ciao, cuore". And to her little and loud family, for cuddling me as much as I need and always making me feel like the uncle from America (or the aunt from England), and for their "Zia Lo...?".

...To the whole NA62 crew, the family I didn't ask for, who made everything brighter and made the times at CERN feel more like a holiday than a job. Especially, to Silvia, for her didactic approach to life (and paragliding), for teaching me how to take pictures without teaching me, and for being my Rosetta Stone when learning how to be a Roman. To Matt, for talking about any possible topic ever conceived in the universe, for his awesome accents (the American and the Italian one) and for those oysters we never ate together. To Nicolas, for spending countless hours fighting my segfaults, for his homemade croissants, for his random acts of kindness and for being French without being French. To Maria Brigida, my desk neighbour, partner in disgrace and confidante during those endless stressful times, and for our afternoon teas that were more like therapy sessions. To Sensei Karim, for teaching me "Metti la cera, togli la cera". To FrancescA Brizioli, for always laughing at me (and sometimes with me, but very rarely). To Robertino Piandani, for ex-friending me plenty of times (and probably once more now that I thanked Brizioli before him). To Matteo, for being the only person who laughs more than me and for all his stories. To Riccardo Lollini, for being the greatest conference buddy I could ask

for and being my spiritual guide in a very specific time of my life. To all the guys in the NA62 WhatsApp chat, to the infamous awesome barbecues, the endless night shifts, the Fantacalcio tournament, the countless laughters... For making all of this so much more worth.

...To Angela, the best, most glamorous, most Neapolitan advisor I could ask for. For bringing the sun every time she walked into my office (and it's not easy, in England), for being a great supervisor and an even more amazing friend. And for taking me to Madrid to eat tons of pimientos del padron when I needed it the most.

...To Dome, for being my therapist even when I didn't want him to, for videochatting with me for two hours that time I had tonsillitis and couldn't talk, for grabbing his coat and coming with me to see Metallica (a truly great adventure time). And for getting back into my life after 10 years.

...To Lorenzo, for telling me I am smart when I feel like an idiot, and for telling me I am an idiot all the other times (just like a true friend).

...To Riccardo, for our flamboyant karaoke nights and for laughing together like kids in primary school. It took us a PhD school in Vietnam to meet, despite coming both from Torino, but it was worth the plane ticket (especially because I didn't pay for it).

...To Marco, for our endless "Il disagio siamo noi" phone calls and for teaching me about all the reforms of Leopoldo I.

...To Esh, for our brunches, his amazing stories and that other thing he knows about.

...To Cristina, for being a deputy mom more than once.

...To Tommaso, not only for the ridiculous amount of time he dedicated me for my analysis, but especially for his extensive and deep knowledge of Boris (matched only by Karim and myself).

...To the Brummies, for the lunch breaks, the mojitos and the cuddles, and especially to Laura, for her couch, the triple chocolate cake and the nights watching Gomorrah.

...To whomever helped me with technical stuff, physics stuff, programming stuff, complicated stuff, easy stuff, stuff I couldn't understand, stuff I didn't want to understand but I had to, all kinds of stuff.

...To someone who left me alone in the middle of Rio de Janeiro with nowhere to go, because it changed my life into something a hundred times better.

...To Enrique, porque la idea de no volver a verte hubiera sido simplemente ridicula. Gracias por pasar.

...To mom and dad. I could have said all the reasons why, but in the end there is only one reason: because no parent is perfect, but they are pretty damn close.

Bibliography

[1] J. Feng. *Dark matter candidates from particle physics and methods of detection.* Ann. Rev. Astron. Astrophys., 48:495–545, 2010.

[2] G. Fantini, A. Gallorosso, F. Vissani, and V. Zema. *The formalism of neutrino oscillations: an introduction.* arXiv, 1802:05781, 2018.

[3] B. Pontecorvo. *Neutrino experiments and the problem of conservation of leptonic charge.* Sov. Phys. JETP, 6:429, 1957.

[4] R. Davis. *A review of the Homestake solar neutrino experiment.* Progress in Particle and Nuclear Physics, 32:13 – 32, 1994.

[5] J. Cline. *Baryogenesis.* arXiv, hep-ph:0609145, 2006.

[6] M. Madhavacheril. *Evidence of lensing of the cosmic microwave background by dark matter halos.* Phys. Rev. Lett., 114:151302, 2015.

[7] L. Roszkowski, E. Sessoloc, and S. Trojanowskid. *WIMP dark matter candidates and searches – current status and future prospects.* arXiv, 1707:06277, 2018.

[8] D. Akerib. *Limits on spin-dependent WIMP-nucleon cross section obtained from the complete LUX exposure.* Phys. Rev. Lett., 118:251302, 2017.

[9] The NA62 collaboration. *Proposal to measure the rare decay $K^+ \to \pi^+ \nu\bar{\nu}$ at the CERN SPS.* (CERN-SPSC-2005-013. SPSC-P-326), 2005.

[10] T. Asaka, S. Blanchet, and M. Shaposhnikov. *The νMSM, dark matter and neutrino masses.* Phys. Lett. B, 631:151–156, 2005.

[11] T. Asaka and M. Shaposhnikov. *The νMSM, dark matter and baryon asymmetry of the universe.* Phys. Lett. B, 620:17–26, 2005.

[12] D. Gorbunov and M. Shaposhnikov. *How to find neutral leptons of the νMSM?* JHEP, 0710, 2007.

[13] M. Shaposhnikov and I. Tkachev. *The νMSM, inflation and dark matter.* Phys. Lett. B, 639:414, 2006.

[14] A. Boyarsky, A. Neronov, O. Ruchayskiy, and M. Shaposhnikov. Phys. Rev. Lett., 97:261302, 2006.

[15] T. Asaka, M. Laine, and M. Shaposhnikov. *Lightest sterile neutrino abundance within the νMSM.* JHEP, 0701:091, 2007.

[16] S. Dodelson and L. M. Widrow. *Sterile neutrinos as dark matter.* Phys. Rev. Lett., 72:17, 1994.

[17] X. D. Shi and G. M. Fuller. *A new dark matter candidate: non-thermal sterile neutrinos.* Phys. Rev. Lett., 82:2832, 1999.

[18] A. Dolgov and S. Hansen. *Massive sterile neutrinos as warm dark matter.* Astropart. Phys., 16:339, 2002.

[19] K. Abazajian, G. Fuller, and M. Patel. *Sterile neutrinos, hot, warm and cold dark matter.* Phys. Rev. D, 64:023501, 2001.

[20] B. Moore, S. Ghigna, F. Governato et al. *Dark matter substructure in galactic halos.* Astrophys. J., 524:19, 1999.

[21] P. Bode, J. Ostriker, and N. Turok. *Halo formation in warm dark matter models.* Astrophys. J., 556:93, 2001.

[22] S. Tulin, H. Yu, and K. Zurek. *Resonant dark forces and small scale structure.* Mon. Not. Roy. Astron. Soc., 368:1073, 2006.

[23] J.J. Dalcanton and C.J. Hogan. *Halo cores and phase space densities: Observational constraints on dark matter physics and structure formation.* Astrophys. J., 561:35, 2001.

[24] A. D. Sakharov. *Violation of CP invariance, C asymmetry, and baryon asymmetry of the universe.* Pisma Zh. Eksp. Teor. Fiz., 5:32, 1967.

[25] E. Akhmedov, V. Rubakov, and A. Smirnov. *Baryogenesis via neutrino oscillations.* Phys. Rev. Lett., 81:1359, 1998.

[26] M. Shaposhnikov. *A possible symmetry of the νMSM.* Nucl. Phys. B, 763:49, 2007.

[27] Z. Maki, M. Nakagawa, and S. Sakata. Prog. Theor. Phys., 28:870, 1962.

[28] Particle Data Group. *Particle data book.* Phys. Rev. D, 98, 2018.

[29] G. Bernardi, G. Carugno, J. Chauveau et al. *Further limits on heavy neutrino couplings.* Phys. Lett. B, 203:332, 1988.

[30] J. Dorenbosch, J.V. Allaby, U. Amaldi et al. *A search for decays of heavy neutrinos in the mass range 0.5 to 2.8 GeV.* Phys. Lett. B, 166:473, 1986.

[31] A.M. Cooper-Sarkar, S.J. Haywood, M.A. Parker et al. *Search for heavy neutrino decays in the BEBC beam dump experiment.* Phys. Lett. B, 160:207, 1985.

[32] A. Vaitaitis, R. B. Drucker, J. Formaggio et al. *Search for neutral heavy leptons in a high-energy neutrino beam.* Phys. Rev. Lett., 83:4943, 1999.

[33] The T2K collaboration. *Search for heavy neutrinos with the T2K near detector ND280.* arXiv, 1902:07598, 2019.

[34] A. Aguilar-Arevalo, M. Aoki, M. Blecher et al. *Improved search for heavy neutrinos in the decay* $\pi^+ \to e^+\nu_e$. Phys. Rev. D, 97:072012, 2018.

[35] R. S. Hayano, T. Taniguchi, T. Yamanaka et al. *Heavy-neutrino search using* $K_{\mu 2}$ *decays.* Phys. Rev. Lett., 49:1305, 1982.

[36] The NA62 collaboration. *Search for heavy neutrinos in* $K^+ \to \mu^+\nu_\mu$ *decays.* Phys. Lett. B, 772:712, 2017.

[37] The NA62 collaboration. *Search for heavy neutral lepton production in* K^+ *decays.* Phys. Lett. B, 778:137 – 145, 2018.

[38] A.V. Artamonov, B. Bassalleck, B. Bhuyan et al. *Search for heavy neutrinos in* $K^+ \to \mu^+\nu_h$ *decays.* Phys. Rev. D, 91, 2015.

[39] D. Bryman and R. Shrock. *Improved constraints on sterile neutrinos in the MeV to GeV mass range.* Phys. Rev. D, 100:053006, 2019.

[40] J. Beacham, C. Burrage, D. Curtin et al. *Physics Beyond Colliders at CERN: Beyond the Standard Model working group report.* CERN-PBS report, 007, 2018.

[41] J. Orloff, A. Rozanov, and C. Santoni. *Limits on the mixing of tau neutrino to heavy neutrinos.* Phys. Lett. B, 550:8–15, 2002.

[42] The DELPHI collaboration. *Search for neutral heavy leptons produced in Z decays.* Z. Phys., C74:57, 1997.

[43] J. Feng, I. Galon, F. Kling, and S. Trojanowski. *FASER: ForwArd Search ExpeRiment at the LHC*. Phys. Rev. D, 97:053001, 2018.

[44] The SHIP collaboration. *A facility to search for hidden particles at the CERN SPS: the SHiP physics case*. Rep. Prog. Phys., 79:124201, 2016.

[45] Curtin D. et al. *Long-lived particles at the energy frontier: The MATHUSLA physics case*. arXiv, 1806:07396, 2018.

[46] V. Gligorov, S. Knapen, M. Papucci, and D. Robinson. *Searching for long-lived particles: A compact detector for exotics at LHCb*. Phys. Rev. D, 97:015023, 2018.

[47] A. Dolgov, S. Hansen, G. Raffelt, and D. Semikoz. *Heavy sterile neutrinos: Bounds from big-bang nucleosynthesis and SN 1987A*. Nucl. Phys. B, 590:562, 2000.

[48] The NA31 collaboration. *First evidence for direct CP violation*. Phys. Lett. B, 206:169 – 176, 1988.

[49] J. Christenson, J. Cronin, V. Fitch, and R. Turlay. *Evidence for the 2π decay of the k_2^0 meson*. Phys. Rev. Lett., 13:138–140, 1964.

[50] A. J. Buras, D. Buttazzo, J. Girrbach-Noe, and R. Knegjens. *$K^+ \to \pi^+\nu\bar{\nu}$ and $K_L \to \pi^0\nu\bar{\nu}$ in the Standard Model: status and perspectives*. JHEP, 2015:33, 2015.

[51] The NA62 collaboration. *First search for $K^+ \to \pi^+\nu\bar{\nu}$ using the decay-in-flight technique*. Phys. Lett. B, 791:156, 2019.

[52] The NA62 collaboration. *Searches for lepton number violating K^+ decays*. arXiv, 1905:07770, 2019.

[53] The NA62 collaboration. *Search for production of an invisible dark photon in π^0 decays*. JHEP, 05:182, 2019.

[54] The NA62 collaboration. *The beam and detector of the NA62 experiment at CERN*. JINST, 12:P05025, 2017.

[55] M. Drewes, J. Hajer, J. Klaric, and G. Lanfranchi. *Perspectives to find heavy neutrinos with NA62*. arXiv, 1806:00100, 2018.

[56] The NA62 collaboration. *First results from the NA62 STRAW spectrometer*. PoS EPS-HEP, page 250, 2015.

[57] E. Goudzovski et al. *Development of the kaon tagging system for the NA62 experiment at CERN.* Nucl. Instrum. Meth., A801:86–94, 2015.

[58] S. Kholodenko. *NA62 charged particle hodoscope: design and performance in 2016 run.* JINST, 12:06042, 2017.

[59] F. Ambrosino. *The large angle photon veto system for the NA62 experiment at CERN.* Physics Procedia, 37:293–300, 2012.

[60] R. Ammendola et al. *The integrated low-level trigger and readout system of the CERN NA62 experiment.* Nuclear Inst. and Methods in Physics Research A, A929:1–22, 2019.

[61] R. Brun and F. Rademakers. *ROOT - an object orientated data analysis framework.* Nucl. Inst. Meth. in Phys. Res., A389:81–86, 1997.

[62] S. Agostinelli, J. Allison, K. Amako, and J. Apostolakis. *GEANT4 simulation toolkit.* Nuclear Instruments and Methods in Physics Research Section A: Accelerators, Spectrometers, Detectors and Associated Equipment, 506:250–303, 2003.

[63] The NA62 collaboration. *NA62 software.* https://na62-sw.web.cern.ch.

[64] T. Sjöstrand, S. Ask, J. Christiansen et al. *An introduction to PYTHIA 8.2.* Comput. Phys. Commun., 191:159, 2015.

[65] Particle Data Group. *Fragmentation functions in e^+e^- annihilation and lepton-nucleon DIS.* Phys. Rev. D, 98, 2018.

[66] L. Buonocore, C. Frugiuele, F. Maltoni et al. *Event generation for beam dump experiments.* JHEP, 05:028, 2019.

[67] The BESIII collaboration. *Determination of the pseudoscalar decay constant $f_{D_S^+}$ via $D_s^+ \to \mu^+\nu_\mu$.* Phys. Rev. Lett., 122:071802, 2019.

[68] G. Bernardi, G. Carugno, J. Chauveau et al. *Further limits on heavy neutrino couplings.* Phys. Lett. B, 203:332 – 334, 1988.

[69] The DELPHI collaboration. *Search for neutral heavy leptons produced in Z decays.* Zeitschrift fur Physik C Particles and Fields, 74:57–71, 1997.

[70] The Belle collaboration. *Search for heavy neutrinos at Belle.* Phys. Rev. D, 87:071102, 2013.

[71] The CMS collaboration. *Search for heavy neutral leptons in events with three charged leptons in proton-proton collisions at* $\sqrt{s} = 13\ TeV$. Phys. Rev. Lett., 120:221801, 2018.

[72] The LHCb collaboration. *Search for Majorana neutrinos in* $B^- \to \pi^+\mu^-\mu^-$ *decays*. Phys. Rev. Lett., 112:131802, 2014.